

TERAHERTZ METAMATERIALS FOR SENSING AND DETECTION

by

DAVID SHAWN WILBERT

SEONGSIN M. KIM, COMMITTEE CHAIR

PATRICK KUNG

QI HAO

DAVID HILTON

PATRICK LECLAIR

A DISSERTATION

Submitted in partial fulfillment of the requirements  
for the degree of Doctor of Philosophy  
in the Department of Electrical and Computer Engineering  
in the Graduate School of  
The University of Alabama

TUSCALOOSA, ALABAMA

2014

Copyright David Shawn Wilbert 2014  
ALL RIGHTS RESERVED

## ABSTRACT

The function of metamaterials targeted for operation at terahertz frequencies was investigated including split-ring resonators, perfect absorbers, and flexible absorbers. The devices were designed through simulation by finite element method commercial software and fabricated by photolithographic lift-off process using electron beam evaporation for the deposition of metal layers. The terahertz time domain spectroscopy measurement technique was used to characterize the devices in both transmission and reflection modes. Each device was composed of arrays of subwavelength resonant structures.

The split-ring resonator study focused on the effects caused by the addition of a passivation layer, which served to effectively lower the resonant frequencies of the rings, as well as the addition of a second layer of rings that led to a broadening of the resonant response of the structures. The perfect absorber investigation was focused on the polarization insensitive nature of the frequency selective surface elements. A mechanism for this property was proposed along with an equivalent circuit model that can describe and predict the resonant behavior. The perfect absorber were based on a unit cell structure with four-fold symmetry that consisted of a metal ground, a polyimide dielectric spacer layer, and top frequency selective surface layer. The flexible absorber chapter reports the simulation and characterization of perfect absorber structures fabricated on a polyimide flexible substrate that consisted of a metal ground plane, a dielectric spacer, and a frequency selective surface composed of two layers of differently sized, nonconcentric, circular rings separated by another dielectric spacer layer. Specifically, the frequency selective surface was seen to exhibit a frequency response dependent upon the

position of the individual resonant elements with respect to each other. The functionality of the flexible absorbers during deformation was also evaluated through the use of two custom designed vacuum holders. Characterization of the flexible absorbers before and after removal from the sacrificial substrate, as well as under both types of deformation, revealed that the structures had little change in functionality. The flexible absorbers were shown to be suitable for future incorporation in sensing applications and to have the potential to lead to future applications in cloaking.

## LIST OF ABBREVIATIONS AND SYMBOLS

<i>T-ray</i>	Terahertz frequency radiation
<i>f</i>	Frequency
<i>E</i>	Electric Field intensity
<i>P</i>	Power
<i>p</i>	Dipole moment
$\theta$	The angle between the propagation direction and the dipole moment <i>p</i>
<i>L</i>	The mean free path of the photocarriers in the photoconductive antenna
<i>q</i>	Photocarrier charge
<i>HEMT</i>	High electron mobility transistor
<i>DNA</i>	Deoxyribonucleic acid
<i>RNA</i>	Ribonucleic acid
$\omega$	Angular frequency of the terahertz electric field
<i>T(<math>\omega</math>)</i>	Complex transmission coefficient
<i>S(<math>\omega</math>)</i>	Frequency dependent amplitude
<i>FP(<math>\omega</math>)</i>	Fabry-Perot reflection contribution to transmission
$\varepsilon$	Permittivity
$\rho_v$	Volume charge density
<i>B</i>	Magnetic flux density
$\mu$	Permeability

$H$	Magnetic field intensity
$\sigma$	Conductivity
$n$	Complex refractive index
$\eta$	Complex wave impedance
<i>SRR</i>	Split-ring resonator
$\omega_p$	Metal plasma frequency
$\omega_c$	Metal scattering frequency
$k$	Wave number
$r$	Spot size radius
$\lambda$	Wave length
$D$	Electric displacement field
$\kappa$	Chirality parameter
<i>MEMS</i>	Microelectromagnetic systems
<i>THz-TDS</i>	Terahertz time domain spectroscopy
<i>PE</i>	Polyethylene
<i>TPX</i>	Polymethyl pentene
<i>Si</i>	Silicon
<i>HR Si</i>	High resistivity silicon
<i>FFT</i>	Fast Fourier transform
$R_{loss}$	Ohmic resistance
$L_{eff}$	Effective inductance
$C_{eff}$	Effective capacitance
<i>FEM</i>	Finite element method

<i>PBC</i>	Periodic boundary condition
<i>PEC</i>	Perfect electric conductor
<i>PMC</i>	Perfect magnetic conductor
<i>SBC</i>	Scattering boundary condition
<i>MFF</i>	University of Alabama Micro-Fabrication Facility
<i>E-beam</i>	Electron beam evaporation

## ACKNOWLEDGMENTS

I would like to thank the many colleagues, friends, and faculty members who have helped me with this research project. I must begin by thanking Dr. Margaret Kim, my advisor and dissertation committee chair, for sharing her research expertise, wisdom, and often great patience with me, and of course, for funding this research. I would also like to thank all of my committee members, Dr. Patrick Kung, Dr. Qi Hao, Dr. David Hilton, and Dr. Patrick LeClair for their invaluable input, inspiring questions, and support of both the dissertation and my academic progress.

This research would not have been possible without the support of my friends and fellow graduate students, including Gang Shen, William Baughman, Nabil Dawarhre, Soner Balci, Joseph Waters, and Foster Kim. I would especially like to thank Mohammad Parvinnezhad Hokmabadi for countless hours of simulation work, as well as valuable insight and discussions over the course of the last few years.

Finally, I would like to thank my family, especially my Dad and Grandmom. Last, but certainly not least, I must thank my wife, Caitlin, for her constant support throughout my graduate education, and both of the rest of our families who never stopped encouraging me.

## CONTENTS

ABSTRACT.....	ii
LIST OF ABBREVIATIONS AND SYMBOLS .....	iv
ACKNOWLEDGMENTS .....	vii
LIST OF TABLES .....	xi
LIST OF FIGURES .....	xii
1. INTRODUCTION .....	1
1.1. Introduction.....	1
1.2. Dissertation Organization and Structure .....	2
2. TERAHERTZ TECHNOLOGIES BACKGROUND.....	4
2.1. Description of Terahertz Technologies.....	4
2.2. Applications of Terahertz Frequency Radiation .....	10
2.3. Advantages and Disadvantages at Terahertz Frequencies .....	16
3. METAMATERIALS BACKGROUND.....	18
3.1. The Interaction of Light and Matter.....	18
3.2. Description of Metamaterials.....	20
3.3. Metamaterial Applications.....	25
4. TERAHERTZ TIME DOMAIN SPECTROSCOPY.....	33
4.1. Description of Operation.....	33
4.2. Reflection Mode System Modification .....	37
4.3. Data Collection and Processing .....	38

4.4. Terahertz Spectroscopic Imaging .....	43
5. SPLIT-RING RESONATORS.....	47
5.1. Split-Ring Resonator Background .....	47
5.2. Simulation of Split-Ring Resonators .....	52
5.3. Split-Ring Resonator Fabrication .....	59
5.4. Split-Ring Resonator Measurement Procedure.....	64
5.5. Split-Ring Resonator Results.....	65
5.6. Conclusion .....	70
6. PERFECT ABSORBERS .....	71
6.1. Perfect Absorber Background.....	71
6.2. Simulation of Perfect Absorbers .....	77
6.3. Perfect Absorber Fabrication .....	81
6.4. Perfect Absorber Measurement Procedure .....	86
6.5. Perfect Absorber Results.....	87
6.6. Conclusion .....	96
7. FLEXIBLE ABSORBERS .....	97
7.1. Flexible Device Background.....	97
7.2. Flexible Absorber Simulation .....	100
7.3. Flexible Absorber Fabrication .....	105
7.4. THz-TDS Measurement of the Flexible Absorbers .....	108
7.5. Flexible Absorber THz-TDS Results.....	112
7.6. Conclusion .....	117
8. CONCLUSION.....	118

8.1. Summary of Findings.....	118
8.2. Future Work.....	120
REFERENCES .....	122
APPENDIX A: PUBLICATIONS .....	138
A.1. Peer-Reviewed Journal Articles.....	138
A.2. Conference Proceedings.....	140

## LIST OF TABLES

4.1. Z-2 Spectral Water Vapor Absorption Line Frequencies .....	42
5.1. Split-ring Resonator Unit Cell Dimensions by Targeted Frequency ..	58
7.1. Flexible Absorber Ring Diameters and Center-to-Center Spacings .	101
7.2. Absorbance at Resonant Frequency Data Summary.....	116

## LIST OF FIGURES

2.1. Electromagnetic Spectrum .....	4
2.2. Diagram of Sample Refractive Indices for Material Parameter Calculation .....	12
2.3. Terahertz Imaging of Concealed Weapons .....	13
3.1. Permittivity and Permeability Diagram .....	21
3.2. Snell's Law .....	23
3.3. Operational Frequency of Metamaterials by Year .....	25
3.4. Chen's Electric Ring Resonator-based Metamaterial Modulator .....	29
3.5. Magnetoelastic Metamaterial .....	30
4.1. Transmission Mode Z-2 .....	34
4.2. Z-2 Signal-To-Noise .....	36
4.3. Reflection Mode Z-2 .....	37
4.4. Zero-Padding Process .....	41
4.5. THz Analyzer Data Processing .....	42
4.6. Spectral Water Vapor Absorption .....	43
4.7. THz Imaging Process .....	44
4.8. Image Reconstruction Process .....	46
5.1. Bi-anisotropy in the Split-Ring Resonator .....	48
5.2. RLC Circuit Model for a Split-Ring Resonator .....	49
5.3. Resonant Frequency Estimation Dimensional Parameters .....	50
5.4. Pendry's Micro-sized Resonators .....	51

5.5. Split-Ring Resonator Model Geometry .....	53
5.6. Split-Ring Resonator Simulation Model with Added Mesh .....	55
5.7. 3-D Split-Ring Resonator Electric Field Density Simulation.....	55
5.8. 2-D Split-Ring Resonator Electric Field Density Simulation.....	56
5.9. Simulation of Transmittance, Reflectivity, and Absorbance .....	57
5.10. Split-Ring Resonator Unit Cell and Dimensions .....	58
5.11. Fabricated Single and Double Layer Split-Ring Resonators .....	59
5.12. Optical Microscope Picture of SRR Patterned Photoresist.....	61
5.13. Optical Microscope Picture of SRR Patterned Photoresist.....	63
5.14. Scanning Electron Microscope Image of Split-Ring Resonators ....	63
5.15. Electric Field Isolated Split-Ring Resonator .....	64
5.16. Magnetic Field Isolated Split-Ring Resonator.....	65
5.17. Electric Field Isolated Transmittance .....	66
5.18. Magnetic Field Isolated Transmittance.....	67
5.19. Simulated and Measured Transmittance.....	67
5.20. Single, Passivated, and Double Layer Transmittance Comparison ..	68
5.21. Transmittance of Copper and Gold Split-Ring Resonators .....	69
5.22. Transmittance of Chromium Array and Low Resistivity Silicon .....	70
6.1. Unit Cell of the First Metamaterial Absorber .....	72
6.2. Dual Band Metamaterial Absorbers.....	73
6.3. First Polarization Insensitive Metamaterial Absorber .....	74
6.4. Perfect Absorber Unit Cell and Size Dimensions.....	76
6.5. Simulation Model of the Perfect Absorber .....	77

6.6. Absorbers Simulated Electric and Magnetic Fields at Resonance.....	78
6.7. Absorbers Simulated Electric and Magnetic Fields at Resonance.....	78
6.8. Simulation of Surface Current Density in Absorbs .....	79
6.9. Simulated Absorbance of Absorbers with Varied Outer Length .....	80
6.10. Absorption Strength and Dielectric Thickness Correlation .....	80
6.11. Absorber Photomask Layout.....	81
6.12. Absorbers Patterned in Photoresist .....	83
6.13. SiO <sub>2</sub> Adhesion Layer .....	84
6.14. Polyimide Spin-Speed Curves .....	85
6.15. Absorber Measurement Orientations .....	86
6.16. Absorbers with Different Polyimide Thickness.....	88
6.17. Effect of Metal Conductivity on Absorber Function .....	89
6.18. Measured Absorbance of Absorbers with Varied Dimensions.....	90
6.19. Measured Time Domain Amplitude of Absorbers.....	91
6.20. Absorber Equivalent Circuit Model and Explanation.....	92
6.21. Calculated Impedance of Absorbers .....	93
6.22. Absorbance Measurement of Rotated 2-T Absorbers.....	94
6.23. Absorber Array Imaging .....	96
7.1. Flexible OLED Display and Solar Cell .....	97
7.2. High Refractive Index Flexible Metamaterial .....	99
7.3. Diagram of a Flexible Broadband Absorber .....	99
7.4. Flexible Absorber Unit Cell Top and Side View Diagrams .....	101
7.5. Flexible Absorber Simulation Model Geometry with Mesh.....	102

7.6. Simulated Surface Currents in the Flexible Absorber .....	102
7.7. Simulated Electric Field Density near Flexible Absorber .....	103
7.8. Simulated Absorbance of the Flexible Absorber at 0° and 90° .....	104
7.9. Picture of Trapped Bubbles in Polyimide .....	105
7.10. Picture of the Flexible Substrate .....	106
7.11. Optical Microscope Picture of Fabricated Flexible Absorber .....	107
7.12. Side View Diagram of the Fabricated Flexible Absorber.....	108
7.13. Flexible Absorber Measurement Setup.....	109
7.14. Cylindrical and Spherical Vacuum Holder Designs .....	110
7.15. Measurement Setup with Vacuum Holders .....	111
7.16. Measured Absorbance of Flexible Absorbers before Removal from Silicon Wafer .....	112
7.17. Measured Absorbance of Flexible Absorbers after Removal from Silicon Wafer .....	113
7.18. Measured Absorbance of Flexible Absorbers during Stretching ....	114
7.19. Modified Measurement Setup for Microscope Viewing .....	114
7.20. Picture of Stretched Flexible Absorber Array .....	115
7.21. Measured Absorbance of Flexible Absorbers on Cylindrical Vacuum Holder .....	115
7.22. Measured Absorbance of Flexible Absorbers on Spherical Vacuum Holder .....	116

## CHAPTER 1

### INTRODUCTION

#### 1.1. Introduction

The terahertz region of the electromagnetic spectrum holds much promise for a variety of different applications due to the unique interaction of materials with radiation at these frequencies. However, it remains challenging to manipulate terahertz frequency radiation. Metamaterials, which are composite materials consisting of arrays of subwavelength resonant structures that give rise to exotic electromagnetic properties, can enable the manipulation of terahertz frequency radiation. This work includes a basic review of the terahertz region of the electromagnetic spectrum and covers some of the applications for radiation at these frequencies. A similar review for metamaterials and metamaterial-based applications is also presented. The main body discusses the investigation of three specific metamaterial devices including split-ring resonators, metamaterial perfect absorbers, and flexible absorbers with focus being on the fabrication and characterization of the structures and comparison of the measured response to simulation. Some of the important contributions of this work are the explanation of polarization insensitivity in the four-fold symmetric metamaterial perfect absorber, and the development of a flexible metamaterial fabrication procedure as well as new methods for device sensing measurements. Finally, the results of this work showed all three metamaterial devices to be suitable for future sensing applications and that the flexible absorbers hold promise for leading to future applications in cloaking.

## 1.2. Dissertation Organization and Structure

This dissertation continues in Chapter 2, with an overview of terahertz technologies. The chapter is divided into three subsections. The first of these covers some the unique properties of terahertz frequency radiation as well as means for generation and detection at these frequencies. The second subsection covers some of the applications that have been realized for radiation in this range of the electromagnetic spectrum. The chapter ends with a discussion of the advantages and disadvantages of terahertz frequency radiation compared to other frequencies such as X-rays.

Chapter 3 provides background coverage on the subject of metamaterials. The chapter begins with a brief explanation of the interaction of light and matter. The subject is discussed through Maxwell's equations and the refractive index. The second subsection defines the term 'metamaterial' and gives a description of the physics of metamaterials. Chapter 3 concludes with a review of some of the various applications for which metamaterials have been used.

The fourth chapter goes into more depth on the terahertz time domain spectroscopy method. It begins with an explanation of the operation of the terahertz time domain spectroscopic system which leads into a description of the system that was used for the measurements performed for this work. Next, the system modification that enabled reflection mode measurement with our system, the Z-2, is covered, along with data collection and processing methods used for this work. Finally, the terahertz imaging capabilities using the modified Z-2 are described.

Chapter 5 starts to focus on the major work of my research beginning with split-ring resonators. The chapter begins with some background on the split-ring resonator, as well as the physical operation of the device. Then the split-ring resonator simulation, fabrication, and

measurement procedures are detailed. The results of the study are next explained with emphasis of the effects of the addition of a passivation layer and second layer of split-ring resonators.

Chapter 6 discusses the terahertz metamaterial perfect absorbers. The chapter begins with a literature review on the topic of metamaterial perfect absorbers and explains to motivation for the work covered in Chapter 6. The simulation, fabrication, and measurement of both polarization dependent and insensitive absorbers in this project are next discussed, followed by a summary of the results and conclusion.

Chapter 7 covers flexible absorbers starting with background on flexible metamaterial devices and the inspiration for the work. Then the device simulation, fabrication, and measurement are described in detail. The chapter ends with the comparison of simulation and measurement results as well as a conclusion.

The dissertation concludes with Chapter 8 which provides a summary of the findings of the split-ring resonator, perfect absorber, and flexible absorber projects. This chapter ends with a discussion of possible future work for these projects.

## CHAPTER 2

### TERAHERTZ TECHNOLOGIES BACKGROUND

#### 2.1. Description of Terahertz Technologies

Over the past two decades, research in the terahertz frequency range of the electromagnetic spectrum has expanded greatly. This frequency range extends from 0.1 THz to 10 THz, corresponding to wavelengths from 30  $\mu\text{m}$  to 3 mm and photon energies from 0.4 meV to 40 meV, and lies in the overlapping region between the microwave and infrared ranges as shown in Figure 1.1. This part of the spectrum is commonly referred to as the terahertz gap and radiation in this region is often called T-rays. It is called the terahertz gap because, unlike most of the rest of the electromagnetic spectrum, the conversion from electric power into electromagnetic radiation cannot be efficiently accomplished through the use of semiconductor devices.<sup>1,2</sup>

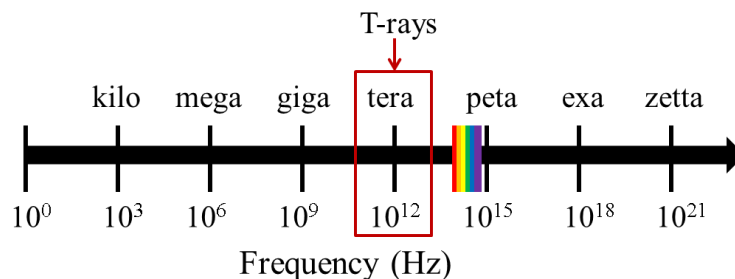


Figure 2.1. The electromagnetic frequency spectrum.

Until the late 1960s, the Globar lamp, an electrically heated silicon carbide rod filament which emits radiation into the far infrared as a black body source, was the only means of

radiation generation at terahertz frequencies. The first reports<sup>3,4,5,6</sup> on the use of nonlinear crystals for optical difference-frequency mixing started in 1969. Optical difference-frequency mixing occurs when two light beams are passed through a nonlinear crystal allowing a third frequency beam to be generated with a frequency that is the difference of the frequencies of the first two light beams. This technique allowed the coherent generation of far-infrared radiation and eventually led to generation methods for terahertz frequency radiation including difference-frequency generation, optical rectification, and photoconductive emission. These methods helped generate strong interest in the field. Both pulsed and continuous wave sources currently exist with different power outputs from a few nanoWatts to several tens of Watts in terms of average power using free electron lasers.

The current methods most often used for generation are photoconductive emission and optical rectification. The optical rectification method was first discovered in 1984<sup>7</sup> and successfully used in 1989.<sup>8</sup> It is a process relying on low difference-frequency mixing wherein the polarization of a high intensity pulse of radiation is rectified by the nonlinear response of a crystal structure. Common crystals used for optical rectification include LiNbO<sub>3</sub>, GaSe, GaAs, and ZnTe, with ZnTe being the most common because of its close phase-matching of the terahertz phase velocity to the group velocity of the high intensity pump pulse inside of the crystal.<sup>9</sup> During the optical rectification process, the generated terahertz beam will be confined inside of the crystal due to total internal reflection unless it is coupled to a matching lens, typically sapphire or silicon, which allows the terahertz beam to escape into free space propagation. The optical rectification method of generation maybe the most commonly used as it can generate broadband radiation with a range of 0.1 THz to 40 THz.<sup>1</sup>

The photoconductive emission method utilizes a device called the photoconductive antenna and was developed during the same time period as the optical rectification method.<sup>10,11,12</sup> In a photoconductive antenna, broadband terahertz frequency radiation is generated by the acceleration and subsequent recombination of photocarriers created by the absorption of a high intensity laser pulse. The laser photon energy must be greater than the bandgap of the crystal material used for the photoconductive antenna in order to effectively excite photocarriers. Common materials widely used for photoconductive antennas include LiTaO<sub>3</sub><sup>13</sup>, InP<sup>14</sup>, InAs<sup>15</sup>, CdTe<sup>14</sup>, and GaAs.<sup>14</sup> Often the photoconductive antenna will be biased with an applied electric field which forces the vector of the photocarrier acceleration. This is accomplished by depositing thin, parallel metal strips across the crystal surface. In others, the acceleration is due to a built-in surface depletion field.

The far field electric field of a radiated pulse from a photoconductive antenna can be given by:

$$E \propto \int \frac{\sin\theta}{R} \frac{d^2p}{dt^2} dx dy \quad (2.1)$$

where  $R$  is the distance between the antenna and the point of measurement,  $\theta$  is the angle between the propagation direction and the dipole moment  $p$ .<sup>16</sup> If we let  $L$  represent the mean free path of the photocarriers in the photoconductive antenna and  $q$  be the photocarrier charge, then it can be assumed that:

$$p = Lq \quad (2.2)$$

and we can say that:

$$\frac{d^2p}{dt^2} = L \frac{d^2q}{dt^2} \quad (2.3)$$

The first derivative of the photocarrier charge with respect to time is of course the photocurrent. Making the substitution and combining the equation with that for the far field electric field yields:

$$E \propto \int \frac{L \sin \theta}{R} \frac{dJ}{dt} dx dy \quad (2.4)$$

where  $dJ/dt$  is the transient photocurrent. This equation shows that the electric field strength is inversely related to the propagation distance, but also proportional to the transient photocurrent. For this reason, the selection of the material used in the fabrication of a photoconductive antenna is of critical importance. The antenna material should exhibit short recombination time. However, for pure crystals, recombination times are mostly too long. To remedy this situation, defects can be introduced through the addition of dopants or defects which can act as traps or scattering centers thereby reducing recombination times. It is also possible to avoid the problem by using crystals with large concentrations of inherent defects such as low temperature grown GaAs. There is an unavoidable trade off, however, because high defect concentrations can lead increased elastic scattering and lower photocarrier mobility. Studies have also shown that the photoconductive antenna can be made more efficient through the use of cryogenic cooling to increase mobility<sup>17</sup> or by the use of an applied magnetic field.<sup>18</sup>

The photoconductive antenna is also an effective means of detection. The antenna must be photoexcited by the high intensity laser pulse of sufficiently high photon energy to allow the interband carrier transitions. When a pulse of terahertz radiation strikes the antenna at the same

time as the pump laser pulse, the surface current in the antenna will be proportional to the electric field of the incident terahertz pulse.

Photoconductive antenna detection has some distinct advantages. They exhibit high sensitivity in terms of signal-to-noise ratio due to the rejection of incoherent radiation from detection and the narrow sampling time per data point. They are most often compact with the entire detector built into a small chip. The use of a photoconductive antenna as a detector has an inherent drawback, however, in that they are difficult to align because the effective area of sensitivity tends to be quite small, usually on the order of tens to a few hundred microns, which results in a requirement for additional focusing optics and tremendous effort for alignment. Even with the additional focusing optics, due to the diffraction limit of the terahertz beam, it is not likely to make the beam spot size small enough to collect the entire terahertz beam cross section during detection. Photoconductive antennas also tend to have more narrow bandwidth than the other common method of detection—electro-optic sampling.

Electro-optic sampling relies on the first order non-linearity, referred to as Pockels effect, in birefringent electro-optic crystals. When a linearly polarized laser pulse propagates through the crystal, its polarization becomes circular with no shift in phase. In the presence of an applied electric field, the birefringent nature of the crystal causes the polarization of the passing laser pulse to instead become elliptical due to a slight phase shift. In our case, the electric field component of the terahertz pulse serves as the applied electric field. The terahertz pulse ellipticity—the ratio of major and minor axes of polarization—is directly proportional to the electric field of the terahertz pulse.

Electro-optic sampling of terahertz pulses was first demonstrated in 1995.<sup>19</sup> The same materials used for generation through optical rectification methods can also be used for electro-optic sampling detection. One distinct benefit of electro-optic sampling for detection is a very large measurable bandwidth, from 0.1 THz to 100 THz, by using multiple materials (electro-optic crystals) in the detection scheme.<sup>20</sup> Like photoconductive antenna based detection, electro-optic sampling can be difficult to align. However, the area of sensitivity in an electro-optic crystal is much larger than that of a photoconductive antenna, allowing for a more complete collection of the terahertz pulse. Another drawback of this method is that the temporal resolution is limited by the mismatch in the velocity of the laser pump pulse and the terahertz pulse. This issue has been resolved through changes in emitter and detector designs.<sup>21,22</sup> Another method for both generation<sup>23</sup> and detection<sup>24</sup> is the high electron mobility transistor, or HEMT. Research into the use of HEMT structures for these purposes has been occurring in parallel with the photoconductive antenna and electro-optic sampling methods. HEMTs are an especially promising means of detection because they offer the possibility for room temperature detection of both continuous wave and pulsed broadband radiation with great sensitivity and responsivity. HEMT-based terahertz detection occurs when plasma waves are excited by incident terahertz radiation and oscillate/resonate in the device channel provided the device dimensions and materials are selected to target the appropriate plasma frequency. Common materials used for these devices include InGaAs, InAlAs, and InP to achieve the desired channel carrier (electron) density. Gate lengths are typically in the submicron range.<sup>25</sup> During operation, incident terahertz waves couple with the plasma resulting in plasmon excitation in the channel. The generated plasmon current has a quadratic relationship to the product of the multiplication of the local carrier velocities and densities leading to a rectified current component. This rectified

component can then be collected at the high-impedance drain contact allowing the HEMT to operate as a terahertz detector.

These recent advances in the ability to generate and detect radiation at terahertz frequencies have enabled an ever growing number of applications for this region of the spectrum.

## 2.2. Applications of Terahertz Frequency Radiation

Spectroscopy for scientific research purposes using either narrowband tunable systems or broadband time domain systems is the most common application for terahertz frequency radiation. Terahertz time domain spectroscopy which utilizes the time domain measurement of short broadband terahertz pulses, from which frequency dependent transmission or reflection can be obtained, has been commonly used for spectroscopy applications. Many biomolecules exhibit characteristic vibrational modes at terahertz frequencies. In particular, the responses of deoxyribonucleic acid (DNA)<sup>26</sup>, ribonucleic acid (RNA)<sup>27</sup>, and various proteins<sup>28,29,30,31,32,33</sup> at terahertz frequencies have been studied using this technique. It has been shown that terahertz frequencies are sensitive to the biomolecular functioning of DNA as both refractive index and absorption spectrum exhibit unique change as the DNA is altered from single-stranded to hybridized forms<sup>34</sup>, and can even be capable of detecting single point mutations.<sup>35</sup> For proteins, terahertz frequencies have shown to be sensitive to thermal denaturing of bovine serum albumin.<sup>36</sup> In this study, the denatured, pressed pelleted protein was seen to have a distinct change in the terahertz response arising from both structural vibrational modes and side chain rotational modes, similar to the results of a different study of cytochrome c, which is a mitochondrion membrane protein.<sup>37</sup>

Terahertz spectroscopy has also proven valuable for the determination of material properties in a variety of materials including polymers, crystalline dielectrics, and semiconductors. Material properties such as transmission and reflection coefficients, permittivity, conductivity and refractive index can be obtained through terahertz spectroscopy. The first work done in this area was performed by Grischkowsky et al. in 1990 on materials including sapphire, quartz, fused silica, silicon, gallium arsenide, and germanium.<sup>38</sup> For their work, they studied the absorption coefficient and refractive index for each material by utilizing the terahertz transmission spectrum. In 1996, Duvillaret et al. reported a method for obtaining the refractive index of a material by measuring a homogeneous slice of uniform thickness, provided the material and its surroundings have a linear electromagnetic response and are magnetically isotropic.<sup>39</sup> The method required the measurement of the transmitted frequency dependent terahertz amplitude from both the sample and the reference/substrate and used the equation:

$$T(\omega) = \frac{S_{Sample}(\omega)}{S_{Reference}(\omega)} = \frac{2\tilde{n}_2(\tilde{n}_1 + \tilde{n}_3)}{(\tilde{n}_2 + \tilde{n}_1)(\tilde{n}_2 + \tilde{n}_3)} * e\left[-i(\tilde{n}_2 - \tilde{n}_1)\frac{\omega L}{c}\right] * FP(\omega) \quad (2.5)$$

where  $\omega$  is the angular frequency of the terahertz wave electric field,  $T(\omega)$  is the complex transmission ratio,  $S_{Sample}(\omega)$  and  $S_{Reference}(\omega)$  represent the measured frequency dependent transmitted amplitude through the sample and reference, respectively,  $\tilde{n}_1$ ,  $\tilde{n}_2$ , and  $\tilde{n}_3$  give the complex index of refraction of air, the sample, and the substrate, respectively, as illustrated in Figure 2.2,  $L$  is the sample thickness, and  $FP(\omega)$  represents the forward and backward Fabry-Perot reflection contributions to the transmission given by:

$$FP(\omega) = \frac{1}{1 - \left(\frac{\tilde{n}_2 - \tilde{n}_1}{\tilde{n}_2 + \tilde{n}_1}\right) \left(\frac{\tilde{n}_2 - \tilde{n}_3}{\tilde{n}_2 + \tilde{n}_3}\right) * e^{-2i\tilde{n}_2(\frac{\omega L}{c})}} \quad (2.6)$$

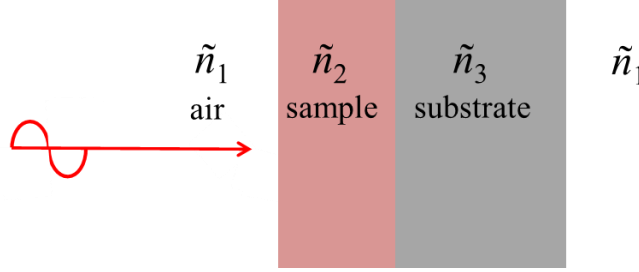


Figure 2.2. Diagram of a sample for terahertz spectroscopic measurement showing the refractive indices used for the calculation of material parameters.

It was reported that in an optically thick sample, the Fabry-Perot contributions could be removed by selectively windowing the measurement which simply meant cutting the time domain raw data before the reflection occurred. This was possible due to the fact that in an optically thick sample, the Fabry-Perot reflections occur temporally far away from the main pulse. Because  $\tilde{n}_1$  and  $\tilde{n}_3$  were known quantities, it was straight forward to solve for the refractive index of the sample. Since then a plethora of other materials have been studied, and the technique has been expanded to allow for the measurement of additional material properties including carrier concentrations and relaxation times.<sup>40</sup> By modifying a terahertz spectroscopy system setup to add an optical pump pulse incident onto the measured sample, time-resolved terahertz spectroscopy is able to determine carrier lifetimes and mobilities by applying the same measurement techniques.<sup>41,42,43</sup>

Along the same vein as these research driven spectroscopic applications, a strong commercial application for security is remote sensing since many materials show unique

sensitivity to terahertz frequency radiation. Terahertz radiation has been shown to be useful for standoff detection of various substances including drugs<sup>44,45</sup> and explosives.<sup>46,47,48</sup> This is possible due to the unique absorption spectra of these substances. The unique absorption spectra of various materials combined with the fact that other materials are transparent at terahertz frequencies allows for security type imaging. Similar to medical X-ray imaging, T-ray imaging can provide the ability to see concealed objects such as knives and firearms as seen in Figure 1.2. Whereas X-ray imaging can only yield the ability to see concealed objects based on back scattering, the collected back scattering in T-ray imaging can be used not only to see concealed materials, but to identify them as well. This property gives T-ray imaging the additional benefit that it will eventually allow for automated systems with fewer false alarms, which will improve throughput and decrease waiting times in places such as airports, resulting in savings in terms of manpower costs.<sup>49</sup>

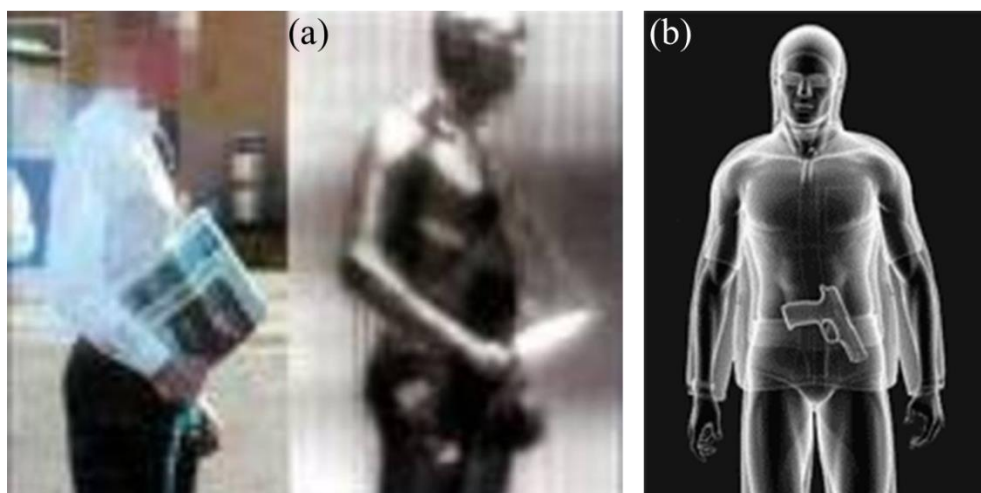


Figure 2.3. (a) Picture and corresponding T-ray image of a man carrying a concealed knife<sup>50</sup> and (b) T-ray image of a man carrying a concealed firearm.<sup>51</sup>

The wide range of investigation into the use of T-rays for imaging based on spectroscopic methods that first started in 1995<sup>52</sup> is ongoing. Biomedical imaging is one area of research that

has seen rapid growth recently. This is again due to its non-ionizing nature and also due to the unique property of being very sensitive to intermolecular vibrations and polar substances such as water. Because some cancerous tissue types have been found to have higher water content than surrounding normal tissues, T-ray imaging can serve as a means of detection.<sup>53,54</sup> Unfortunately, current T-ray imaging is limited in its use for many biomedical imaging applications since terahertz frequency radiation will not penetrate deep enough due to strong absorption by water. However, skin cancers such as basal cell carcinoma can be a prime candidate for this type of application as the imaging can be performed based on reflected radiation instead of transmission.<sup>55</sup> T-ray imaging is even being used for pharmaceutical purposes of quality control and determining release mechanisms of drugs.<sup>56</sup>

High frequency communications is another area of intense research. As wireless communication technology has progressed from low frequency radio wave carrier waves into the microwave region, both the speed of flow and the overall amount of information able to be transmitted and received has continuously increased. Current wireless communications are mainly dominant in the microwave range with carrier frequencies of several tens of gigahertz. The ability to further progress wireless communications technology into the terahertz range could improve this performance by a factor of thousands. This along with such envisioned applications as short range secure battlefield communications has spurred research into this area.

Communication at terahertz frequencies can allow for large bandwidths. By modulating the transmission in short bursts on different frequencies over the bandwidth range, referred to as frequency hopping, communications can be made even more secure than using encryption alone. Not only would this make eavesdropping more difficult, frequency hopping over such a large bandwidth would make it improbable that the communication could be detected at all. However,

difficulties in realizing wireless communications at terahertz frequencies including appropriate modulation of a carrier signal and the fact that the system bandwidth is usually intrinsically limited by the bandwidth of the transmitter or detector must first be overcome. Current methods of modulation eventually rely on electronic means which can also limit actual data rates. These modulation methods are divided into two types which are modulation of T-ray generation and external T-ray modulation.

A delay line can be used to mechanically modulate the terahertz waveform during generation in pulsed time domain and continuous wave photomixing methods. This method is comparatively slow with maximum repetition rates on the order of a few hundred hertz.<sup>57,58,59</sup> It is also possible to modulate the waveform (amplitude modulation) through modulation of the applied bias voltage of the photoconductive antenna. This form of modulation can achieve repetition rates near 1 MHz.<sup>60,61</sup> The most promising of the generation modulation methods involves electrically modulating a Schottky diode which serves as a delay line. This method can potentially increase repetition rates into the gigahertz range but is currently rather inefficient.<sup>52,63</sup>

The external T-ray modulation methods currently suffer from limited modulation bandwidth and carrier wave frequency. Some of these methods include liquid crystal modulators<sup>64,65</sup>, free carrier in semiconductor modulators<sup>66,67</sup>, and ferroelectric modulators.<sup>68</sup> J. Federici and L. Moeller published an excellent review of T-ray wireless communications in 2010 that will shed more light on this topic.<sup>69</sup> With the strong interest and continued work in this area, our ability to effectively modulate terahertz frequency carrier waves will no doubt improve and overcome these problems in the near future.

Finally, terahertz frequency radiation holds much value in astronomy. This is due to three reasons. First, infrared radiation is the most abundant form of radiation in the Universe because temperatures in space are extremely cold. The small amount of heat that objects in space radiate is typically in the far-infrared and terahertz regions. Second, many objects in space are obscured by dust and debris clouds that scatter visible light reflected from objects we would like to observe. Because T-rays have wavelengths much larger than the dust particles, T-rays can penetrate and pass through these dust clouds enabling the collection of radiation. Third and finally, visible radiation emitted or reflected from objects that are moving away from the earth rapidly due to expansion of the Universe is often Doppler redshifted into the terahertz region.<sup>70</sup> Since the 1980s, far-infrared and T-ray astronomy research has expanded as new telescopes and observatories have been installed in Hawaii<sup>71</sup>, Antarctica<sup>72</sup>, and Chile.<sup>73</sup> Terahertz spectroscopy based telescopes provide spectroscopic information that can allow for the identification of materials and material states which is especially useful for studying the birth process for stars or for finding systems outside our solar system that may contain planets with water.<sup>74</sup>

### 2.3. Advantages and Disadvantages at Terahertz Frequencies

Terahertz frequency radiation has several advantages over radiation of other frequencies. In terms of biomedical imaging, terahertz frequency radiation is non-ionizing which means that it is less harmful to living tissues than X-rays. As previously discussed, it is higher frequency than radio and microwave frequencies, so it has the potential to provide much higher data speeds. Many materials have a unique absorption spectrum in the terahertz frequency range which can provide the ability to precisely sense or detect them. Also, many materials are transparent at terahertz frequencies.

However, terahertz frequency radiation has some severe disadvantages as well. All matter that is warmer than the equilibrium temperature of its surroundings emits thermal energy including a random distribution of terahertz radiation. However, this is of little use for most applications since coherent sources are required for most applications. Secondly, high power sources did not exist until only very recently. Even now, the few sources available are very costly. T-rays are rapidly absorbed by water vapor in the atmosphere meaning that its use is limited to short distances or enclosed, purges spaces. Due to those issues, terahertz frequency communication is limited to a short range, line of sight functionality.<sup>69</sup> However, the strong atmospheric attenuation can actually be seen as a benefit for certain types of communication applications as it can serve to make inter-satellite communication at terahertz frequencies more secure. Also, T-rays from a ground source may be back scattered off the atmosphere and received by another ground station with low noise and little chance of satellite eavesdropping, both due to the attenuation. Finally, there are few natural materials that can be used to efficiently manipulate radiation at terahertz frequencies. Therefore, it has still proven difficult to work with outside of research environments, but a relatively new class of materials known as metamaterials promises to enhance our ability to manipulate radiation at these frequencies.

## CHAPTER 3

### METAMATERIALS BACKGROUND

#### 3.1. The Interaction of Light and Matter

Much of human perception is due to the interaction of light and matter. Most notably sight which is simply the interpretation of signals sent to the brain that are caused by the interaction of visible light with the eye. Electricity and magnetism have been observed and studied extensively for centuries, but it was not until the discoveries of Orsted, Gauss, Ampere, and Faraday in the early to middle 1800s that we began to gain a true understanding of these phenomena. Then, in 1864, Maxwell's mathematical correlation of these discoveries led to the discovery of four equations:

$$\nabla \cdot \epsilon \mathbf{E} = \rho_v \quad (3.1)$$

$$\nabla \cdot \mathbf{B} = 0 \quad (3.2)$$

$$\nabla \times \mathbf{E} = -\frac{\partial}{\partial t}(\mu \mathbf{H}) \quad (3.3)$$

$$\nabla \times \mathbf{H} = \sigma \mathbf{E} + \frac{\partial}{\partial t}(\epsilon \mathbf{E}) \quad (3.4)$$

where  $\epsilon$  is the permittivity,  $\mathbf{E}$  is the electric field intensity,  $\rho_v$  is the volume charge density,  $\mathbf{B}$  is the magnetic flux density,  $\mu$  is the permeability,  $\mathbf{H}$  is the magnetic field intensity, and  $\sigma$  is the material conductivity.

Maxwell's equations allowed him to discover that time varying electric and magnetic fields produce radiation that propagates through space and thus the electromagnetic nature of light, establishing modern electromagnetism. The solution to these equations for a given system, provided appropriate boundary conditions are known, completely describe the electric and magnetic fields at every point in space in the system and moreover describe the wave interaction with any particular medium.

The electromagnetic response of a material can be characterized by its intrinsic properties of electrical conductivity, permittivity, and permeability. The electrical conductivity is a measure of a material's ability to develop an electric current in the presence of an applied electric field. The permittivity of a material is its ability to resist the formation of an electric field. Likewise, the permeability of a material is its ability to resist the formation of a magnetic field. Permittivity and permeability, which describe the effective or net electric and magnetic responses of a material, respectively, but on a smaller scale, are caused by the sum response of the electric and magnetic dipoles inside the material. The electric dipoles in ordinary material can be due to carriers (electron-hole), atomic (electron-nucleus), and molecular arrangement (ions). Most materials do not have internal magnetic dipoles which is why ordinary materials have near unity permeability.

Other useful material parameters for describing the electromagnetic response of a material can also be derived from Maxwell's equations. The refractive index of a material is a unitless quantity that yields the speed at which radiation will travel through the material relative to the speed of light and falls naturally out of Maxwell's equations. The refractive index of a material is determined by the equation:

$$n = \pm\sqrt{\epsilon\mu} \quad (3.5)$$

where  $n$  is the complex refractive index of the material. Similarly, the wave impedance is given by the equation:

$$\eta = \sqrt{\frac{\mu}{\epsilon}} \quad (3.6)$$

where  $\eta$  is the wave impedance. It should be noted that all of these material parameters are frequency dependent.<sup>75</sup>

### 3.2. Description of Metamaterials

In 1968, Russian physicist Victor Veselago theoretically calculated the electromagnetic response of a material with simultaneously negative permittivity and permeability. According to his calculations, electromagnetic waves in this type of material, which he called left-handed, would have phase velocities that are anti-parallel to the group velocities. In his paper, he envisioned left-handed materials properties including reversed Doppler shift and reversed Cerenkov and even alluded to superlensing applications even though materials that could have negative permeability did not exist.<sup>76</sup> No further progress could be achieved until 1999 when Pendry reported a theoretical design—the split-ring resonator (SRR)—that could provide a negative permeability medium<sup>77</sup> quickly followed by the first report of a fabricated left-hand material by Smith in 2000.<sup>78</sup>

In 2001, Walser coined the term metamaterial.<sup>79</sup> A metamaterial can be defined as a homogeneous effective medium that exhibits an unusual electromagnetic response. Metamaterials typically consist of an array of subwavelength, electromagnetically resonant

structures. Unlike ordinary material, whose properties come directly from its constituents, the unusual electromagnetic characteristics of a metamaterial occur because of the size, geometry, and orientation of the comprising resonant structures. This unique attribute can allow for an engineerable electromagnetic response in metamaterials and is the commonly accepted definition of a metamaterial. It should be noted that left-handed materials are a subclass of metamaterials.

A material can be classified by its electromagnetic response into one of four categories based on the sign of its permittivity and permeability. It is helpful to visualize this as a quadrant system as seen in Figure 3.1. Most natural materials can only fall into the first, second, or fourth quadrants. The first category is composed of materials with simultaneously positive permittivity and permeability. These materials allow radiation to propagate and are referred to as dielectrics.

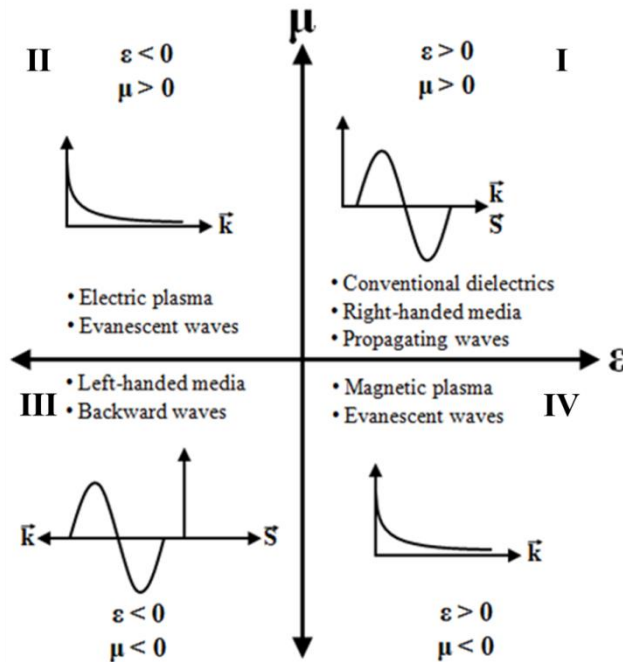


Figure 3.1. Diagram of permittivity and permeability combinations

The second quadrant is composed of materials with a negative permittivity and positive permeability. Radiation in this quadrant will be evanescent. The second quadrant is made up of

metals. The permittivity of a metal can be described by the Drude model, which correlates the carrier behavior in a material with its electromagnetic properties, with the equation:

$$\varepsilon(\omega) = 1 - \frac{\omega_p^2}{\omega(\omega + i\omega_c)} \quad (3.7)$$

where  $\omega_p$  is the metal plasma frequency,  $\omega$  is the angular frequency of the propagating wave,  $\omega_c$  is the metal scattering frequency which serves as a loss term. Assuming that the scattering frequency for the material is much less than the plasma frequency when loss is negligible, it can be seen that as the angular frequency approaches the plasma frequency ( $\omega \rightarrow \omega_p$ ), the resulting permittivity approaches zero. If the angular frequency is below the plasma frequency, the resulting permittivity will become negative. This situation leads to an imaginary refractive index and wave impedance resulting in a large amount of reflection. Similarly, fourth quadrant contains ferromagnetic materials with a positive permittivity and negative permeability which do not allow the propagation of radiation.

However, any material that can belong to the third quadrant is unique because it will exhibit simultaneously negative permittivity and permeability. This combination leads to a real, negative refractive index, real wave impedance, and backward wave propagation inside the material. This can be expressed mathematically in the form of the wave number, given by the equation:

$$k = \omega \sqrt{\varepsilon \mu} \quad (3.8)$$

In order for a wave to propagate, the wave number must be real. For the cases of simultaneously positive and simultaneously negative permittivity and permeability, this condition is met as seen in Figure 3.1.

Perhaps the simplest means of illustrating the effect of a negative index of refraction is through Snell's Law which relates the angles of refraction at the interface of two different materials to the refractive index of each material. Snell's Law is governed by the equation:

$$n_1 \sin \theta_1 = n_2 \sin \theta_2 \quad (3.9)$$

where  $n_1$  and  $n_2$  are the refractive index of different materials and  $\theta_1$  and  $\theta_2$  are the angle with respect to the interface normal vector of the incident and transmitted wave, respectively, as shown in Figure 3.2.

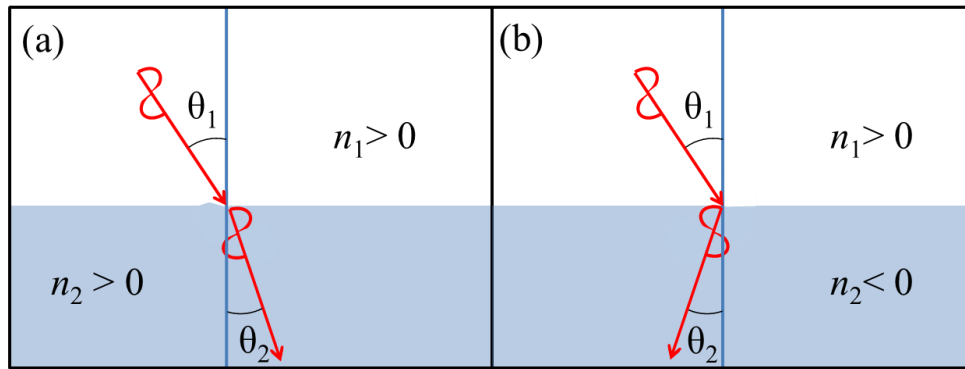


Figure 3.2. Snell's Law for a (a) positive refractive index and (b) negative refractive index.

Since the permittivity and permeability parameters are frequency dependent, the operational range of frequencies for a metamaterial are as well. The major factor in determining the operating frequency of a metamaterial is the size of the subwavelength structures which form the homogenous media. This means that the operational frequency can be scaled mostly based

on the size of these structures which are most often made of high conductivity metals. Decreasing the size leads to a corresponding increase in operational frequency. Unfortunately, the size scaling of metallic structures is limited because the conductivity of the metal will decrease from the bulk value when the size is decreased sufficiently. The breakdown of the scaling process becomes significant in the infrared region, so new methods and materials other than metal conductors are necessary to achieve at the visible frequencies. The expected next step is the replacement of metal resonant elements by superconducting quantum interference structures which could lead to further scaling of metamaterial elements into visible frequencies. Some other perspective alternatives have been suggested which include structured alloys, oxides, carbon nanotubes, and graphene.<sup>80</sup>

Since 2000, new advances have continued to push metamaterial operating frequencies higher; finally realizing operation at visible frequencies in 2007. The graph in Figure 3.3 was published in review article by Soukoulis<sup>81</sup> and shows how the operational frequencies of metamaterials have increased with the open triangles indicating only negative permeability metamaterials and the solid triangles indicating left-handed metamaterials. Aside from the difficulties in achieving higher frequency operation, the resonant nature of the subwavelength structures makes the operational bandwidth of metamaterials usually very narrow. This is another challenge that must eventually be overcome for many applications.

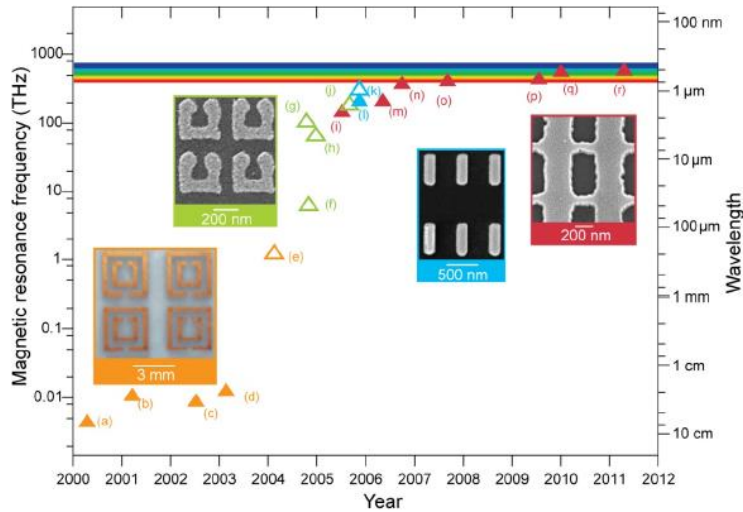


Figure 3.3. Operational frequency of metamaterials by year.<sup>81</sup>

### 3.3. Metamaterial Applications

Over the past decade, the list of potential applications for metamaterials has seen explosive growth. The initial applications that could be fabricated were based firmly in the radio and microwave frequency ranges. This was due to the appropriate sizes for the structures being on the order of millimeters or centimeters. Despite this, however, many ideas for novel applications quickly arose for the entire electromagnetic spectrum. Some of these applications included invisibility cloaks<sup>82,83</sup>, superlenses<sup>84,85,86</sup>, filters<sup>87,88</sup>, modulators<sup>89,90,91</sup>, antenna radomes<sup>92,93</sup>, beam steering optics<sup>94,95</sup>, microwave couplers<sup>96,97</sup>, and waveguide loading for enhanced transmission.<sup>98,99</sup>

A class of metamaterials often referred to as transformation optics allow for the precise control of electromagnetic wave propagation within a system. Transformation optics have so far been the key to the invisibility cloak, superlens, and beam steering applications. Transformation optics rely on the specific placement of the constituent resonant elements onto an imposed

coordinate system. This can be accomplished through a conformal mapping process and enables the metamaterial to bend light around an object in the case of a cloak or beam steering optic.

The same property can also make it possible to achieve theoretically unlimited resolution in the case of a superlens. Resolution is an imaging term indicating the smallest distinguishable feature size. For optical imaging, light is focused onto a specimen and the reflection is collected. Typically, the resolution is determined by the cross sectional diameter at the focal point—or spot size—of the incident light. The spot size is dependent on the wavelength of the light and focus angle. The minimum spot size for an optical microscope is said to be diffraction limited and given by the equation:

$$r = \frac{1.22\lambda}{2(n \sin \theta)} \quad (3.10)$$

where  $r$  is the spot size radius,  $\lambda$  is the wavelength,  $n$  is the refractive index of the media between the lens and the specimen, and  $\theta$  is the half aperture angle.<sup>100</sup> The term  $(n \sin \theta)$  is referred to as the numerical aperture of the objective lens in a microscope.

Realistically, the minimum spot size, and therefore the resolution, for most imaging systems will be somewhere near half of the wavelength of the light. For example, blue light at a wavelength of 475 nm, corresponds to a resolution of about 240 nm which might still be too large to resolve nanostructures such as quantum dots. It is also insufficient for biological samples such as viruses, some bacteria, proteins, and the internal components of human cells. For features much smaller than the wavelength, the reflected light is evanescent in nature and therefore cannot be collected in the far field, meaning at the objective. Metamaterial superlenses

based on transformation optics can break the diffraction limit and resolve features much smaller than the wavelength.

Another class of metamaterials, chiral metamaterials are capable of inducing a much stronger rotation of the polarization of incident waves than possible with natural materials. Chirality was first described by Sir William Thomson (better known as Lord Kelvin) in a famous quote: “I call any geometrical figure, or group of points, ‘chiral’, and say that it has chirality if its image in a plane mirror, ideally realized, cannot be brought to coincide with itself.”<sup>101</sup> Chiral metamaterials can exhibit a negative refractive index.<sup>102</sup> Whereas standard metamaterials that achieve a negative refractive index require two separate resonances to force simultaneously negative permittivity and permeability, chiral metamaterials should be able to exhibit a negative refractive index for one polarization with a single chiral resonance.<sup>103</sup> Chiral metamaterials can also possess properties including circular dichroism<sup>104,105</sup>, giant optical activity<sup>106,107</sup>, and utility in tuning the Casimir force.<sup>108,109</sup>

Chiral metamaterials are designed such that no mirror symmetry exists within the composing matrix of subwavelength resonant elements. This is accomplished through the use of enantiomer elements such as split-ring resonators and gammadions. The absence of mirror symmetry gives rise to a cross-coupling of the electric and magnetic field components of incident circularly polarized waves leading to different refractive indices for oppositely polarized (left and right rotating) waves. The cross-coupling is given by the equations<sup>110</sup>:

$$D = \epsilon E - \frac{i\kappa H}{c} \quad (3.11)$$

$$\mathbf{B} = \frac{i\kappa\mathbf{E}}{c} + \mu\mathbf{H} \quad (3.12)$$

where  $\mathbf{D}$  is the electric displacement field, and  $\kappa$  is the chirality parameter, and the refractive index of a chiral metamaterial is given by the equation:

$$n_{\pm} = \sqrt{\epsilon\mu} \pm \kappa \quad (3.13)$$

where the positive and negative signs are used to distinguish right and left circularly polarized incident waves, respectively. If the chirality parameter becomes sufficiently large, the refractive index will become negative for one of the polarization rotations. These properties have led to applications for chiral metamaterials as polarizers<sup>107,111</sup> and superlenses.<sup>112,113</sup>

Until recently, most of the realized applications for metamaterials were passive. Over the past few years, however, there has been an increasing push to achieve active devices. A review of the subject was recently published by N. I. Zheludev and Y. S. Kivshar in 2012.<sup>114</sup> One of the first active metamaterial devices, reported in 2006, allowed for the modulation of terahertz frequency radiation through the use of an applied electric bias. The device employed an array of gold electric ring resonator elements deposited on a GaAs substrate which collectively work as a Schottky diode. Contacts were deposited on both sides of the array with the resonator elements connected by deposited wire strips that were linked to a contact on one side as shown in Figure 3.4. When no bias was applied, the electric ring resonators did not function because the substrate conductivity was high enough to effectively short circuit the rings. In the case of an applied bias voltage, however, depletion of the GaAs substrate caused it to become insulating allowing a resonance to develop in the rings. The device was shown to be capable of up to 50% amplitude modulation at the resonant frequency.

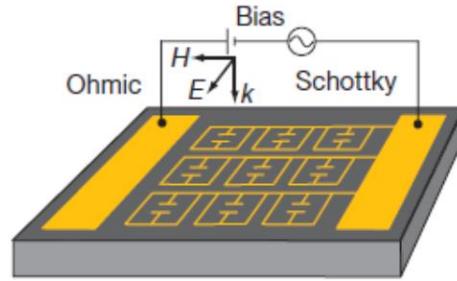


Figure 3.4. Diagram of H. -T. Chen's electric ring resonator-based metamaterial modulator.<sup>115</sup>

Another active metamaterial application is reconfigurable devices that can enable real-time switching or tunability. This has been accomplished by actively changing the position or orientation of the resonant elements with respect to each other<sup>116</sup> and through the displacement of planar arrays relative to other stacked arrays in three-dimensional structures.<sup>117</sup> This type of application was first reported in 2009. In this work, split-ring resonator arrays were fabricated on bi-material cantilevers. The absorption of incident radiation by the split ring-resonators resulted in an increase in temperature which caused a bending of the cantilevers moving the split ring-resonators out of plane.<sup>118</sup> This type of device was suggested to be suitable for detection of T-rays or infrared waves and for temperature sensing.

Microelectromechanical systems (MEMS) have also been effectively utilized for these purposes as actuators<sup>119</sup> and for transmission line tuning.<sup>120,121</sup> However, these different switching systems that are mechanical in nature are limited in switching speeds. Photonic metamaterials, in which switchable, nonlinear dielectrics and metallic resonant elements can be combined, offer significantly faster switching speeds. This is attained by using high-intensity light to alter the plasmonic behavior at the metal-dielectric interface leading to unusual effects such as increased transmission or reflection from the device. Graphene is a particularly well suited material for this type of application. Although single-layer Graphene does show a fast,

broadband nonlinear response, the nonlinear change in transmission is very small. Through the addition of metallic resonators, the fast, nonlinear change in transmission can be increased by an order of magnitude leading to applications including pulse shaping and optical switching.<sup>122</sup>

Magnetoelastic metamaterials are reconfigurable metamaterials in which the resonators can change position due to the Ampere's force caused by other nearby resonators and is balanced by a restoring Hooke force due to the elasticity of the dielectric layer between resonator arrays as shown in Figure 3.5.

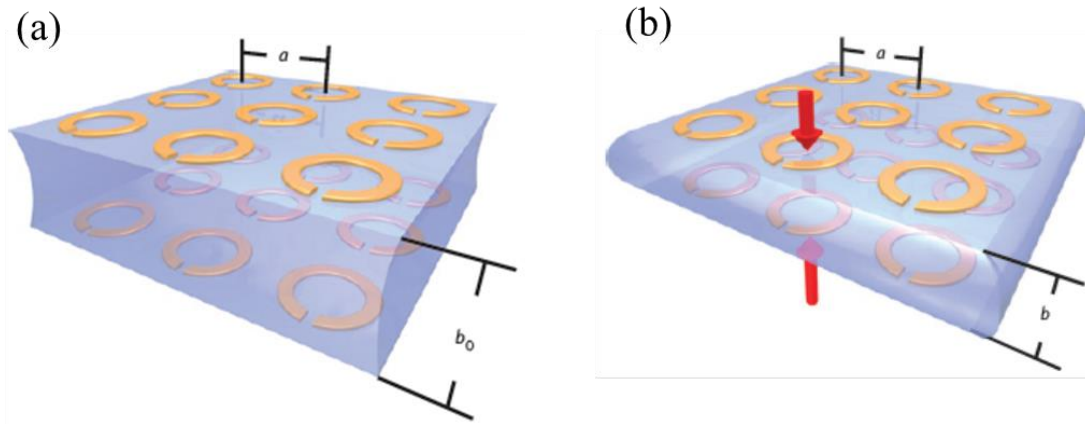


Figure 3.5. Diagram of a magnetoelastic metamaterial showing (a) the unexcited state and (b) the excited compressed state.<sup>123</sup>

In a similar work, a plasmonic metamaterial was shown to be capable of mimicking the adhesive nature of a Gecko toe. When near to a metal or dielectric surface and illuminated by a light source at resonant frequency, the plasmonic metamaterial would experience a strong light-driven force holding it to the surface. Only a few tens of nanowatts per square micron was enough intensity so that the force would overcome the combination of the radiation pressure and Casimir and gravitational forces.<sup>124</sup>

There has also been recent interest in the incorporation of liquid crystals into metamaterial devices to attain a tunable nonlinear response.<sup>125</sup> The refractive index of a metamaterial can be electrically engineered when an applied electric<sup>126,127</sup> or magnetic<sup>128</sup> field (in the form of a wave) can change the orientation of the resonant elements infiltrated with liquid crystals. The benefit of liquid crystals is that they can serve as a control mechanism for metamaterial devices at room temperature with response times in the millisecond range. This is unfortunately much slower than the aforementioned photonic metamaterial type.

Metamaterials can be developed for mechanical waves as well as electromagnetic waves. Currently, much research is also being performed in the area of acoustic metamaterials. Acoustic metamaterials, similar to electromagnetic metamaterials, rely on arrays of resonant elements to achieve their unusual properties. Unlike electromagnetic metamaterials, however, the elements composing an acoustic metamaterial are mechanical resonators. Acoustic metamaterials rely on positive or negative interference of the incident and scattered or reflected waves. Also, whereas electromagnetic metamaterial resonators are sensitive to the lattice parameter for coupling effects, acoustic metamaterial resonators have negligible coupling, and are for the most part unaffected by resonator spacing or the direction of the incoming waves.<sup>129</sup>

Acoustic metamaterials fall into two distinct categories. The first category is called intrinsic acoustic metamaterials. In this type, the size of the resonators is completely decoupled from the wavelength of the incoming waves. Silicon rubber is often used in the construction of intrinsic acoustic metamaterials<sup>130</sup>. The other category is called inertial acoustic metamaterials. This type relies on resonant elements that act as mass spring damper oscillators.<sup>131,132</sup>

Acoustic metamaterials share many of the same types of applications as electromagnetic metamaterials. Perhaps the most widely known is for cloaking of objects. As sonar works off of reflected sound waves underwater, acoustic metamaterials could be developed to make submarines invisible.<sup>133</sup> Other research is aimed at using acoustic metamaterials to make buildings earthquake resistant.<sup>134</sup> Acoustic metamaterials have also been used for perfect sound proofing.<sup>135</sup> Acoustic metamaterial superlenses have been developed as well.<sup>136</sup>

## CHAPTER 4

### TERAHERTZ TIME DOMAIN SPECTROSCOPY

#### 4.1. Description of Operation

As previously stated, the most common application for terahertz frequency radiation is spectroscopy for scientific and research purposes using broadband terahertz time domain spectroscopy systems. Terahertz time domain spectroscopy (THz-TDS) was first developed in the middle of the 1980s.<sup>7,137</sup> Over the past three decades, THz-TDS has seen a steady growth of new applications. The major benefit of THz-TDS is that it can be used to provide spectroscopic information over a large range of frequencies.

Although the number of commercially available THz-TDS systems is growing, these systems tend to be rather expensive given that some of the required components, such as an ultrafast pulsed laser system and lock-in amplifier, do not even come with many these systems. Provided the ultrafast laser system and lock-in amplifier are already on hand, a homemade THz-TDS system can be assembled for much less expense. The basic equipment necessary for this task can be categorized as ultrafast (pump) beam optics, T-ray beam optics, and detection components. The ultrafast optics necessary include several optical mirrors, focusing lenses, a linear delay stage or optical shaker, a polarization dependent beam splitter, and wave plates. An Either an optical rectification crystal or photoconductive antenna emitter, aluminum flat mirrors, parabolic off-axis mirrors and/or polyethylene (PE) or polymethylpentene (TPX) lenses make up the required T-ray beam optics. Either a photoconductive antenna or electro-optic sampling

detection setup can be used for detection. Finally, some type of stage is needed to accurately position the sample in the T-ray beam path.

The THz-TDS system used for the measurements in this work, along with a schematic diagram of the system, is given in Figure 4.1. The system, called the Z-2, has a photoconductive antenna emitter pumped by a Coherent MIRA-900, an ultrafast infrared laser, with maximum average output power of 2 W (at a wavelength of 775 nm) in 120 fs pulses and a repetition rate of 76 MHz. The MIRA-900 is a tunable titanium sapphire based oscillator capable of both continuous wave and ultrafast pulse output in the wavelength range from 700 nm to 1000 nm. The MIRA is pumped by a Coherent Verdi V-12 diode laser with continuous wave output with maximum average power of about 12.5 W at a wavelength of 532 nm. The Z-2 photoconductive antenna emitter high voltage bias (130 V) is gated by a Stanford Research Systems SR830 lock-in amplifier which routes the collected measurement data to a computer.

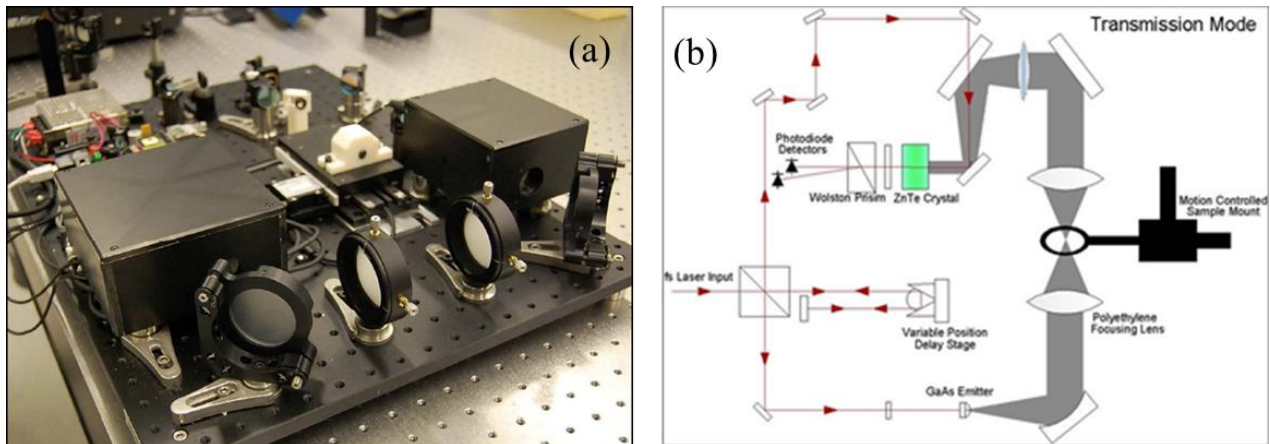


Figure 4.1. (a) Photograph and (b) system diagram of the Z-2 in transmission mode.

In order to explain how the Z-2 operates, it will be helpful to follow the path of an ultrafast pump pulse as it travels through the system. Upon entering the Z-2, the pulse is divided into two separate pulses when it passes through the beam splitter. One of the two new pulses, the

probe pulse, is guided with mirrors to the photoconductive antenna where it used to generate carriers which emit the broadband terahertz pulse. The terahertz pulse is then further guided, again through the use of mirrors, into the electro-optic crystal for detection. The other ultrafast pulse, the reference pulse, is aligned along a variable path length using a linear translation stage. After passing this segment, the reference pulse is then routed through the electro-optic crystal and following Wollaston prism onto a set of photodiodes. The probe and reference pulse paths must be carefully aligned so that they are collinear.

As previously stated in Chapter 2, the refractive index of the electro-optic crystal will change in the presence of an applied electric field. In this case, the applied electric field is in the form of the propagating terahertz pulse. When the terahertz pulse travels through the crystal it changes the refractive index seen by the linearly polarized reference pulse giving it an elliptical polarization. After passing through the crystal, the reference pulse then passes through the Wollaston prism. The Wollaston prism again splits the reference pulse into two separate pulses that are spatially dispersed based on the polarization of the reference pulse. These two pulses then go to the photodiodes.

The system measures the voltage difference between the two photodiodes which is directly proportional to the electric field of the terahertz pulse meaning it contains both amplitude and phase information about the electric field of the terahertz pulse. The terahertz pulse generated by the photoconductive antenna is broadband leading to temporal broadening of the terahertz pulse, which has a pulse width on the order of picoseconds, compared to the probe pulse. By translating the linear stage, the reference pulse can be effectively delayed. This allows the reference pulse to be used to sample the terahertz pulse in time as it passes through the electro-optic crystal.

For this system, a three axis motion controlled stage was used for sample positioning. The stage consists of three individual Newport motorized linear stages. The stage is controlled by a Newport ESP301 three axis motion controller/driver that is connected to a computer for remote control. A PE lens was placed before the sample to focus the terahertz pulses onto the sample followed by an additional PE lens to recollimate the pulses after the sample. A holder consisting simply of thin sheet of stainless steel with small aperture was fabricated for the measurements. The holder was mounted to the stage and aligned such that the maximum signal passed through the aperture indicating it was correctly positioned at the focal point of the terahertz pulse path.

An important figure of merit for this type of system is its signal-to-noise ratio. For this system, a measurement of the terahertz pulse and an identical measurement with the terahertz pulse blocked by a steel plate were performed as shown in Figure 4.2. The pulse amplitude maximum was seen to be 11.56 mV while the maximum of the noise signal was seen to be 4  $\mu$ V. This yields a signal-to-noise ratio of nearly 3000:1. Such systems can reach signal-to-noise ratios of greater than 10,000:1, but these values are largely dependent on the alignment of the system as the noise signal is for the most part constant.

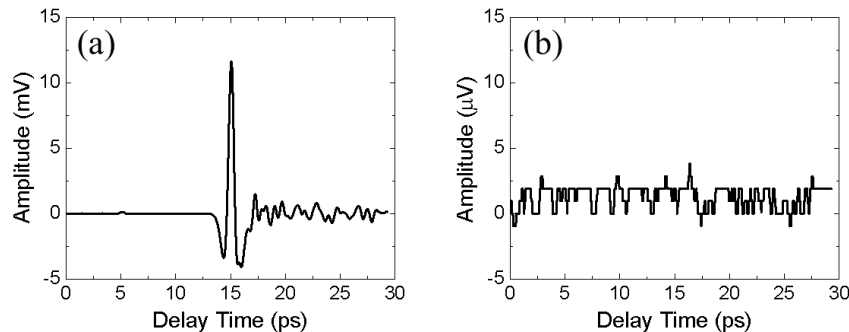


Figure 4.2. Time domain measurement of (a) a terahertz pulse freely propagating through air and (b) the noise signal with terahertz pulse blocked. Note that the scale of the noise signal is given in microvolts as opposed to millivolts.

## 4.2. Reflection Mode System Modification

Transmission mode measurement requires the samples to be either somewhat transparent at terahertz frequencies or thin enough to allow a sufficient level of transmission. Unfortunately, this is not always the case. Reflection mode measurement works in the same way as transmission mode measurement except that the radiation reflected from the sample must make it to the detector instead of the transmitted radiation. Because the system did not have reflection mode capability when installed, it was necessary to modify the system to enable this type of measurement. For the reflection mode modification, a 2 mm thick, high resistivity silicon (HR Si) wafer was added to the system to serve as a terahertz beam splitter. A diagram of the reflection mode system setup is shown in Figure 4.3.

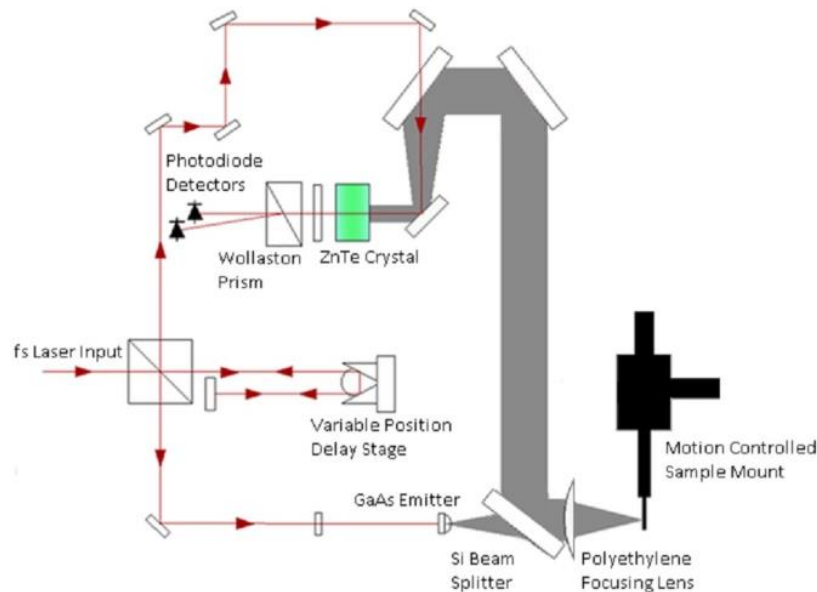


Figure 4.3. Diagram of modified Z-2 system in reflection mode.

The modification was performed by replacing the first aluminum mirror after the emitter with the HR Si beam splitter. The terahertz pulse would exit the emitter box, be transmitted through the beam splitter, and focused onto the sample with a PE lens. The reflected terahertz

pulse would then be recollimated by the PE lens and reflected along the original transmission mode path by the HR Si beam splitter. Although the diagram seems simple enough, the implementation can be quite difficult.

The Z-2 system came with a built-in diode alignment laser which was aligned to the terahertz pulse path while the system was in transmission mode. When the aluminum mirror was removed to begin the modification, two irises were placed on the table and aligned to the built-in alignment laser. Next, the sample stage and holder were positioned on the table such that the holder was normal to the alignment laser to ensure the reflected pulse would have the appropriate propagation vector. Afterwards, the holder was removed from the stage and an additional diode alignment laser was aligned to the two added irises on the table. The HR Si beam splitter was positioned such that the second alignment laser was aligned back along the transmission mode path and incident on the photodiodes. Finally, the PE lens was positioned using the second alignment laser followed by the sample holder being remounted on the stage. Because the HR Si beam splitter divides the terahertz pulse evenly, the best achievable terahertz pulse amplitude with this method is about 25% of the maximum transmission mode amplitude. This is also the case for the signal-to-noise ratio.

#### 4.3. Data Collection and Processing

The Z-2 came with a basic National Instruments LabVIEW program that was designed to remotely control the system. This program is capable of running a single spectroscopic scan during which the delay stage will move from a specified start position to specified end position at a set speed. During this time, the program queries the lock-in amplifier and records the received voltage values in a text (ASCII) file along with the delay stage position for each value. This

process does not yield the fixed interval spacing between data points needed for further processing, so the program then interpolates the raw data into a set with fixed intervals of delay position. The fixed interval delay position data is then converted into delay time data. This is done through the relation between the speed of light and delay distance by simply dividing the distance by the speed of light. This reduces to the equation:

$$t = \frac{d}{75} \quad (4.1)$$

where  $t$  is the delay time in picoseconds and  $d$  is the delay distance in microns. At this point, a fast Fourier transform (FFT) can be performed to yield frequency dependent values of power, amplitude, and phase. The FFT is derived from the discrete Fourier transform which is of the form:

$$Y_k = \sum_{x=0}^{n-1} y_x e^{\frac{-i2\pi xk}{n}} \quad \text{for } k = 0, 1, 2, \dots, n-1 \quad (4.2)$$

where  $Y$  is the transformed frequency dependent data,  $n$  is the number of data points, and  $y$  is the input time domain data.<sup>138</sup> Unfortunately, this is where the utility of the provided software ends. In order to obtain transmission and reflection ratios for a given sample, further processing is required.

When a sample measurement is performed, an additional reference measurement must also be performed. The reference scan should ideally contain all of the identical materials that interact with the terahertz pulse in the sample scan, except for the sample itself. For the measurement of a homogeneous material, such as a bare HR Si wafer, the corresponding reference would be an open air measurement. For a nonhomogeneous (multilayer) sample, such

as a thin film of SiO<sub>2</sub> deposited onto an HR Si substrate, the reference would be the measurement of the bare HR Si wafer. During data processing, the frequency dependent amplitude of the sample is divided by that of the reference to obtain either the transmittance or reflectivity, depending on the measurement mode.

Additionally, because the frequency resolution of the FFT is directly proportional to the size of the time window, or amount of delay time measured, it is beneficial to scan over a longer delay time during the measurement. However, multiple reflections caused by various material interfaces in the terahertz pulse path—including Fabry-Perot reflections and PE lens reflections—crop up in the scans that lead to sinusoidal oscillations in the frequency domain. These oscillations can be removed through a process referred to as zero-padding. For this process, reflection pulses are removed by replacing the time domain data corresponding to the reflections with a constant value near enough to zero to be negligible. Zero-padding produces a smoothing effect on the frequency domain data as seen in Figure 4.4. It can also be used to lower the time required for scans by scanning a smaller time window and using the zero-padding constant to increase the total time window on both sides of the pulse. This is effectively a means of frequency domain interpolation. One must take care to ensure that the time window is not too small, as the additional oscillations that occur directly after the pulse must be collected to obtain accurate results.

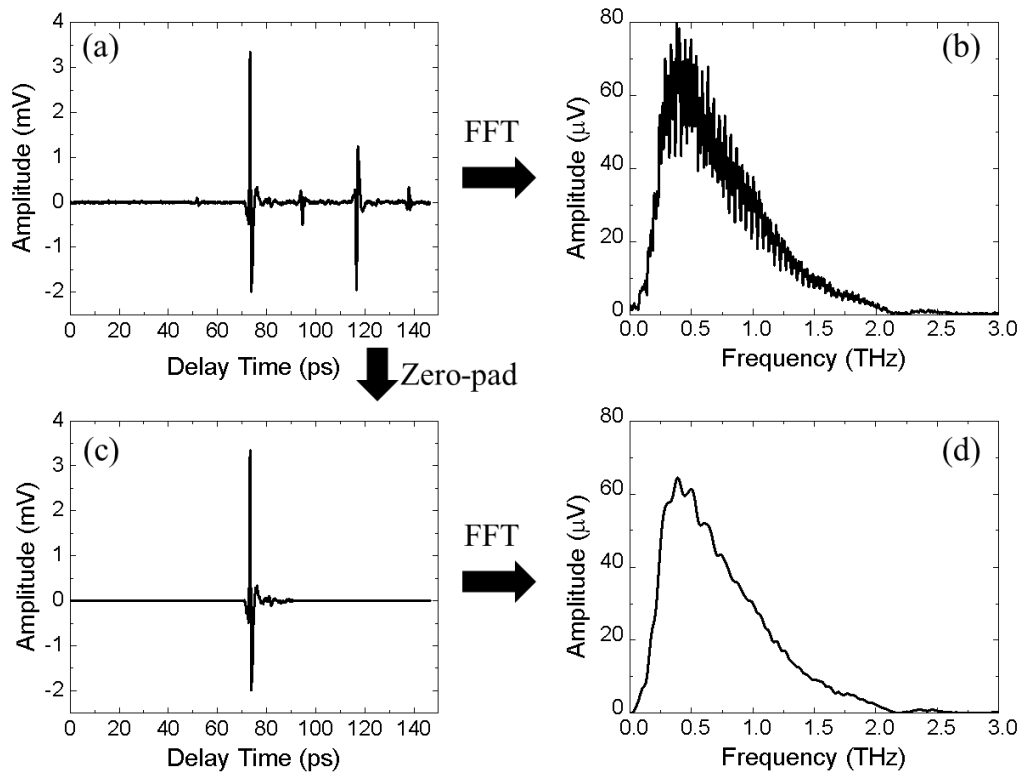


Figure 4.4. (a) Reflection mode time domain amplitude of a copper coated substrate and (b) corresponding FFT amplitude before zero-padding. (c) Zero-padded time domain amplitude based on the same scan and (d) corresponding FFT amplitude.

Additional data processing was accomplished through the use of an additional LabVIEW program that was written by one of my colleagues, William Baughman. This program, which is called THz Analyzer is shown in Figure 4.5. It takes the data files output by the Z-2 program and allows for further processing including the zero-padding process. The program also allows for simultaneous loading of the sample and reference files to generate the sample transmittance or reflectivity.

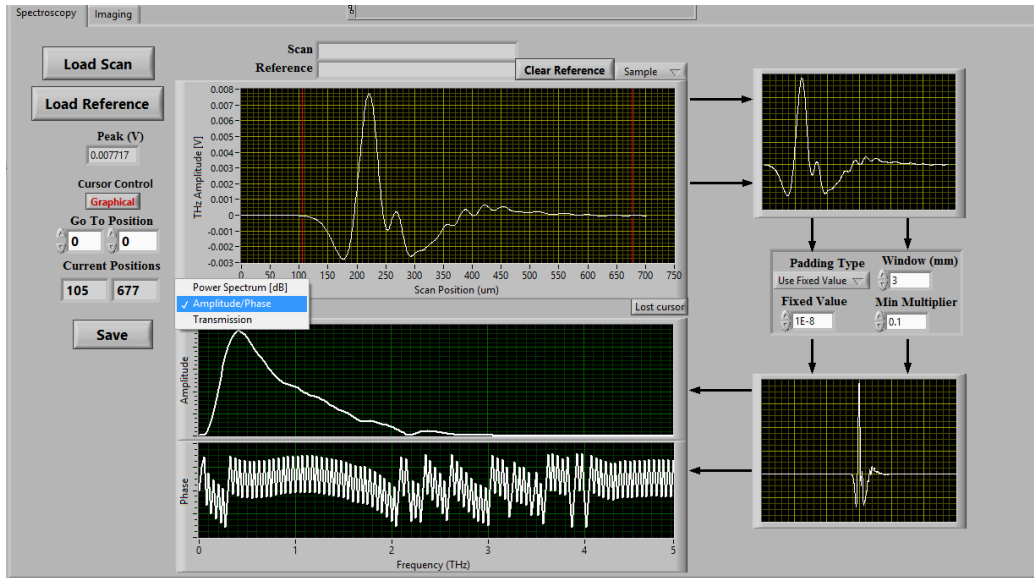


Figure 4.5. THz Analyzer data processing program interface.

Although the zero-padding process can help smooth the frequency domain data, it cannot reduce the narrow absorption lines caused by water vapor in the air. Multiple water vapor absorption lines exist in the spectral region measured by the Z-2 as listed in Table 1. The common method used to remove or at least reduce these absorption lines is purging of the system. To this end, an acrylic enclosure was built for the Z-2 to allow purging of the system with clean dry air or nitrogen.

Water Vapor Absorption Line Frequencies (in THz)			
1.09	1.72	2.26	2.77
1.16	2.17	2.39	2.97
1.67	2.2	2.64	3.01

Table 4.1. The absorption lines in the Z-2 spectral range due to atmospheric water vapor.

Once the purging of the system is started, nitrogen flows into the enclosure forcing the water vapor out. The amount of water vapor left inside the enclosure exponentially decays with

respect to time, which means it can take a good deal of time to purge the system to the point where the water vapor absorption lines have completely vanished. Through testing, it was found that the water vapor absorption lines diminish quickly over the course of the first 15 minutes of purging with further improvement taking substantially longer on the order of an hour. The effectiveness of the purging process is shown in Figure 4.6 which shows the transmitted power spectra at the 1.7 THz water vapor absorption lines before and during purging.

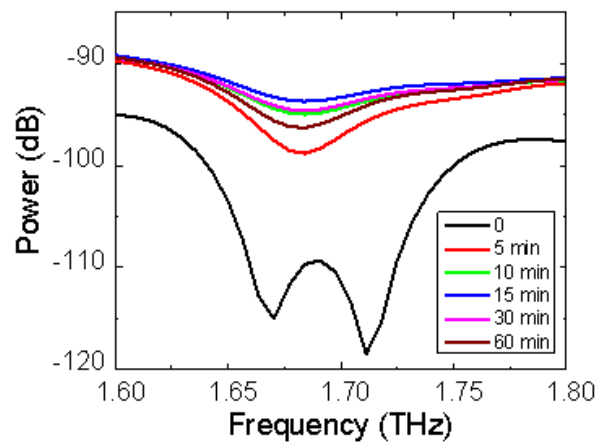


Figure 4.6. Power spectra near 1.7 THz water vapor absorption lines for varied purge times.

#### 4.4. Terahertz Spectroscopic Imaging

Terahertz spectroscopic imaging can be performed with the Z-2 through the use of the motion controlled stage. This is accomplished by raster scanning the sample in the plane normal to the terahertz pulse path and taking spectroscopic scans at set stage position intervals. Each spectroscopic scan serves as the information for a single pixel. By mapping the sample position coordinates, in terms of x-axis and z-axis location, along with the spectroscopic data, an image of the sample can be reconstructed. Because each pixel contains the complete

spectroscopic information, the reconstructed images can reveal information on its composition, density, and other possible characteristics such as refractive index. The following Figure 4.7

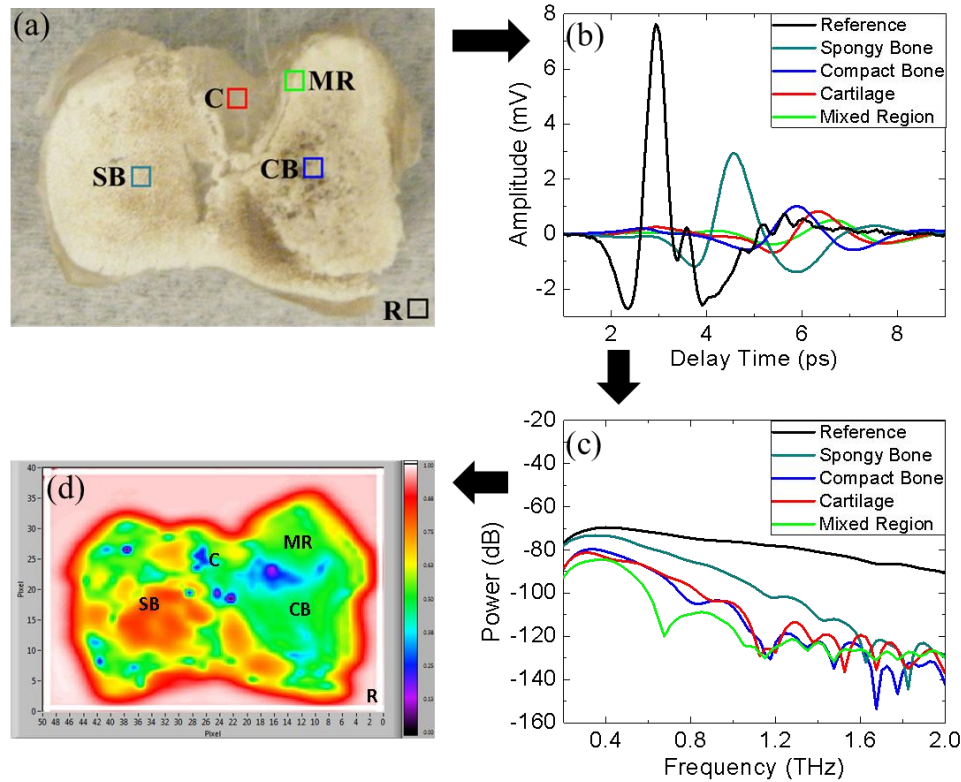


Figure 4.7. (a) Photograph of cross sectioned chicken bone sample with different tissue types labeled. (b) Time domain terahertz amplitude and (c) frequency dependent power spectra for different tissue types. (d) Reconstructed image based on the power spectra at 0.85 THz.

shows one of the images that has been reconstructed based on the THz power transmission through a cross sectioned chicken bone with some typical time domain amplitude and frequency dependent power spectra corresponding to the different types of tissues in a normal bone. This particular image was reconstructed based on the transmitted power at 0.85 THz and is 20 mm by 20 mm. The different tissues are labeled by acronym (based on the first letter of each word such as ‘CB’ for Compact Bone) of the tissue types given in the graph legend. The regions of different tissue type are clearly visible in the image, as well as additional features that are not

visible to the eye. While it remains for upcoming work, dissecting these regions to identify the additional features will enable future identification of these types of features without any need for dissection. This type of imaging, once optimized, promises to be of great benefit to the field of medicine.

Although the spectroscopy program used to control the Z-2 did not have imaging capability, it could be used to image a sample by simply manually moving the sample stage and running individual spectroscopic scans. However, this was a rather inconvenient method for larger images containing many pixels, as it was a time consuming process for the system operator to manually adjust the position for sometimes hundreds of spectroscopic scans. Another of my colleagues, Babatunde Ajilore, wrote an additional LabVIEW program, called TeraVision, used in the laboratory. This program automates the process of adjusting the sample stage position and spectroscopic scanning. Even with the automation, the imaging procedure for large images still takes a great deal of time. It is not uncommon for imaging times to take an entire day or more.

The TeraVision program saves the spectroscopic time domain data for each pixel along with the sample position in a text file which can then be processed. The Terahertz Analyzer program also has this functionality and was used to process the image shown in Figure 4.7 (d). This program can reconstruct images based on the time domain or frequency dependent spectra. It also allows for the zero-padding of the spectroscopic data in each pixel and performs the subsequent FFT before frequency dependent image reconstructions.

Both time domain and frequency dependent images can be reconstructed from the data based on a number of parameters other than the amplitude including time domain pulse delay.

Figure 4.8 shows images reconstructed from both the time domain amplitude and pulse delay. This type of imaging method is particularly useful in the case of imaging biological samples which often tend to be nonhomogeneous and complex in terms of different tissue types. Using multiple image reconstruction methods allows for the ability to detect and visualize subtle, localized differences in the sample composition. In Figure 4.8, the time delay based reconstruction yields a much more distinct separation of the different tissue types. It also makes visible the larger areas of cartilage in the bottom right and upper left regions of the sample that are not apparent in the amplitude based reconstruction. The area of compact bone appears much different in the time delay based reconstruction as well.

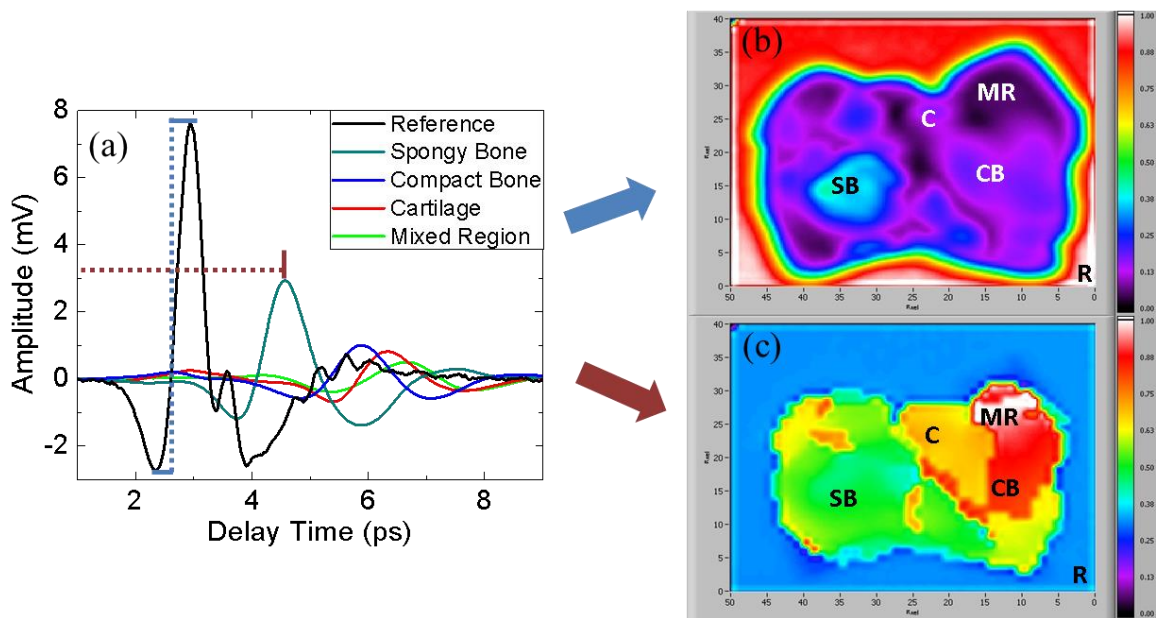


Figure 4.8. (a) Time domain terahertz pulse amplitude for different tissue types contained in the cross sectioned chicken bone sample and the reconstructed images based on the time domain terahertz pulse (b) amplitude and (c) delay time.

## CHAPTER 5

### SPLIT-RING RESONATORS

#### 5.1. Split-Ring Resonator Background

This chapter details the investigation of the effects of three dimensional or multilayered SRR arrays on the SRR resonant response. The SRR geometries were designed through simulation for operation at targeted frequencies in the THz range. The completed design was used to produce a photomask for photolithographic fabrication. Single layer, passivated single layer, and double layer arrays were then fabricated and subsequently characterized by THz time domain spectroscopy.

A SRR can absorb either or both the electric and magnetic components of incident radiation at the appropriate frequency, and is referred to as bi-anisotropic. Bi-anisotropic SRRs can achieve high levels of absorption. In operation, as shown in Figure 5.1, the radiation is incident parallel to the plane of the ring, with the electric field perpendicular to the splits (gaps) in each ring and the magnetic field normal to the plane of the ring. When the magnetic field (or a component of it) is normal to the plane of the rings, it will induce a current in the rings which will move from one side of the gaps to the other. This will in turn create a voltage across the gaps, which at this point are effectively functioning as capacitors. Alternatively, when the electric field (or a component of it) is perpendicular to the gaps, the electric field in the gaps will cause it to build a capacitance with an imposed voltage. This will induce a current in the rings that will in turn induce a magnetic field through the rings. In this particular case, both conditions are met, and the absorption increases drastically. Incident radiation can still be absorbed even if

neither of these conditions exists, at the  $90^\circ$  polarization angle. In that case, referred to as a dipole or half-wave resonance, the capacitance occurs between the internal opposing sides of the rings. Whereas the currents in the SRR flow circularly around the rings in the LC resonance condition, the currents flow symmetrically around both sides of the rings during the dipole resonance condition.<sup>139</sup>

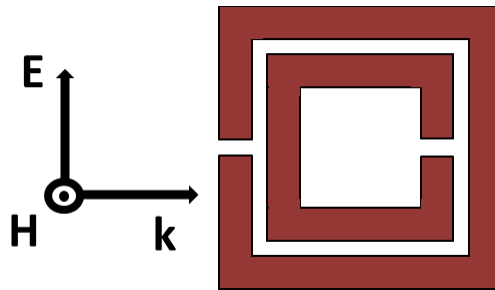


Figure 5.1. Diagram of a split-ring resonator under both electric and magnetic field excitation.

When the SRR absorbs radiation, it exhibits an LC resonance and can effectively be modeled with the simple RLC circuit as shown in Figure 5.2. In the figure,  $R_{\text{loss}}$  is the ohmic loss due to resistance in the rings,  $L_{\text{eff}}$  is the effective inductance of the SRR, and  $C_{\text{eff}}$  is the effective capacitance of the SRR system. Depending on the geometry,  $C_{\text{eff}}$  can become very complex to model as it must take into account the capacitance of both gaps, the capacitance between the rings, and the coupling with other SRRs that are sufficiently close for coupling to occur. It is also important to take into account the presence of a dielectric (which most certainly will be there if only in the form of a substrate) that will have the effect of lowering the resonant frequency. Other than this, the resonant frequency of any SRR, or array of SRRs, comes from the parameters of the system in which it exists. It is determined by the size parameters and spacings of the individual SRR and will hardly be affected by what components, whether electric, magnetic, or both, of the incident radiation are being absorbed.

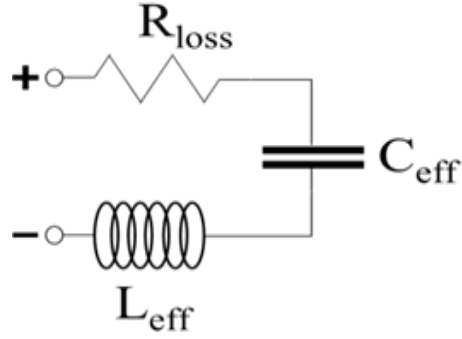


Figure 5.2. RLC circuit model for a SRR.

It is possible to roughly estimate the resonant frequency of a SRR through a simple calculation method, provided a few assumptions are made. In the case of a single, perfectly conducting, square split-ring, as shown in Figure 5.3, through the assumption that the self-inductance of the ring can be roughly approximated by that of a single closed ring which is given by:

$$L = \frac{\mu_0 A}{t} \quad (5.1)$$

where  $L$  is the self-inductance of the ring,  $A$  is the area inside the ring, and  $t$  is the circumference of the ring. The ring capacitance is needed as well, which can be estimated by assuming the sides of the ring and the split in the ring function as parallel plate capacitors. This capacitance is given by:

$$C = C_1 + C_2 = \frac{\epsilon A_1}{d_1} + \frac{\epsilon A_2}{d_2} \quad (5.2)$$

where  $C_1$  and  $C_2$  are the capacitance due to the sides of the ring and the ring splits, respectively,  $A_1$  and  $A_2$  are the area of the parallel surface of the ring side and the ring split, respectively, and

$d_1$  and  $d_2$  are the distances between the ring sides and the ring splits, respectively. The inductance and capacitance values may then be used to solve for the resonant frequency:

$$f_o = \frac{1}{2\pi\sqrt{LC}} = \frac{1}{2\pi\sqrt{\left(\frac{\mu_o A}{t}\right)\left(\frac{\epsilon A_1}{d_1} + \frac{\epsilon A_2}{d_2}\right)}} \quad (5.3)$$

This method requires no information about the system except for the dimensions of the SRR and that the SRR is in an air medium. Again, this is a method rough estimation, but can be performed very quickly and was useful for the initial determination of SRR dimensions to begin simulation.

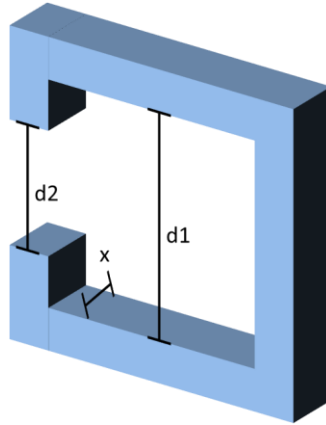


Figure 5.3. Three-dimensional diagram of a SRR used for estimation of resonant frequency.

The work in which Pendry first proposed the SRR was the spark, so to speak, that started the metamaterial fire. In his work, it was posited that just like ordinary materials which are composites of atoms, a material that was a composite of periodic structures could be created that would allow for tuning the material's permeability provided the unit cell lattice constant of this material was much less than the wavelength. This restriction was imposed so that the composite structures could both diffract and refract radiation. The authors then went about detailing the

examination of the magnetic properties of the metal split ring cylinders and “Swiss Rolls” shown in Figure 5.4 to specifically show that the effective permeability could be negative at the LC resonance frequencies of these structures<sup>77</sup>. The authors then proposed the flat disc, circular

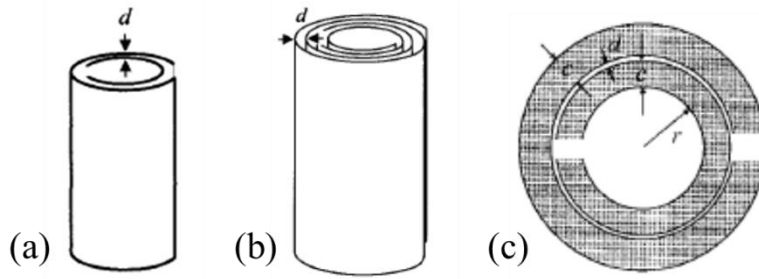


Figure 5.4. Diagram of a (a) split ring cylinder, (b) “Swiss Roll,” and (c) the flat disc split-ring resonator used in Pendry’s report.<sup>77</sup>

SRR based on the top view of the split ring cylinder with the calculation of the resonant frequency and the effective permeability of the structure being:

$$\omega_o^2 = \frac{2}{LC} = \frac{2}{\pi r C_{pul} L} \quad (5.4)$$

where  $C_{pul}$  is the per-unit length capacitance of the SRR and:

$$\mu_{effective} = 1 - \frac{\frac{\pi r^2}{a^2}}{1 - \frac{3L}{\pi^2 \mu_o \omega^2 c r^3 + i \left( \frac{2d\rho}{\omega r \mu_o} \right)}} \quad (5.5)$$

where  $r$  is the radius of the SRR,  $a$  is the lattice constant, and  $\rho$  is the resistance per unit of length of the metal.

Since Pendry’s proposal of the SRR as the first means of tuning permeability, there have been many different geometries of SRRs proposed and tested.<sup>140,141,142,143</sup> The properties of

SRRs have become well known through investigation by numerous groups<sup>144,145,146,147,148</sup> such that SRRs have been incorporated into a variety of passive and active devices.<sup>149,150,151,152,153</sup> Even though the structure of the SRRs used for this work have of course been studied before<sup>146,147,148,149</sup>, no experimental investigation of the effects of passivation and multiple SRR layers of this geometry have been found. The nearest work that was found on the investigation of multiple layers used single ring SRRs.<sup>154</sup> In this work, the lattice constant in all three dimensions was made sufficiently large so that capacitive coupling between both in-plane and out-of-plane SRRs was negligible.

## 5.2. Simulation of Split-Ring Resonators

The SRRs presented in this work were designed through simulation using the RF (radio frequency) module of the finite element method (FEM) based software COMSOL Multiphysics. This program makes possible the simultaneous simulation of multiple physical models provided the appropriate governing and coupling relations (equations) are known. FEM is based on choosing basis functions which only have non-zero values over small, specific subdomains. These subdomains are referred to as elements. Once a model is built, it is broken up into a mesh of triangular shaped elements for two-dimensional models or tetrahedral shaped elements for three-dimensional models. The basis functions are then solved for each element and correlated to yield a solution for the entire system.

In beginning the SRR simulations, the geometrical model of the SRR was built in a similar fashion as would be performed in any standard computer-aided drafting software, such as National Instruments Inventor or Dassault Systems SolidWorks. The basic two-dimensional geometry was built using rectangles. Then the planar SRR face was extruded to create the solid

structure as shown in Figure 5.5. Next, the Si substrate was added in the same manner. For simulations of the passivated and dual layer SRR arrays, a polyimide layer was added. A second SRR was also added for the dual layer simulation.

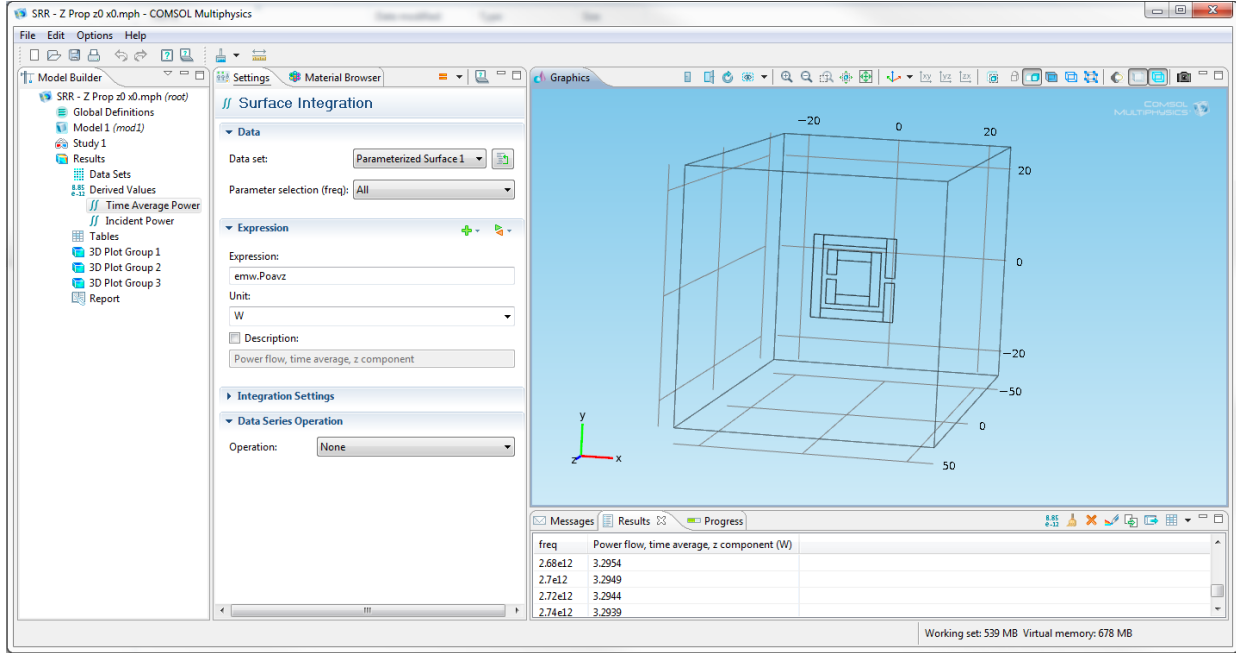


Figure 5.5. Split-ring resonator built in COMSOL Multiphysics.

Once the geometrical model had been built, the materials library of the software was used to assign material properties to the SRR, substrate, and polyimide when required. The next step in setting up the simulation was to setup the physical system. For this, the software requires the selection of an equation. For the simulations performed for this work, the built-in wave equation was used:

$$\nabla \times \mu_r^{-1} (\nabla \times \mathbf{E}) - k_0^2 \left( \epsilon_r - \frac{i\sigma}{\omega\epsilon_0} \right) \mathbf{E} = 0 \quad (5.6)$$

where  $\mu_r$  is the relative permeability,  $\varepsilon_r$  is the relative permittivity, and  $k_o$  is the free space wave number. Then a radiative source parameter  $E_o$  with a value of 1 V/m are added to the model which will be used to scale through a specified range of frequencies.

At this point, the model boundary conditions should be applied. The boundary conditions must be carefully selected based on the geometry of the sample. For the SRR simulations here, periodic boundary conditions (PBC) were used. PBCs allow for each boundary to which they are applied to appear as if it was the boundary on the opposing side of the model. PBCs are appropriate for models which do not exhibit mirror symmetry. COMSOL Multiphysics has built-in functionality for PBCs by forcing the electric field to the value at the opposing side. The sixth and final boundary condition should be opposite the radiative source and set as a scattering boundary condition (SBC) through the equation:

$$\mathbf{n} \times (\nabla \times \mathbf{E} + E_b) - ik\mathbf{n} \times (\mathbf{E} \times \mathbf{n}) = -\mathbf{n} \times (E_o \times (ik(\mathbf{n} - \mathbf{k}_{dir})))e^{-ik_{dir} \cdot \mathbf{r}} \quad (5.7)$$

where  $E_b$  is the scattered electric field,  $k_{dir}$  is the direction of wave propagation, and  $r$  is the distance from the radiative source. Finally, the model is broken into small tetrahedral elements. This process is referred to as adding a mesh to the model. The model with mesh added is shown in Figure 5.6. After this, the simulation is ready to be started.

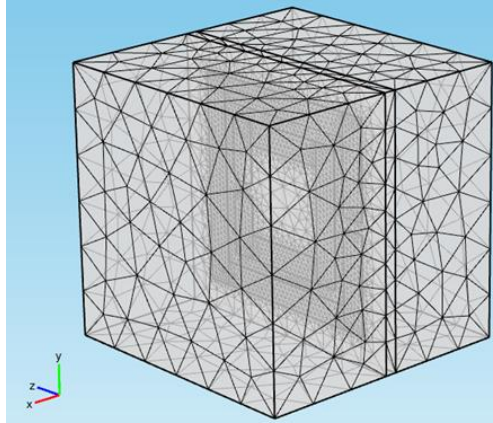


Figure 5.6. SRR simulation model with mesh added.

Once the simulation has completed, the localized electric or magnetic fields, current densities, power flow, and other quantities are able to be visualized through the software interface. Of particular use is the ability to generate slices inside of the simulated system that show field densities as seen in Figure 5.7.

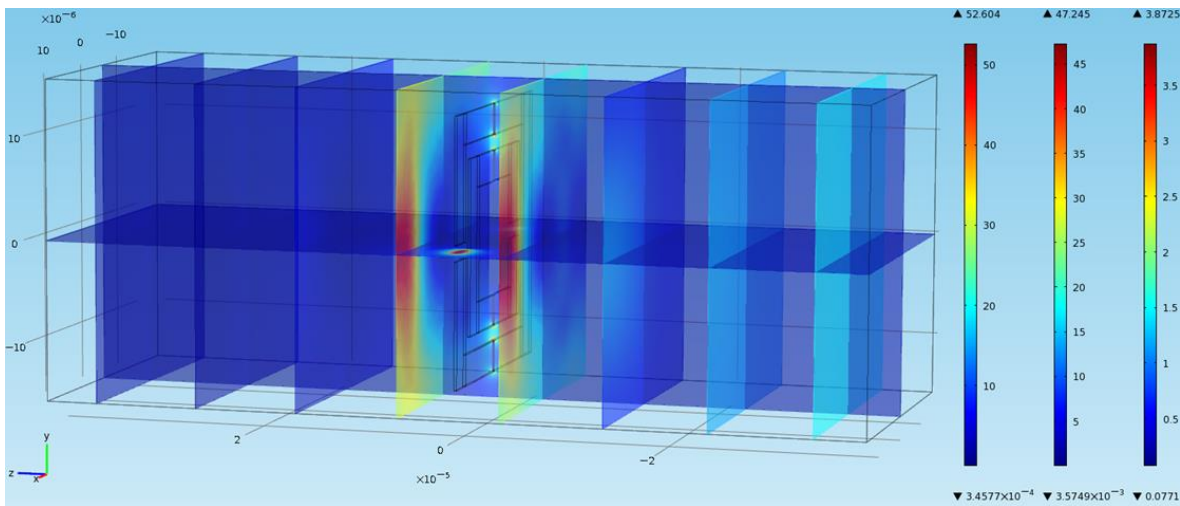


Figure 5.7. Simulation result showing slices of the electric field density in the split-ring resonator system.

The simulation for the SRRs in this work was performed so that the software can obtain the simulation results for each frequency in the range from 0.2 THz to 2.2 THz with a frequency

resolution of 0.02 THz. Although the software can display the three-dimensional images quite well, it can sometimes be difficult to visually distinguish valuable details on the two-dimensional screen. For this reason, it is often advantageous to view the system two-dimensionally. Figure 5.8 shows a two dimensional view of the simulated electric field density in near proximity to the SRR as the incident frequency is scaled from below to above the resonant frequencies.

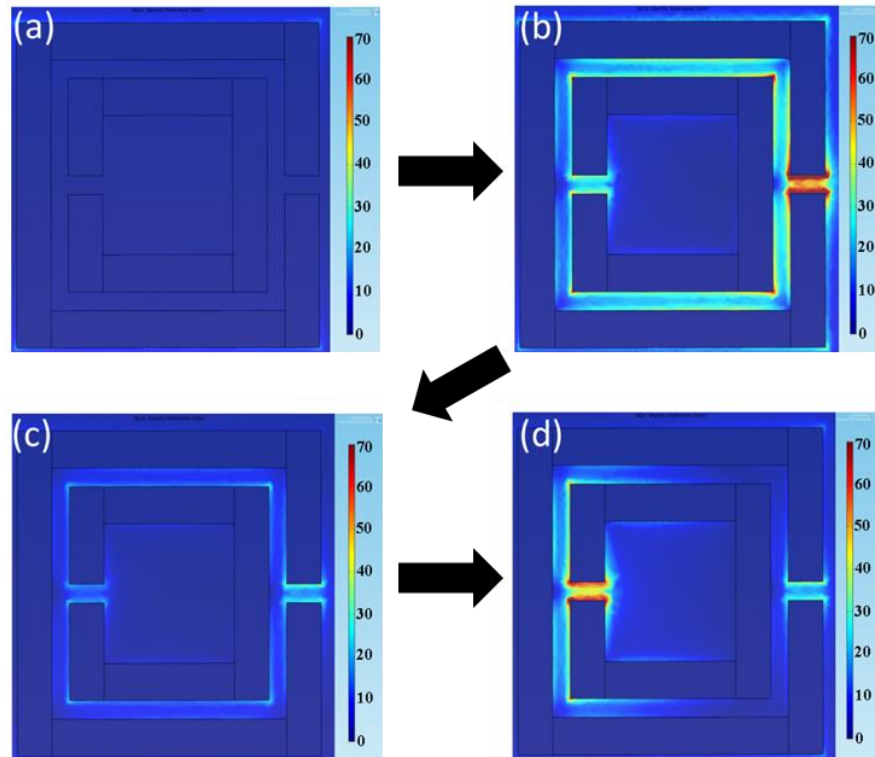


Figure 5.8. Simulation result showing the electric field density in the split-ring resonator system as the source frequency increases from (a) below resonance through (b) the first LC resonance and (c) between resonant frequencies to the (d) second LC resonance.

During simulation, the COMSOL software calculates the electric field, from which additional field quantities can be obtained, at each frequency interval. The electric field can then be used to determine incident power from the equation:

$$P_i = \frac{|E_o|^2 A}{2\eta} \quad (5.8)$$

where  $P_i$  is the incident real power and  $A$  is the area of incidence normal to the wave vector. By integrating time average power component parallel to the wave vector, the transmitted power for each frequency can also be obtained. Evaluating the ratio of the incident power to the transmitted power yields the transmittance which will be used later in this chapter for comparison with measurement. Figure 5.9 shows the simulated transmittance, reflectivity, and absorbance for array of SRRs as calculated by COMSOL.

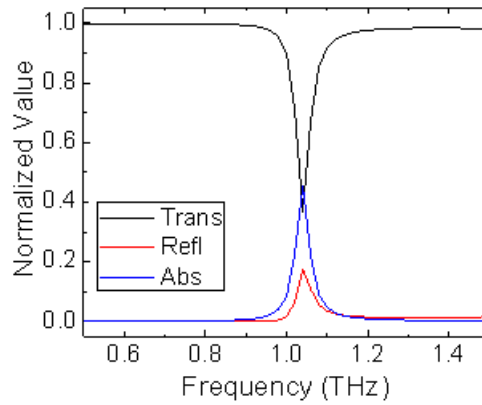


Figure 5.9. Simulation result showing the calculated transmittance, reflectivity, and absorbance for a SRR array.

Based on these simulation results, the experimental dimensions of the SRRs to be fabricated were selected to target frequencies in the range from 0.2 THz to 2.5 THz, as seen in Table 5.1, with the dimensions shown in Figure 5.10.

Frequency (THz)	Dimensions ( $\mu\text{m}$ )					
	<b>a</b>	<b>b</b>	<b>d</b>	<b>g1</b>	<b>g2</b>	<b>w</b>
0.50	15.00	5.00	2.00	2.00	2.00	4.00
0.75	11.00	5.00	1.50	1.50	1.50	3.00
1.00	7.00	5.00	1.00	1.00	1.00	2.00
1.00	7.00	5.00	1.00	3.00	5.00	2.00
1.00	7.00	5.00	1.00	5.00	9.00	2.00
1.00	7.00	5.00	1.00	7.00	13.00	2.00
1.50	5.00	5.00	1.00	1.00	1.00	1.00
2.00	3.50	5.00	1.00	1.00	1.00	1.00

Table 5.1. Unit cell dimensions by targeted frequency.

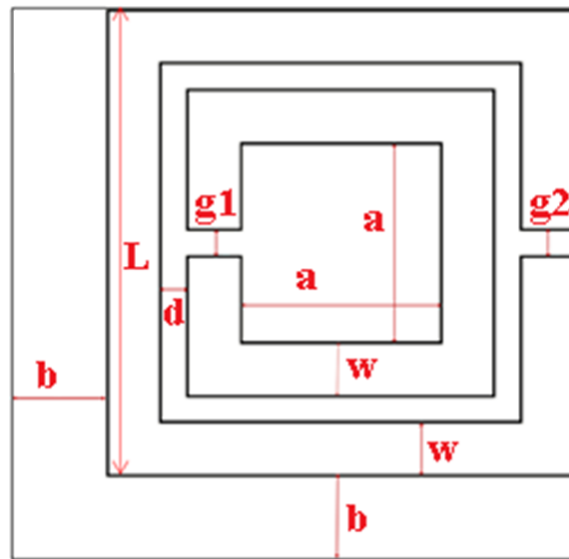


Figure 5.10. Diagram of the unit cell parameters for the fabricated split-ring resonator arrays.

### 5.3. Split-Ring Resonator Fabrication

The first step in the fabrication process was designing the mask. From the previous table giving size geometries, eight SRR arrays, one for each of the sizes measuring ten SRRs wide by 1 cm long, were placed in a grid pattern with enough space in between the arrays so that after fabrication, they could be easily separated as seen in Figure 5.11. A positive photolithography process was desired so that better fabrication resolution (smaller feature sizes) could be obtained. The mask was designed as a dark-field mask, meaning that the patterns were transparent with the rest of the surface opaque. Metals used for electron beam evaporation (E-beam) deposition were chromium and copper, where only a thin 15 nm layer of chromium was used as an adhesion layer for the copper. Finally, a substrate with high resistivity was needed to allow maximum THz transmission and to prevent a short circuit condition of the ring gaps. The same 2 mm thick, 2” diameter HR Si wafers ( $>10 \text{ k}\Omega/\text{cm}$ ) were used as a substrate.

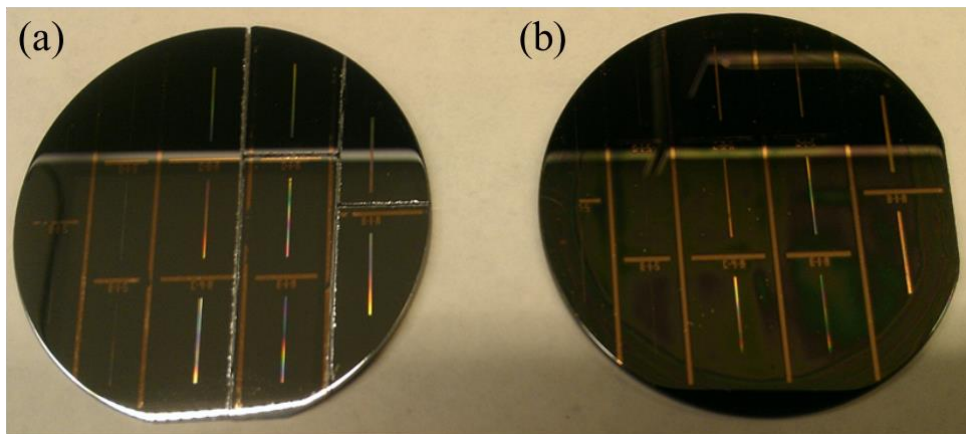


Figure 5.11. Pictures of (a) the single layer SRR arrays and (b) the double SRR layer arrays after fabrication.

The spin coating was performed using a Solitec 5000 series spin coat machine. Shipley S-1808 positive photoresist was used for spin coating. The spin coating process requires the

wafer surface to be as clean as possible. The standard process used for wafer cleaning in the was to spin the wafer at 300 RPM for 10 s while spraying acetone onto it, followed by spinning at 400 RPM for 10 s with a combination of acetone and isopropyl alcohol for the first 5 s, and then only isopropyl alcohol for the remaining 5 s. This is followed by a 30 s spin at 2500 RPM to evaporate all of the remaining liquid. This process worked well for removing most of the visible debris from the wafer, but many times it would be noticed that the resist would still form streaks during the spin. As a result, sonication in an acetone bath for 5 min followed rinsing with isopropyl alcohol and drying with a nitrogen gun was implemented before mounting the wafer for spin coating. Although occasional streaks still occurred, it did yield a noticeable decrease in the overall amount of faulty spin coats.

Through testing of the thickness of the S-1808 from different spin speeds, the optimum spin speed was found to be 3000 RPM for a time of 30 s, which corresponded to a 0.8  $\mu\text{m}$  thick layer of photoresist as tested by a Dektak profilometer. The initial target for SRR thickness was 250 nm, and since a lift-off process was planned, the photoresist needed to be at least three times as thick. However, as the photoresist layer became thicker, feature resolution decreased, so from this trade-off, 0.8  $\mu\text{m}$  was selected.

The next step in the process was a soft bake of the resist. According to the manufacturer, a bake time of 30 s was recommended, and subsequently attempted. After the 0.8  $\mu\text{m}$  layer of photoresist had been deposited on the Si wafer and soft baked, a MA-6 Karl Suss Mask Aligner tool was used to perform the exposure. The manufacturer recommended exposure time was 3 s, which was attempted first. Then the exposed film was developed in a Microposit MF-319 developing solution for 60 s followed by a 90 s submersion in a deionized water bath. This yielded the patterns shown in Figure 5.12.

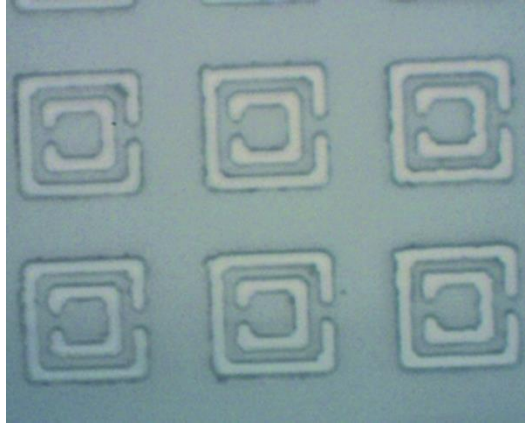


Figure 5.12. Optical microscope picture of SRR patterned photoresist.

The following step was E-beam deposition of chromium and copper onto the resist. As chromium is routinely used in the clean room, the standard procedure was followed with results conforming well to expectation. According to the crystal oscillator in the E-beam, the deposited thickness of chromium was 15 nm. This was followed by a 185 nm copper deposition that was performed without breaking the vacuum seal of the chamber. Copper is not an available source, so it was necessary to tune the parameters for copper deposition including soak times and powers to first melt and then start evaporation of the source material.

After the deposition was completed, lift-off was performed by placing the substrate into a photoresist remover (Microposit Remover 1165) solution bath for 20 min. This removed all of the resist as well as the copper that was on top of the resist leaving on the copper SRRs that were adhered to the substrate. At this point, the single layer arrays were complete. The procedure was duplicated two more times to have the bases for the passivated and double layer arrays.

DuPont PI-2610 polyimide was used as the dielectric spacing layer. Polyimide does not typically adhere well to smooth surfaces such as silicon wafers or metals. It was therefore necessary to use an adhesion promoting agent. DuPont VM-651 was used for this purpose. It

comes in a concentrated liquid form that must be mixed at a specific concentration of 0.1% in deionized water and shaken vigorously. This solution was then drip coated onto the static wafer with the arrays and let stand for 20 s. The wafer was then spun at 3500 RPM for 45 s to remove the additional solution. This process should leave several monatomic layers of the adhesion promoter on top of the wafer.

Next the PI-2610 was drip coated onto the wafer, spun at 400 RPM for 5 s to spread the polyimide, and spun at 3500 RPM for 30 s to thin the layer. The wafer was then soft baked at 85°C for 90 s on a hot plate. The wafer was next hard cured at 350°C for 30 min in a nitrogen purged furnace. This process provided a 1.7  $\mu\text{m}$  polyimide layer and could be repeated to achieve a desired thickness through variation of the spin speeds. For this purpose, only a single layer was necessary, however, the process for achieving desired thicknesses by depositing multiple layers will be discussed in Chapter 6.

At this point the passivated layer arrays were completed. The additional wafer then had another layer of adhesion promoter deposited followed by a 15 nm layer of  $\text{SiO}_2$ . Finally, the same initial array fabrication procedure was repeated to get a second layer of arrays on top of the polyimide layer yielding the double layer arrays. Figure 5.13 shows optical microscope pictures of the (a) single layer, (b) passivated, and (c) double layer arrays. Figure 5.13 (c) is focused on the lower layer of rings. The SRR arrays were also viewed by scanning electron microscope as seen in Figure 5.14.

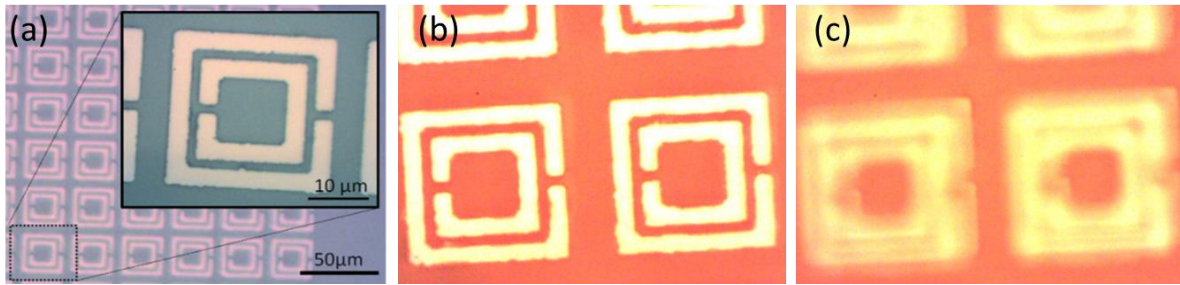


Figure 5.13. Optical microscope pictures of (a) a single layer SRR array, (b) a passivated SRR array, and (c) a double SRR layer.

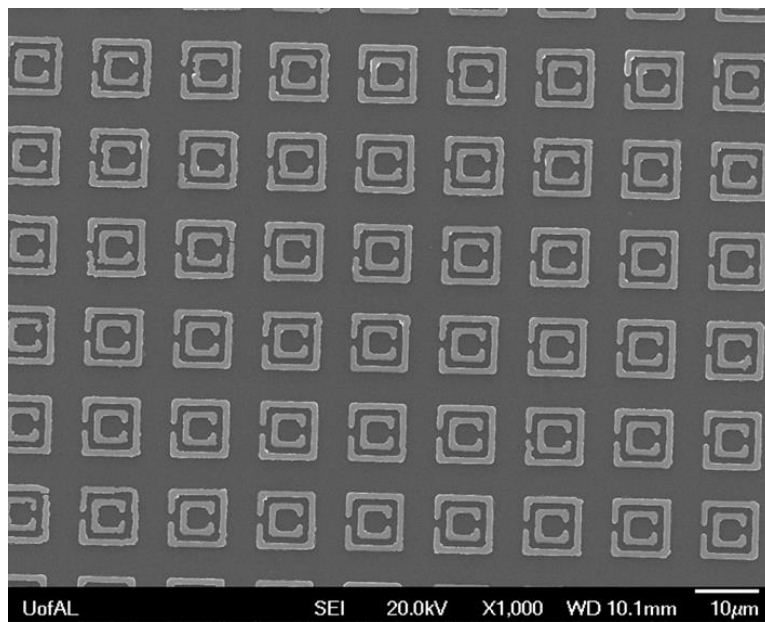


Figure 5.14. Scanning electron microscope image of a SRR array.

#### 5.4. Split-Ring Resonator Measurement Procedure

The SRR orientations were varied between measurements such that the electric field absorption would be isolated with no contribution from the magnetic field. This was achieved by maintaining normal incidence of the THz beam onto the arrays and measuring at two rotations about the propagation vector. The first measurement in this series had the electric field spanning (perpendicular to) the ring gap, which allowed for maximum absorption of the electric field. The second measurement had the electric field pointing through (parallel to) the ring gap which minimized the absorption of the electric field as can be more clearly visualized with the following Figure 5.15.

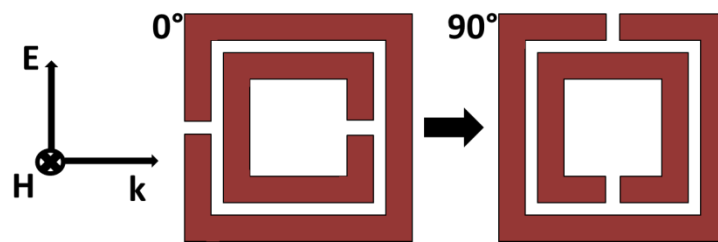


Figure 5.15. Diagram of the split-ring resonator unit cell structure showing the change in orientation during rotation with respect to the incident wave vector.

An additional set of measurements designed to isolate the magnetic field absorption of the SRRs with no contribution from the electric field component as shown in Figure 5.16 was also performed. The first measurement in this series had the SRRs oriented so that the magnetic field was normal to the plane of the rings with the electric field parallel to the ring gap, which allowed for maximum absorption of the magnetic field and minimum absorption of the electric field. The second measurement maintained the electric field orientation parallel to the ring gap by rotating the SRR about the electric field vector which led to minimized absorption of both the magnetic and electric field components.

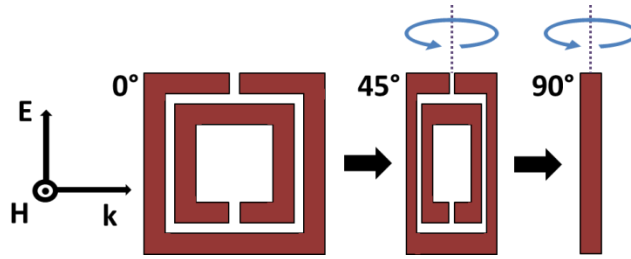


Figure 5.16. Diagram of the split-ring resonator unit cell structure showing the change in orientation during rotation with respect to the electric field vector.

### 5.5. Split-Ring Resonator Results

Figure 5.17 (a) shows the initial orientation for a SRR with relation to the incident field vectors, which we refer to as  $0^\circ$ , at which we expected to see the LC resonances. The arrays were then rotated  $90^\circ$  about the propagation. This rotation minimized the electric field interaction in the SRR gaps so that only the strong resonance due to the induced dipoles is visible. Figure 5.17 (b) shows the transmittance spectra for both  $0^\circ$  and  $90^\circ$  rotations of a nonpassivated SRR array with  $L=35\mu\text{m}$ . The normalized transmittance spectrum was obtained by dividing the frequency dependent amplitude transmitted through the array by the amplitude transmitted through a reference bare Si wafer, so unity means 100% transmission. At the  $0^\circ$  rotation, both the 0.45 THz and 0.88 THz LC resonant frequency absorptions are visible with the LC resonance of the inner ring at 0.88 THz significantly greater than that of the outer ring and the dipole resonance clearly visible at 1.53 THz. Both LC resonant absorptions disappeared while the dipole resonant absorption was broadened and shifted to 1.03 THz for the  $90^\circ$  rotation measurement.

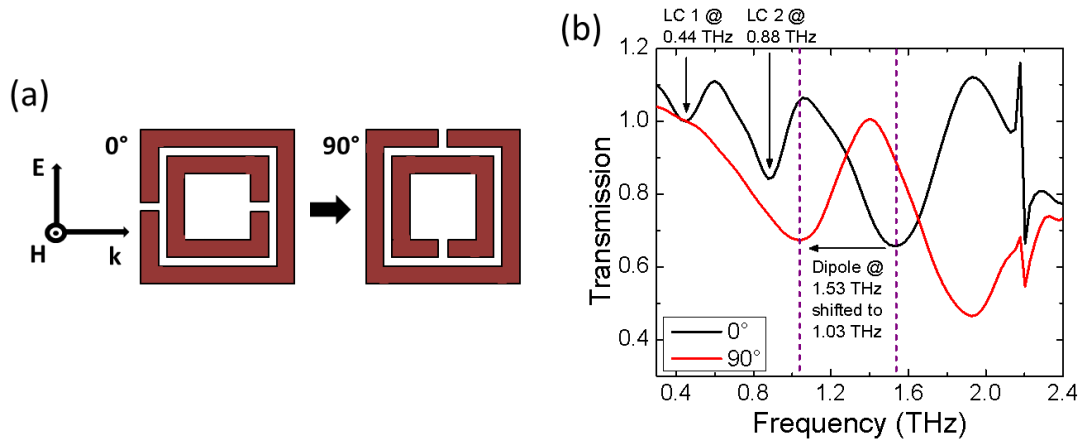


Figure 5.17. (a) Diagram of SRR orientations during measurement for clarity and (b) the corresponding measured transmittance for each orientation.

The measurements from the second set of rotations that were designed to minimize the electric field contribution to the absorption are shown in Figure 5.18. The measurement corresponds to a single layer array with SRR outer length of  $L=35\ \mu\text{m}$ . The array was measured at angles of  $0^\circ$ ,  $30^\circ$ , and  $55^\circ$ , instead of those previously listed. This was necessary, due to the sample geometry. Because the arrays were so thin in the beam cross section, it was impossible to see a valid signal at severe angles where most of the beam was clipped by the substrate. Even so, the dipole resonance is still clearly visible at the measured angles. However, no evidence of the LC resonance was seen for this measurement series. All of the rest of the SRR measurements discussed following are focused on the arrangements where the magnetic field component of absorption is kept minimized with the wave vector held constantly normal to the plane of the rings.

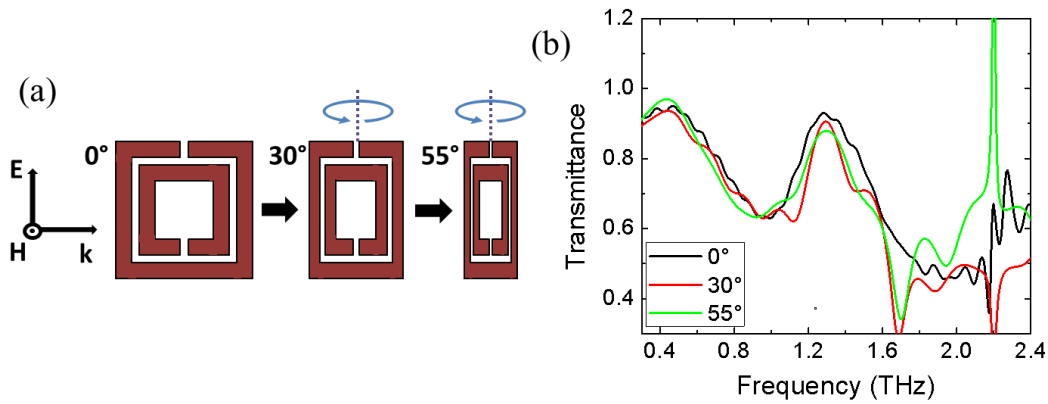


Figure 5.18. (a) Diagram of SRR orientations during measurement for clarity and (b) the corresponding measured transmittance for each orientation.

The simulated and measured transmittance spectra for a single layer array with SRR outer length of  $L=35 \mu\text{m}$  are given in Figure 5.19 at both rotations (a)  $0^\circ$  and (b)  $90^\circ$ . For the  $0^\circ$  SRR rotation, the measured outer and inner ring LC resonant frequencies, at 0.45 THz and 0.875 THz, respectively, were in good agreement with those from the simulation even though transmission dips were not as strong as expected from simulation. The dipole resonance at 1.5 THz was also visible and in agreement with the frequency in the simulation although it had reduced strength as well. At the  $90^\circ$  rotation, the outer ring dipole resonance was seen at 1.1 THz. This also matched the simulation.

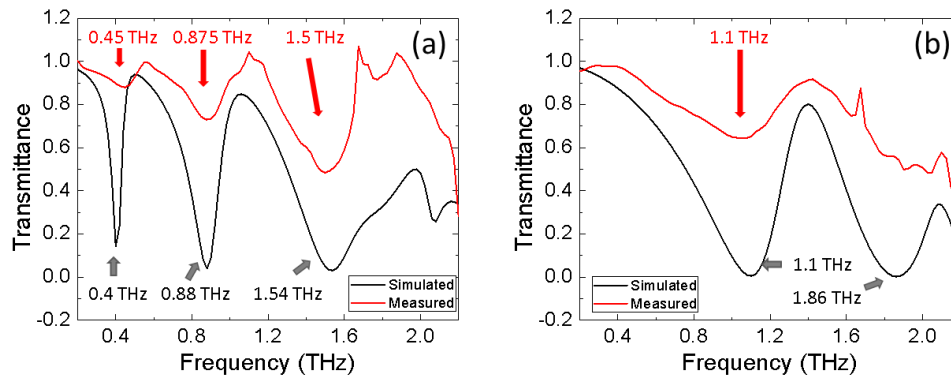


Figure 5.19. Simulated and measured transmittance spectra for a single layer array with SRR outer length of  $L=35 \mu\text{m}$  at both rotations (a)  $0^\circ$  and (b)  $90^\circ$ .

The resonant frequencies were seen to be tunable by varying the size parameters of the SRR geometry. The change in outside edge length from 35  $\mu\text{m}$  to 26  $\mu\text{m}$  effectively shifted the first resonance by 0.18 THz from 0.45 THz to 0.63 THz and the second resonance by 0.37 THz from 0.88 THz to 1.25 THz, as seen in Figure 5.20(a). The addition of the passivation layer to the first layer of SRRs caused a red shift of the resonance frequency due to the change in permittivity in the ring gaps as expected. The addition of the second layer of SRRs on top of the passivation layer did not yield a noticeable shift in resonance frequency although it did result in a small increase in the absorption at the first resonant frequency. These results can be seen in Figure 5.20 which gives the transmittance of (a) two single layer arrays, (b) two passivated arrays, and (c) two double layer arrays with the red and green traces representing SRRs with outer lengths of 35  $\mu\text{m}$  and 26  $\mu\text{m}$ , respectively.

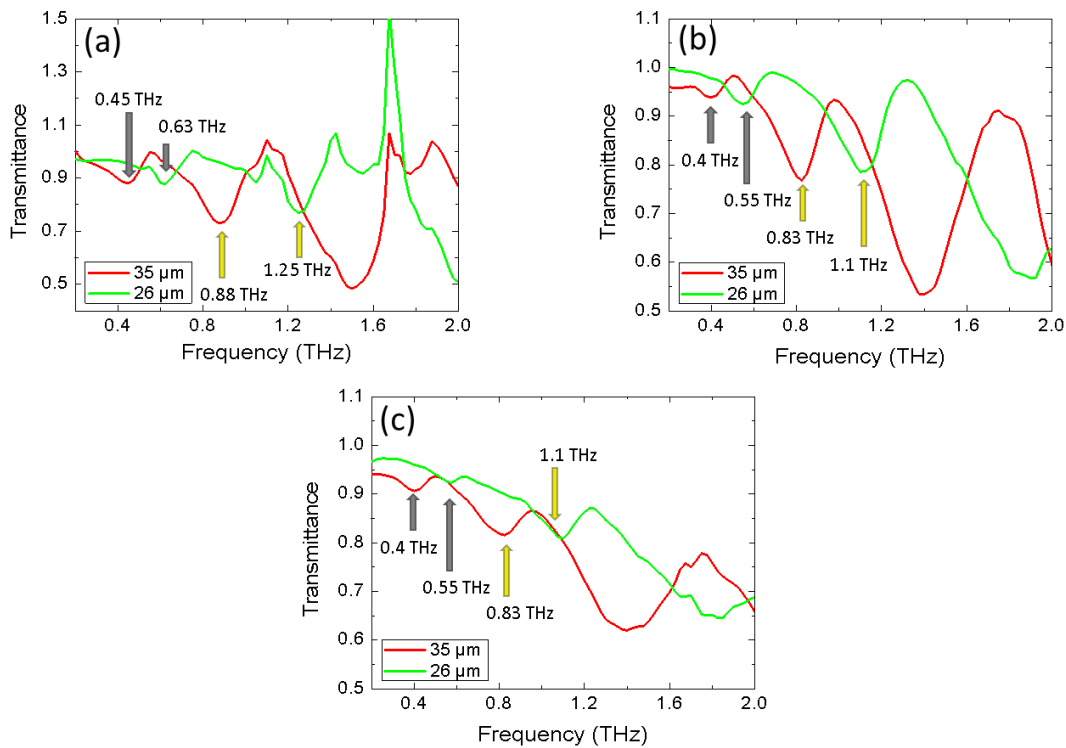


Figure 5.20. Transmittance of (a) single layer arrays, (b) passivated arrays, and (c) dual layer arrays. Red and green traces for SRR outer lengths of 35  $\mu\text{m}$  and 26  $\mu\text{m}$ , respectively.

Identical single layer SRR arrays were also fabricated using gold with a chromium adhesion layer for the rings on a high resistivity Si substrate. Any shift in the first LC resonance is not detectable within the resolution of the Z-2 system. The transmittance of the gold SRR array clearly has a small shift to higher frequency in the second LC resonance compared to that of the copper SRR array. The same is the case for the dipole resonance. Although visible, these shifts are only barely large enough to be detected. For this reason, it was decided that the difference in the fabrication using copper would be more advantageous as the cost of copper is much less than that for gold. The result of the measurements is seen in Figure 5.21.

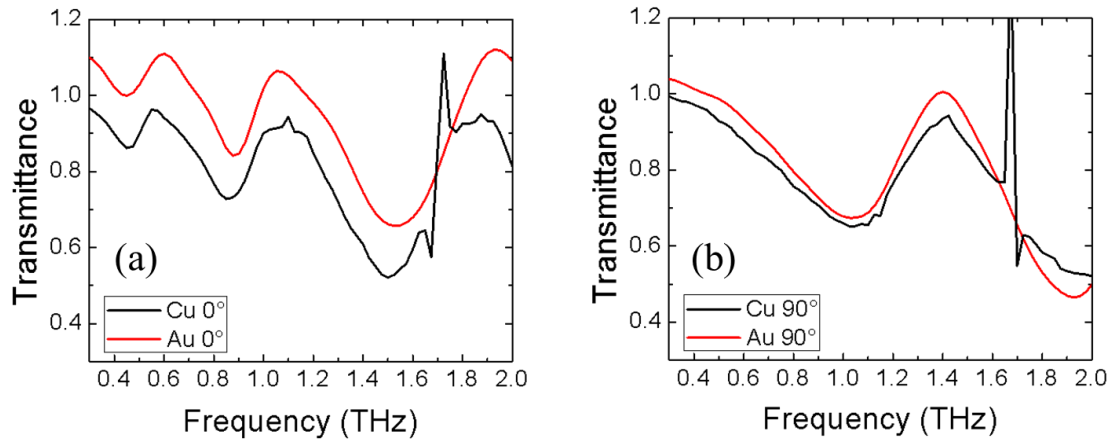


Figure 5.21. Measured transmittance of copper and gold SRR arrays at (a) 0° and (b) 90°.

Initially, a 2 inch diameter, 250  $\mu\text{m}$  thick silicon wafer with much lower resistivity ( $\sim 100 \Omega/\text{cm}$ ) was used for the substrate. The SRR arrays fabricated with the lower resistivity substrate exhibited a no distinct resonances in transmittance. The cause for this was thought to be the short-circuiting of the resonator through the substrate. Additionally, single layer SRR arrays with entirely chromium rings were fabricated, but yielded what appeared to be a very uniform attenuation of the entire transmittance spectra without distinct resonances as well, but may have exhibited the dipole resonance. It is suspected that the conductivity of the chromium composing

the SRRs was too low which may have caused a substantial broadening of the absorption. More on this broadening effect due to the conductivity will be discussed in Chapter 6. Both the lower resistivity substrate SRR array and chromium SRR array spectra are shown in Figure 5.22.

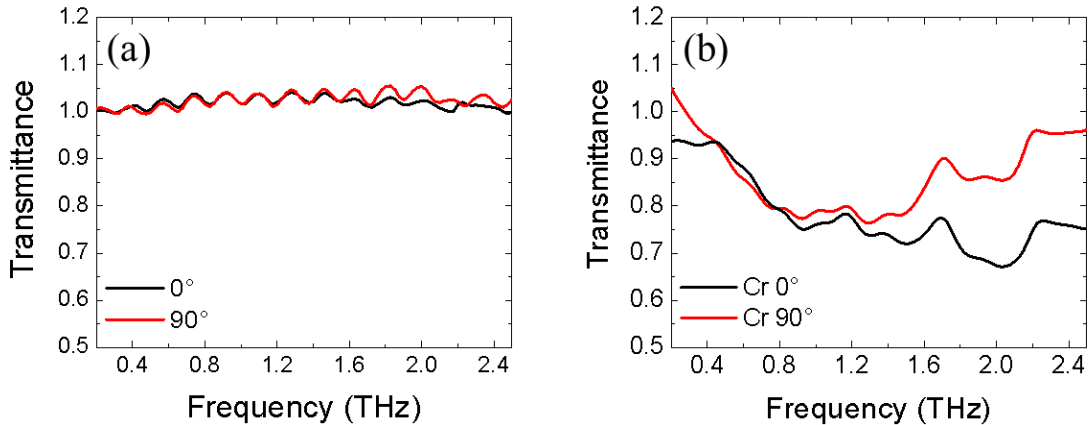


Figure 5.22. Transmittance of single layer arrays fabricated (a) on low resistivity silicon substrate and (b) with rings entirely of chromium.

## 5.6. Conclusion

This chapter has presented the investigation of single layer, passivated, and dual layer SRR array that were fabricated by a standard photolithography lift-off procedure and measured with transmission mode THz-TDS. The SRR arrays were shown to have two distinct and switchable LC resonances as well as a dipole resonance. The addition of the passivation layer served to cause a shift in resonance to lower frequencies.

## CHAPTER 6

### PERFECT ABSORBERS

#### 6.1. Perfect Absorber Background

One type of metamaterial that has shown great potential for active devices is metamaterial perfect absorbers. The unique properties of metamaterial perfect absorbers make them an ideal candidate for metamaterial functioning devices designed for sensing and detection. Absorbers are also proposed to be useful in applications designed to minimize interference. Although not a metamaterial, the first absorber device—the Salisbury screen—was invented in 1952 and designed to absorb at microwave frequencies<sup>154</sup>. It was constructed by a three layer approach consisting of a conducting back plane and a layer of metallic resonators separated with a dielectric spacing layer. Through impedance matching the device to the surround atmosphere, the Salisbury screen would minimize reflection by creating a destructive interference between the wave reflected from the back plane and that reflected from the resistive layer.

The first metamaterial perfect absorber, reported in 2008, and had a similar structure and functionality.<sup>155</sup> The device took advantage of the inherent loss due to the metal in the FSS layer. The absorber was fabricated using the three layer approach with the resistive layer being replaced with a frequency selective surface (FSS) and metal wire strips were used instead of a full back plane. By appropriately tuning both the FSS elements and the wire strips, they were able to obtain impedance matching between the device and free space (air) leading to a minimized reflectivity. The unit cell structure for the first absorber device is given in Figure 6.1.

The FSS was made up of an array of electric-LC resonators (ELC). An ELC is a type of SRR with a different geometry than a single ring or concentric rings.<sup>156</sup>

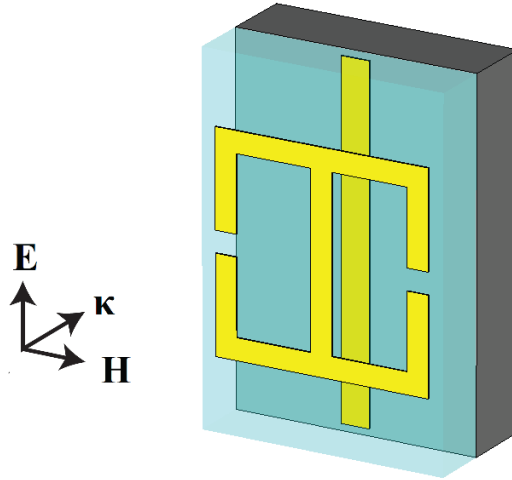


Figure 6.1. Diagram of the unit cell structure of the first metamaterial absorber with associated incident wave field vectors<sup>155</sup>.

The LC resonant frequency for the device was targeted by appropriate selection of the ELC size and geometry. Like the SRR, when the polarization of the incident wave spans the ring gaps of the ELC, an induced current circulates on the rings resulting in an LC resonance. The device also had a polarization dependence similar to the SRR. This first absorber device was reported to exhibit an absorbance of 70% at 1.3 THz. Since then, additional FSS elements have been designed that utilized different geometries including rods<sup>157</sup>, rings<sup>158</sup>, and crosses.<sup>159</sup> Absorbers have also been designed using inverted patterns where the FSS plane is metal and the elements are voids in the plane.<sup>160,161</sup> Near perfect absorption has now become common place.

There has been a great deal of debate on the exact mechanism responsible for the function of metamaterial absorbers. It has been reported that the absorption was due to the destructive interference between the waves reflected from the FSS and backplane.<sup>162</sup> Another report has suggested that the absorption was due to standing wave resonances in the dielectric

spacing layer.<sup>163</sup> Another proposed mechanism of absorption was that out of phase induced currents were the cause.<sup>164</sup> The final candidate mechanism was that the absorption was caused by anti-parallel currents in the FSS and back plane.<sup>155</sup> Regardless of the mechanism of absorption, it is generally agreed upon that the FSS is used to set the resonant absorption frequency and the dielectric spacing layer thickness is used to tune the absorption strength.

In the years since the first metamaterial absorber was reported, there have been great strides in the ability to manipulate the absorption of these devices, including metamaterial absorbers that have been designed to exhibit multiple resonant absorption frequencies.<sup>158,161,165,166,167,168,169</sup> These absorbers are capable of developing more than one resonant frequency due to the imposing of unique geometries which include more than one ring incorporated into the unit cell structure whether connected laterally or as concentric rings as shown in Figure 6.2.

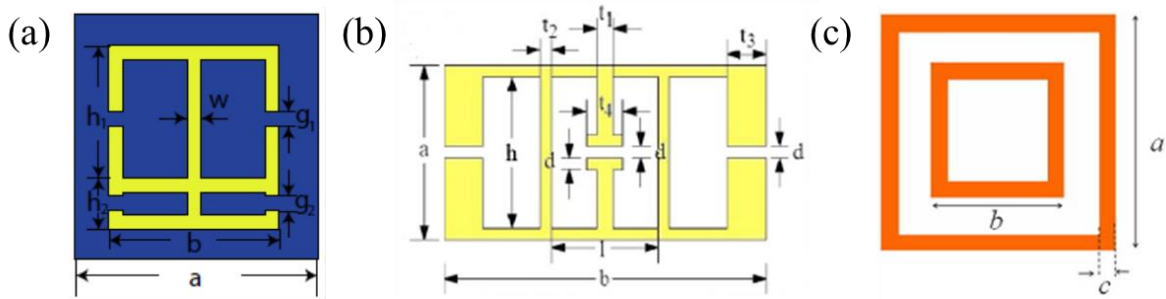


Figure 6.2. Dual band metamaterial absorber designs based on references (a) 162, (b) 163, and (c) 158.

Due to the resonant nature of the elements that make up the FSS in most absorber devices, the effective absorption frequency range is typically very narrow. There has been much work towards achieving broadband absorber devices. A great deal of this work has been focused on the incorporation of multiple ELCs with different, but very close resonant frequencies into the

FSS unit cell.<sup>159,168,169,170,171,172</sup> By doing so, the overlap in the individual absorption from each ELC can form a wider band of absorption. The extraction of individual frequencies from the total absorbed radiation may be possible with these types of absorbers which could lead to broader detection applications.

In 2009, the same group that produced the first metamaterial absorber reported a new absorber designed to be insensitive to the polarization of the incident radiation.<sup>173</sup> The device again consisted of three layers including a bottom layer of crosses instead of wire strips, a middle dielectric spacing layer, and a top layer of ELCs. This time, however, the ELCs were designed to exhibit four-fold rotational symmetry which allowed polarization insensitivity, as shown in Figure 6.3. The device was reported to achieve an absorbance of 75% at 1.15 THz for both the polarization shown in Figure 6.3 (c) and when the polarization was rotated 90°. Since then, a variety of additional polarization insensitive designs have been reported.<sup>158,159,167,174,175,176,177</sup> Two recent reviews of metamaterial absorbers have been published and offer more detail on the subject.<sup>178,179</sup>

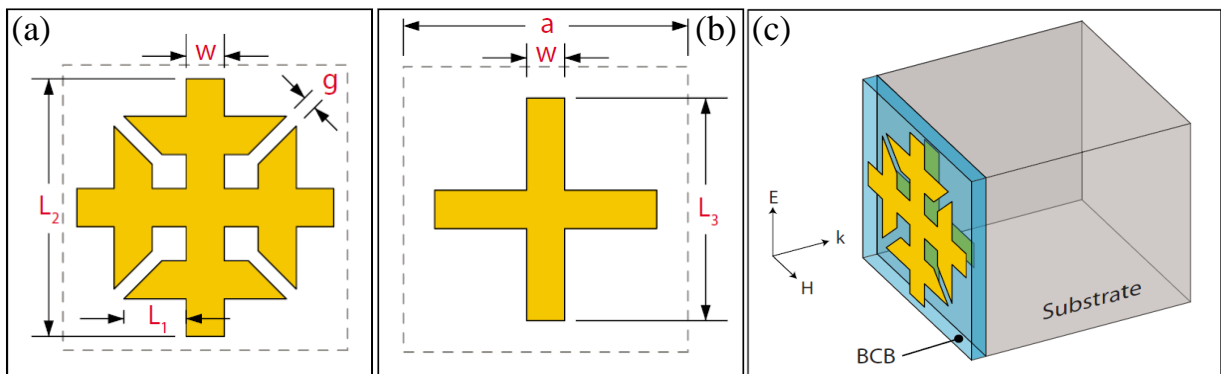
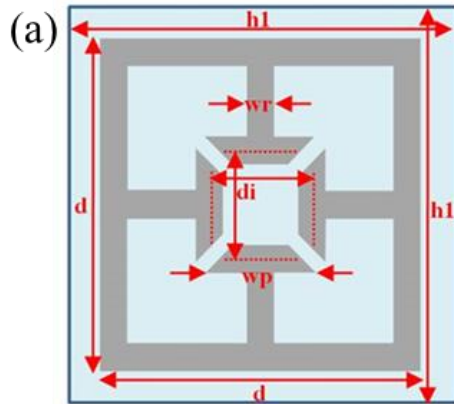
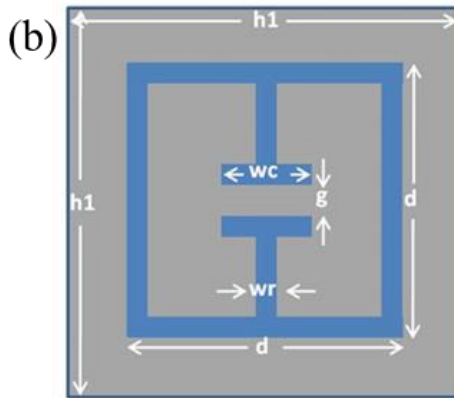


Figure 6.3. Diagram of the unit cell structure of the first polarization insensitive metamaterial absorber including the (a) FSS unit cell ELC structure, (b) ground plane element structure, and (c) three-dimensional view with associated incident wave field vectors<sup>173</sup>.

Although a few devices have been reported to have polarization insensitivity, no explanation of this characteristic has been reported and only a single report of the verification of this property by measurement at polarizations other than  $0^\circ$  and  $90^\circ$  was found.<sup>158</sup> This chapter details the investigation of a polarization insensitive metamaterial absorber. The perfect absorber structures in this work were designed based on the common three layer approach using a conducting back plane base followed by a dielectric spacing layer with a frequency selective surface layer of periodic metallic resonant elements on top. The resonant frequencies of the top layer correspond to the frequencies where the device absorbs. In these structures, the geometry of the top layer allows for accurate targeting of the resonant frequency while the dielectric spacing layer thickness determines the strength of the resonance. The absorbers were also fabricated by standard photolithography and electron beam evaporation for metal deposition. The fabricated structures were characterized by THz time domain spectroscopy. Figure 6.4(a) gives the unit cell dimensions along with corresponding values for each dimension for what we refer to as 4-T absorbers due to the fact that the structure appears to contain four internal, T-shaped arms. Figure 6.4(b) gives the same as (a), but for what we refer to as 2-T absorbers which only have two internal, T-shaped arms. The naming convention for each array was based its position on the mask such that R4C3, for example, would be the array in the fourth row and third column.



	d (um)	di (um)	wr (um)	wp (um)	h1 (um)	b (um)	sep (um)	spacing
2A (R3C1)	56	20	4	21	75	0.4	9	19
2B (R3C2)	1010	26	1010	21	1010	1010	1010	
2C (R3C3)	1010	20	1010	15	1010	1010	1010	
2D (R3C4)	1010	20	1010	4	1010	1010	1010	
2E (R4C1)	50	18	3.5	19	67	0.4	7.8	17
2F (R4C2)	1010	24	1010	19	1010	1010	1010	
2G (R4C3)	1010	18	1010	13	1010	1010	1010	
2H (R4C4)	1010	18	1010	3.5	1010	1010	1010	
2I (R5C1)	44	15.5	3	16.5	59	0.4	7.4	15
2J (R5C2)	1010	22	1010	16.5	1010	1010	1010	
2K (R5C3)	1010	15.5	1010	10	1010	1010	1010	
2L (R5C4)	1010	15.5	1010	3	1010	1010	1010	



	d (um)	wr (um)	wc (um)	g (um)	h1 (um)	b (um)	sep (um)	spacing
1A (R1C1)	35	3.5	15	2.5	47	0.2	8.7	12
1B (R1C2)	1010	1010	15	5	1010	1010	1010	
1C (R1C3)	1010	1010	11	2.5	1010	1010	1010	
1D (R1C4)	1010	1010	6.5	4	1010	1010	1010	
1E (R2C1)	30	3	13	2	40	0.2	7.4	10
1F (R2C2)	1010	1010	13	4	1010	1010	1010	
1G (R2C3)	1010	1010	11	2	1010	1010	1010	
1H (R2C4)	1010	1010	6	3	1010	1010	1010	
1I (R1C5)	25	2.5	11	1.5	33.5	0.2	6.3	8.5
1J (R2C5)	1010	1010	11	4	1010	1010	1010	
1K (R3C5)	1010	1010	8	1.5	1010	1010	1010	
1L (R4C5)	1010	1010	5.5	3	1010	1010	1010	

Figure 6.4. Unit cells with labeled dimensional parameters and mask dimensions for both (a) 4-T and (b) 2-T absorbers.

These types of structures (3-D planar absorbers) are being intensely researched by multiple groups around the world due to the fact that their electromagnetic response can be easily engineered along with simple, inexpensive fabrication possibilities. It has already been shown that these types of structures can achieve near perfect absorption, but as more unique EM responses are sought, the design geometries can become increasingly complex leading to difficulty in the identification of the exact mechanisms of interaction.

## 6.2. Simulation of Perfect Absorbers

The metamaterial absorbers presented in this work were also designed by simulation with COMSOL Multiphysics. Like the SRR simulations, the built-in wave equation of RF Module was used. After the model geometries and material parameters had been set, the boundary conditions were selected. This time, however, the boundary conditions were changed from PBCs to perfect electric conductor and perfect magnetic conductor conditions (PEC and PMC) that are set up with the equations:

$$\mathbf{n} \times \mathbf{E} = 0 \quad (6.1)$$

and where  $\mathbf{n}$  is the normal vector to the plane of the FSS element and:

$$\mathbf{n} \times \mathbf{H} = 0 \quad (6.2)$$

This set of boundary conditions is well suited to models that have good mirror symmetry. The built model unit cell system along with the established boundary conditions is given in Figure 6.5. The built model with added mesh is given in Figure 6.6.

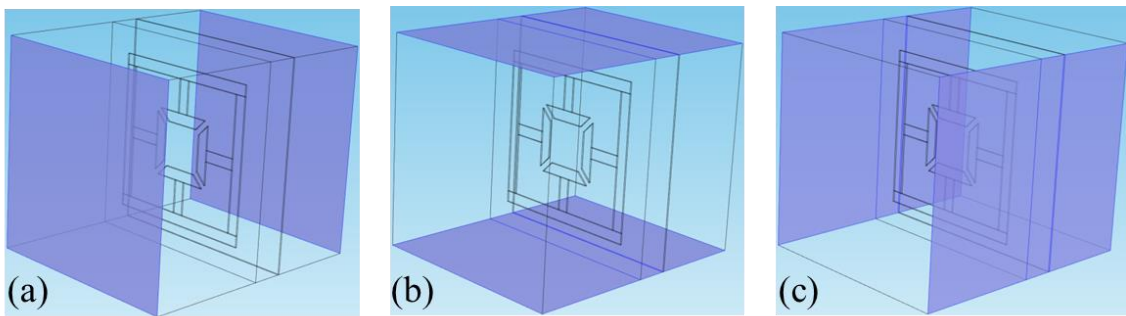


Figure 6.5. Absorber unit cell model with (a) front radiative source and back scattering boundary conditions as well as (b) perfect magnetic conductor and (c) perfect electric conductor boundary conditions.

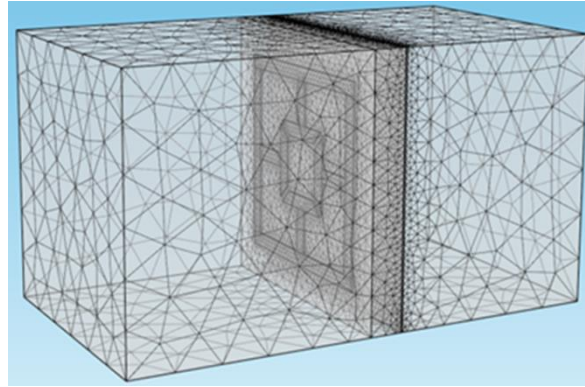


Figure 6.6. 4-T absorber simulation model with mesh added.

Once the model had been fully defined, the simulation was performed. Figure 6.7 shows post-processed slices of the electric and magnetic field vectors both below and at the resonant frequency. It is plain to see that at the resonant frequency, the device shows strong absorption of the wave. This type of processed view is perhaps the quickest, easiest way to see that the device is in operation.

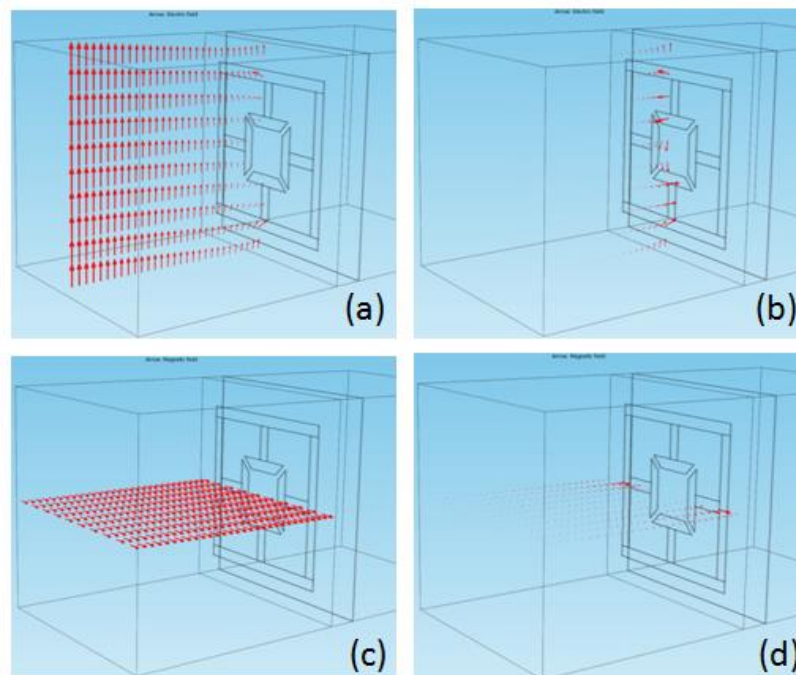


Figure 6.7. Simulated reflected (a &b) electric and (c & d) magnetic field vectors for the absorber device below (a & c) and at (b & d) the resonant frequency of 0.89 THz.

The simulated surface current density on the resonant element at  $0^\circ$  and  $45^\circ$  rotations is seen in Figure 6.8. In this Figure, red colored arrows have been added for clarity on the direction of the current as well as blue and black arrows indicating the capacitive regions in which the electric field is strongest. The currents in the  $0^\circ$  rotation oscillate about approximately half of the ring resulting in two effective LC resonating half rings. However, by tracing the currents in the  $45^\circ$  rotation, we can see that the current paths have changed. At this rotation, the current paths form four quarter rings where the current in the left and right quarter rings oscillate like dipoles and the top and bottom quarter rings exhibit LC oscillation.

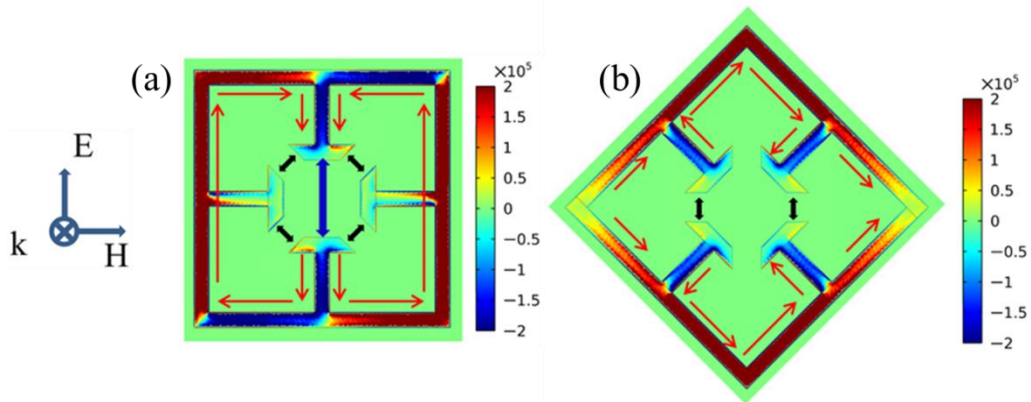


Figure 6.8. Simulated surface current density of the absorber unit cell at resonance.

Multiple simulations were performed in order to estimate the effect of varying specific size dimensions of the resonant element unit cell. In Figure 6.9 presents the simulated effect that manipulating the outer length,  $d$ , of the resonant element has on the resonant frequency. According to the simulations, the resonant frequency can be scaled higher or lower by decreasing or increasing, respectively, this size dimension.

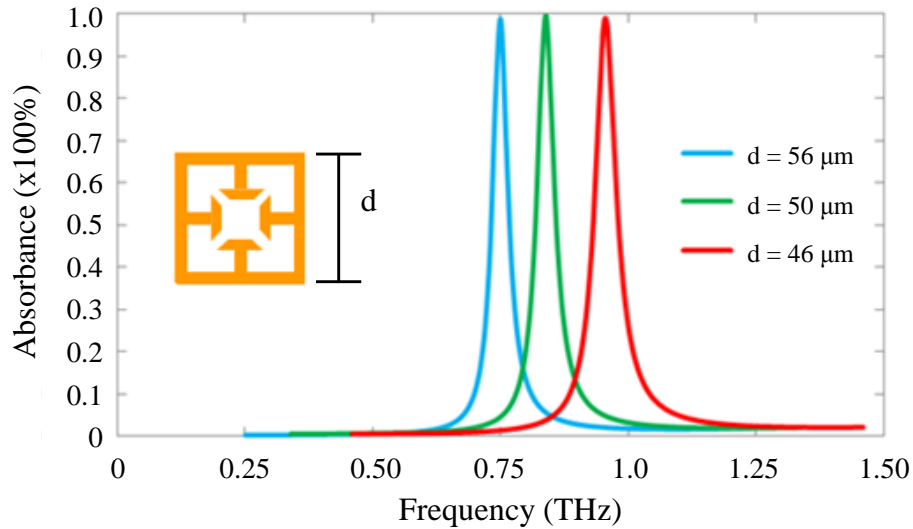


Figure 6.9. Simulated absorbance for elements with varied outer length.

The absorption strength in Figure 6.9 does not appear to change with the variation of the outer length. This is due to the fact that each of the simulations had a different dielectric thickness. As seen in Figure 6.10, the strength of absorbance is strongly dependent on the dielectric thickness. Therefore, any changes in the planar geometry of an FSS element that cause a change in the resonant frequency must be accounted for by tuning the dielectric thickness. This was done by simply repeating the simulation while sweeping through a range of thicknesses.

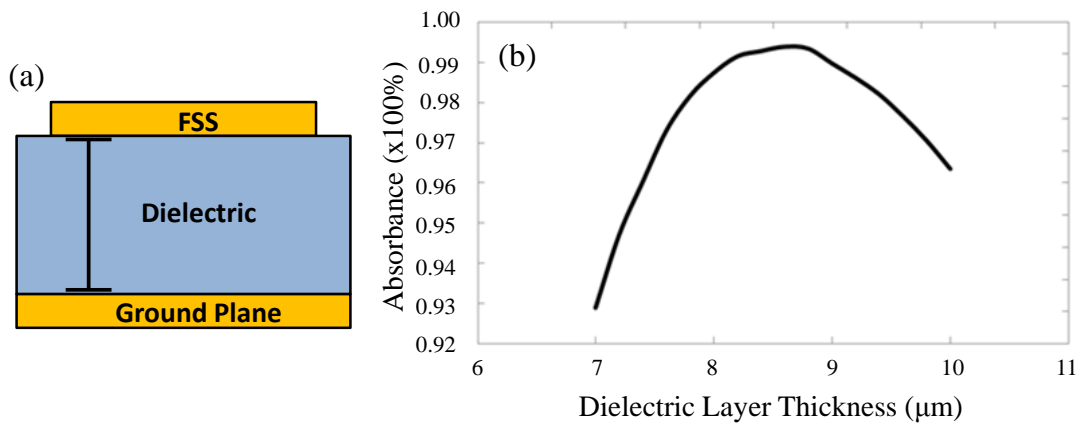


Figure 6.10. (a) Diagram of side view of absorber unit cell with (b) the absorption as a function of the dielectric layer thickness.

Based on the simulation results, the photomask used for the fabrication of these absorber devices was drafted. The mask was again designed to be a dark-field mask that would be more suitable to the lift-off process. The mask layout is shown in Figure 6.11.

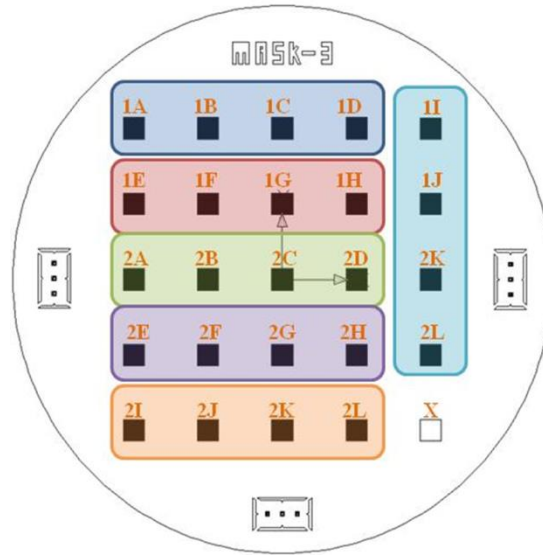


Figure 6.11. Diagram of the layout of the photomask used for fabrication of the absorbers. The dark squares indicate arrays of FSS elements with varied dimensional parameters.

### 6.3. Perfect Absorber Fabrication

The process of developing a fabrication procedure for the absorber arrays required the optimization of the processing of the polyimide to achieve accurate and repeatable dielectric spacing layer thickness. It started with the spin coating and curing the polyimide (PI-2610) layer. The PI-2610 was to be static drip coated followed by the immediate two stage spinning cycle of a 400 rpm spread stage for 5 s and higher speed spin stage for 30 s, with this second stage speed set according to the desired PI-2610 thickness. This was to be followed by a two stage hot plate baking cycle of 85°C for 90 s and 135°C for 90 s. After this, the substrate was to

be cured under inert atmosphere at 350°C for 30 min. In the first tests, the spin speed stage was set to 2000 rpm which lead to an after-cure thickness of about 3 μm when measured by profilometer directly after the curing bake. This did not match the spin speed curve provided by the manufacturer, but during this time the goal was to verify that the process would be successful. At this point, the PI-2610 was applied to several small pieces of bare Si substrate to generate rough spin-speed curves, which were then used to determine the spin speeds and number of layers needed to achieve the correct thicknesses.

Once the correct spin speeds were determined for the desired polyimide thickness and used to get the copper ground plane and dielectric spacing layer stably in place, the standard photolithography processing was applied. A ground plane consisting of 15 nm chromium and 200 nm copper was deposited onto a 2" diameter, 250 μm thick Si wafer followed by the polyimide deposition procedure. The VM-651 adhesion promoter steps were repeated to make ready the top surface of the polyimide before drip coating the S1808 immediately followed by a two stage spin cycle of 300 rpm spread stage for 3 s and 3000 rpm spin stage for 30 s to get a photoresist thickness of about 800 nm and a hot plate bake at 115°C for 1 min. The photoresist was next exposed in the Karl Suss MA-6 Mask Aligner and then developed in MF-319 developer for 30 s followed by a 90 s deionized water bath. According to manufacturer specifications, the exposure time should have been 3 s, but this time gave poor results under the optical microscope. After optimizing the exposure time by successive trials, the optimum time was found to be 1.8 s although the inner 45° angles appeared slightly rounded regardless what time was used as seen in Figure 6.12. More on this issue will be discussed in Chapter 7.

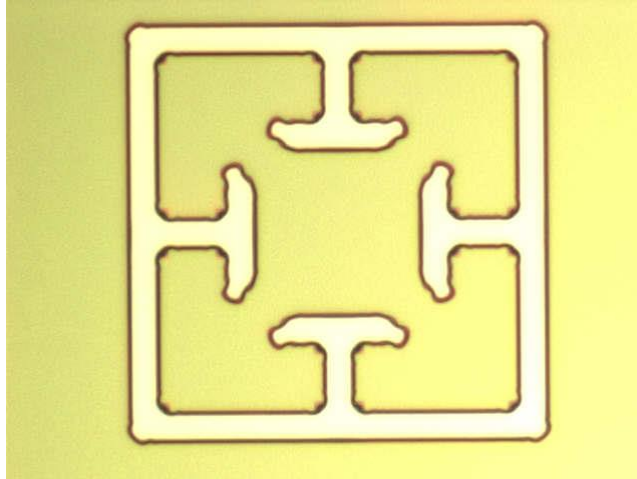


Figure 6.12. Optical microscope picture of a FSS resonant element pattern in photoresist after development.

At this point, E-beam metal deposition was performed in two stages consisting of a 15 nm chromium adhesion layer and a 185 nm layer of copper, which was then followed by attempted lift-off. The first lift-off attempt was performed in an acetone bath for 20 min, but no lift-off was seen. This was followed by placing the acetone into a sonic bath which did initiate lift-off, but did not prove to be a repeatable process as some times all of the metal would lift-off. To solve this problem, an additional step of E-beam deposition of 15 nm of  $\text{SiO}_2$  was added after the VM-651 adhesion assist coat. The addition of the  $\text{SiO}_2$  layer did greatly improve the adhesion of the metal patterns to the polyimide. Unfortunately, the addition of the  $\text{SiO}_2$  required the optimization of the S-1808 exposure time to be repeated. The new optimized exposure time was found to be 2.1 s, although the structures still appeared to be rounded at the  $45^\circ$  angles. This is seen in Figure 6.13. It was unclear at the time how the additional material layer would affect the operation of the absorbers, but the effort was still focused on achieving successful fabrication of the devices. It was later determined that the  $\text{SiO}_2$  layer had negligible effects on the device performance.

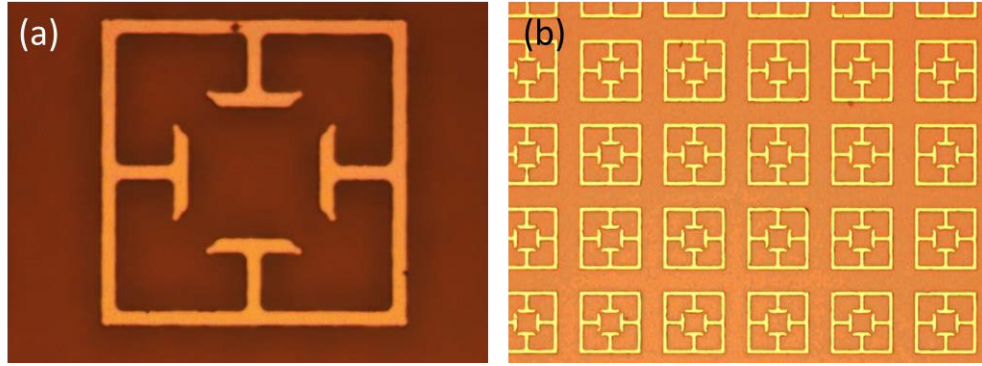


Figure 6.13. Optical microscope pictures of (a) an absorber FSS element fabricated without the additional  $\text{SiO}_2$  layer and (b) with the  $\text{SiO}_2$  layer. The picture in (b) was taken before lift-off.

The absorbance of these first sets of fabricated absorbers was measured with the THz TDS system in reflection mode and seen to obtain a maximum absorbance of approximately 30% among the best performing arrays. Upon repeating the polyimide thickness measurement with the profilometer, the thicknesses were all seen to have decreased dramatically. It was believed that the polyimide hot plate baking steps were not of a sufficiently high temperature to prevent surface chemistry interaction between individual layers. This meant that each time a new layer was applied, the previous layer was still fluid enough that some of it would combine with the new polyimide and be spun off during the high speed spinning. This was corrected by increasing the PI-2610 hot plate bake temperatures from  $85^\circ\text{C}$  and  $135^\circ\text{C}$  to  $105^\circ\text{C}$  and  $150^\circ\text{C}$ , respectively, as well as adding a  $185^\circ\text{C}$  oven bake for 5 min, which led to a nearly linear increase in thickness per layer. It did, however, require the running of a new series of spin-speed curves to determine the proper thicknesses. During the spin-speed curve testing, several of the finished polyimide coats were used to continue photolithography and lift-off testing. One of these test pieces in particular was measured to have a  $20\ \mu\text{m}$  polyimide layer, but only three of the arrays survived the lift-off process. These three arrays have shown the strongest absorption to date and since have had the polyimide thickness measurement repeated to find an actual thickness of  $10.7\ \mu\text{m}$ . The results of these arrays will be further discussed later in this chapter.

Fabrication was attempted again with the newly optimized PI-2610 baking procedure, and again the absorbance was observed to be weak. The polyimide thicknesses were again measured by profilometer, and again seen to be less than expected. This was thought to be due to insufficient curing bake temperature. For the next fabrication attempts, the substrates were cleaved into smaller pieces after the SiO<sub>2</sub> deposition and cured at 350°C for 50 min with a 2°/min ramp rate in a nitrogen purged tube furnace. Since this process has been in place, the PI-2610 thicknesses have appeared to be finally stable. In addition, the photolithography procedure was reoptimized for this set of devices. It was suspected that the photoresist side walls were too far from vertical, which was causing the difficulty in lift-off. To remedy the situation, a new lift-off photoresist (MicroChem LOR-3B) layer was added before the S1808 that would undercut it.

After running yet another set of spin-speed curves, shown in Figure 6.14, to optimize the new curing bake and dual photoresist processes, fabrication was attempted again. This time the polyimide average thicknesses were measured to be 5.8 μm and 7.1 μm by profilometer which was exactly what was expected, and according to simulation should yield better than 90% absorbance. However, the absorbance of these new sets of absorber arrays were has been seen to be only 40% for the strongest absorbing arrays.

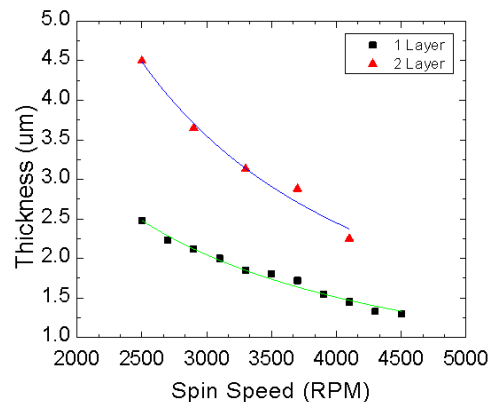


Figure 6.14. Experimentally produced spin-speed curves for PI-2610.

#### 6.4. Perfect Absorber Measurement Procedure

The Z-2 reflection mode setup was used to measure the THz time domain reflection of the metamaterial absorber arrays. The absorber arrays were mounted on the same steel plate holder with a small aperture that was used to position the arrays correctly in the terahertz pulse path with the motion controlled stage. Both the polarization dependent and the polarization insensitive absorbers were rotated about the terahertz pulse path to measure the sensitivity of the arrays to the incident polarization as shown in Figure 6.15. Although Figure 6.15 only shows the  $0^\circ$  and  $45^\circ$  rotations, the arrays were measured at multiple angles from  $0^\circ$  up to and full  $90^\circ$  rotation in  $10^\circ$  increments.

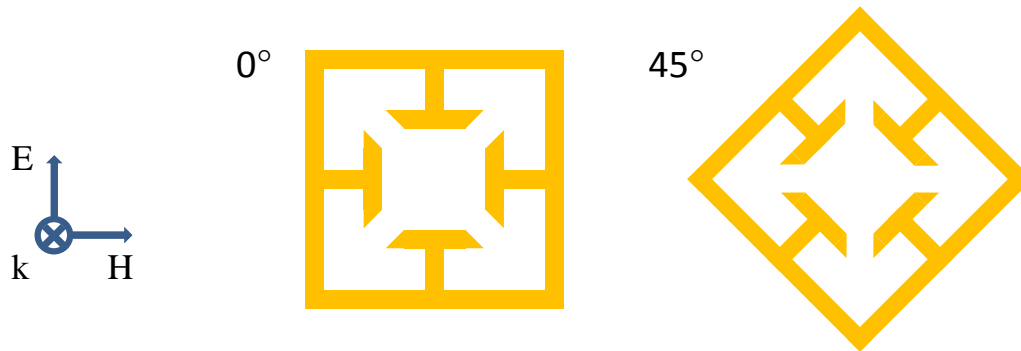


Figure 6.15. Diagram of the absorber FSS unit cell structure showing the change in orientation during rotation with respect to the incident wave vector.

The purpose of the conducting ground plane was to eliminate transmission. This was observed to be the case in the simulations. Before the reflection mode measurements were performed, the arrays were measured with the transmission mode setup and verified to have no transmission which allowed for a simplification in data processing. The measurements were processed in the same manner as the SRR measurements with the additional step of calculating the absorbance spectra by the formula:

$$A = 1 - R \quad (6.3)$$

where  $A$  is the absorbance and  $R$  is the reflectivity.

### 6.5. Perfect Absorber Results

The first characterization performed after fabrication is always optical microscope inspection to determine the status of the absorber structures through the lift-off process. Figure 6.16 shows three optical microscope pictures, each taken through a 50x objective, of the corresponding array from the 5.8  $\mu\text{m}$ , 7.1  $\mu\text{m}$ , and 10.7  $\mu\text{m}$  polyimide thickness arrays. Overlaid onto each picture is an outline corresponding to the correct dimensions from the photomask. The structures with 10.7  $\mu\text{m}$  polyimide thickness more closely match the outline than those from the other two. The width of the metallic legs should be 3.5  $\mu\text{m}$ , but have been measured to be 2.6  $\mu\text{m}$ , 2.2  $\mu\text{m}$ , and 3  $\mu\text{m}$  for the 5.8  $\mu\text{m}$ , 7.1  $\mu\text{m}$ , and 10.7  $\mu\text{m}$  polyimide thickness arrays, respectively. It also appears that the inner 45° features on the 10.7  $\mu\text{m}$  polyimide thickness array are more correctly shaped. Figure 6.16(d) shows the measured absorption spectra for each of the arrays. There is a slight, but noticeable frequency shift seen between the absorption peak from the array on 10.7  $\mu\text{m}$  thick polyimide and the other two arrays. This is most likely due to the differences in the widths of the metallic legs mentioned previously. The obvious difference however, is in terms of the absorption magnitude. The 7.1  $\mu\text{m}$  thick polyimide thickness should be, according to simulation, the optimized array and therefore, should exhibit the strongest absorption.

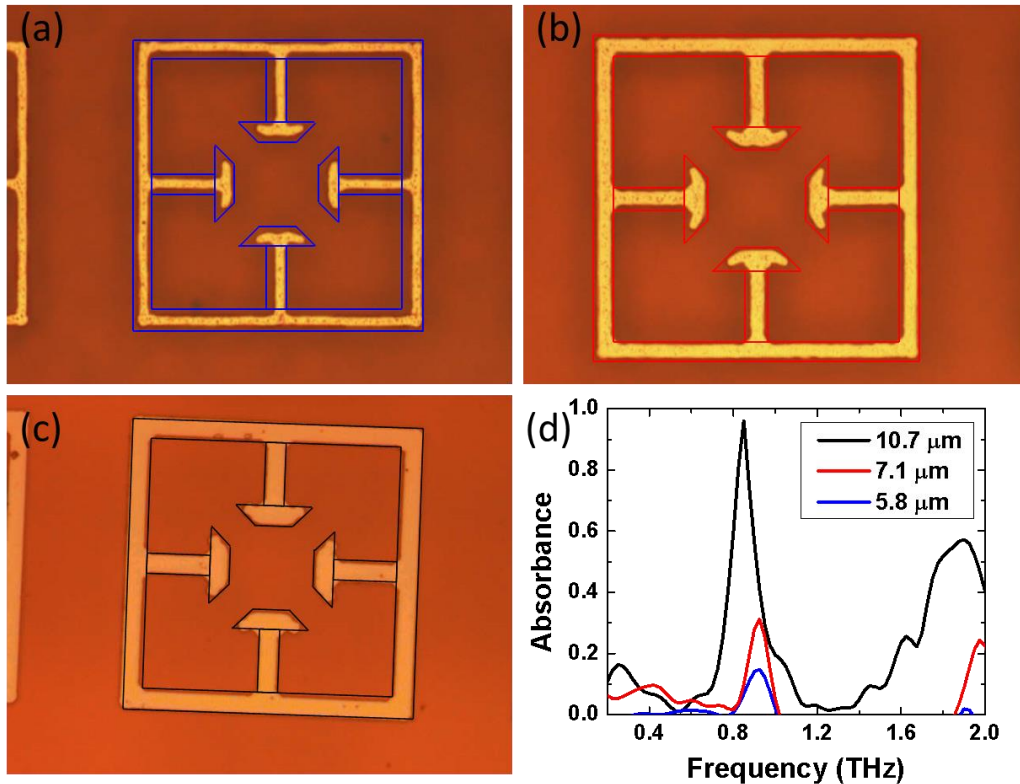


Figure 6.16. Optical microscope pictures of an individual FSS element in absorber arrays with (a) 5.8  $\mu\text{m}$ , (b) 7.1  $\mu\text{m}$ , and (c) 10.7  $\mu\text{m}$  polyimide thickness and (d) the corresponding absorption spectra. Outlines corresponding to listed mask dimensions have been added to optical microscope pictures.

Another discrepancy from expected absorption from simulation is the broadened absorption. The cause for this was found to be the difference in conductivity of the copper making up the structures from that of bulk copper ( $6 \times 10^7$  S/m). In fact, simulations based on lower copper conductivity ( $1 \times 10^7$  S/m) match well with the measurement as shown in Figure 6.17 (a). Figure 6.17 (b) shows simulations of different copper conductivities and clearly indicates that as the conductivity is reduced, the absorption is red shifted and broadened.

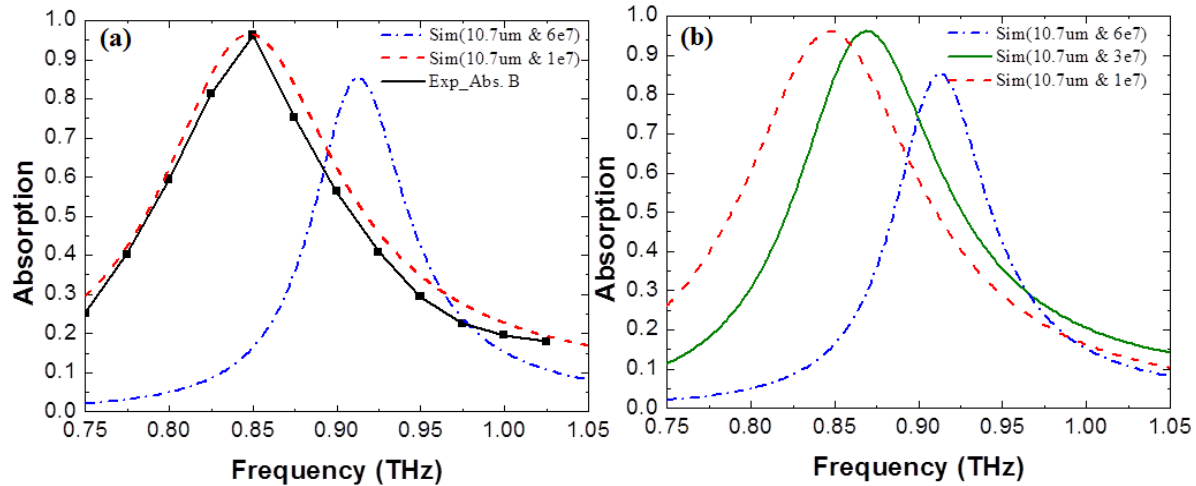


Figure 6.17. (a) Simulated absorption spectra of absorber structures with bulk and matched conductivity with the measured absorption and (b) Simulated absorption spectra of The absorber structures with varied conductivity.

The course of study has focused on those arrays that have yielded the best results in the absorbance spectrum with the 10.7  $\mu\text{m}$  polyimide thickness array, as shown in Figure 6.17(a). Even though, only three arrays for that polyimide thickness survived during the lift-off process, all three arrays have shown strong absorption. It was previously stated that the structures were designed to allow observation of the effects of varying specified dimensions. Figure 6.18(a) shows the absorbance spectra of these three arrays with 10.7  $\mu\text{m}$  polyimide thickness. The variation in the dimensions of the unit cell structures (see Figure 6.4) lead to a slight change in resonance frequency from array R4C3 and R4C2, whereas a more noticeable frequency shift occurs from R4C3 to R5C3. This demonstrates the dependency of the resonant frequency on certain dimensions more than others. In particular, the most important dimensions on the absorption frequency are the length of the outside metal square and the closest distance between both adjacent T-shaped structures (typically lead to LC resonances) and opposite inside T-shaped structures (typically lead to dipole resonances). Also, Figure 6.18(b) shows the results of the absorbance spectra collected at various rotation angles from the array R4C3 about the THz

propagation vector. As shown in the Figure 6.18(b), the resonance frequency is consistent through the rotations. This demonstrates the polarization insensitivity of the structure.

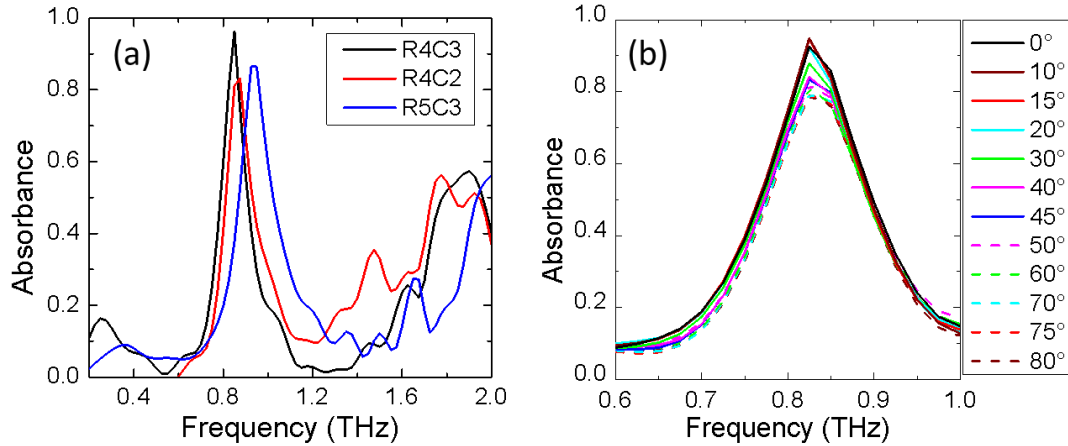


Figure 6.18. Measured absorbance of (a) arrays with varied size parameters and (b) array R4C3 at rotations about the wave vector to show insensitivity to polarization.

At first glance, the differences in absorbance strength over the rotations might be thought to have some angular dependence, and while this is slightly true, the cause of the difference in this case was due to the measurement. We speculate that the center of the array might not be perfectly centered on the rotation stage. Therefore, the effective area of the array onto which the THz beam was incident was changing throughout the rotation, and resulted in that each spectrum was measuring a slightly different area of the array. Thus, the differences in absorption magnitude are more likely due to inhomogeneity of the individual absorber elements inside of the arrays since the fabrication process could not be perfect. This is proven by the fact that the rotation angles from 45° to 90° do not mirror those from 45° to 0°, as the symmetry of the structures ideally require.

Significant variation in the time domain reflected pulse was also observed between different arrays as is seen in Figure 6.19. Interestingly, very little difference was observed in the

actual pulse peak amplitude, but the ringing that occurs after the pulse is affected. This was not expected, but can be rather useful during measurement. It was often difficult to determine the optimal placement of the array in the THz beam path when the pulse peak position is used as a polling position, which has been done routinely for other measurement. This results in the necessity to perform an entire spectroscopic scan every time a movement is made. By polling a position in the ringing signal it is possible to find the optimum measurement location much more quickly.

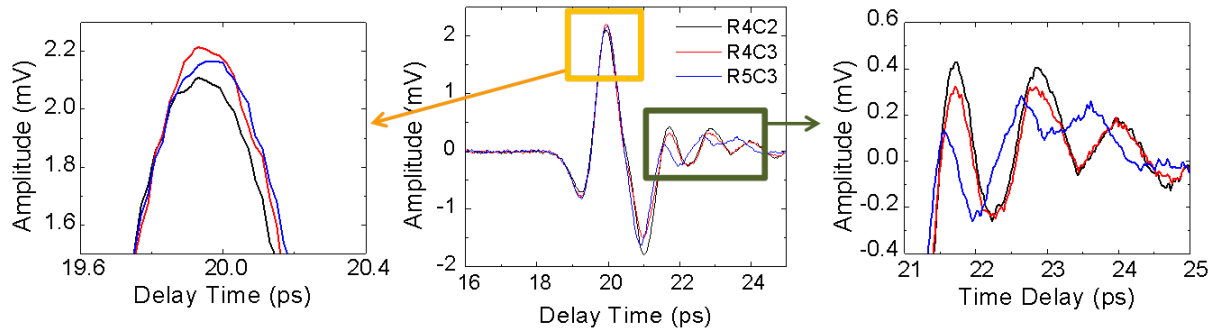


Figure 6.19. Measured time domain amplitude with zoomed view of peak and ringing.

Figure 6.20 shows the results of the electric field and surface current distributions in the FSS elements obtained from simulation which showed how to explain the polarization insensitivity of the design that occurs in our designed structure. The relation between the simulated electric field and current density distributions at the FSS for incident polarizations of (a)  $0^\circ$ , (d)  $20^\circ$ , and (g)  $45^\circ$  and corresponding back plane electric field and current density distributions (c, f, and i) in Figure 6.20 were used to evaluate the effective poles and formulate the circuit models (b, e, and h) for the incident polarizations.

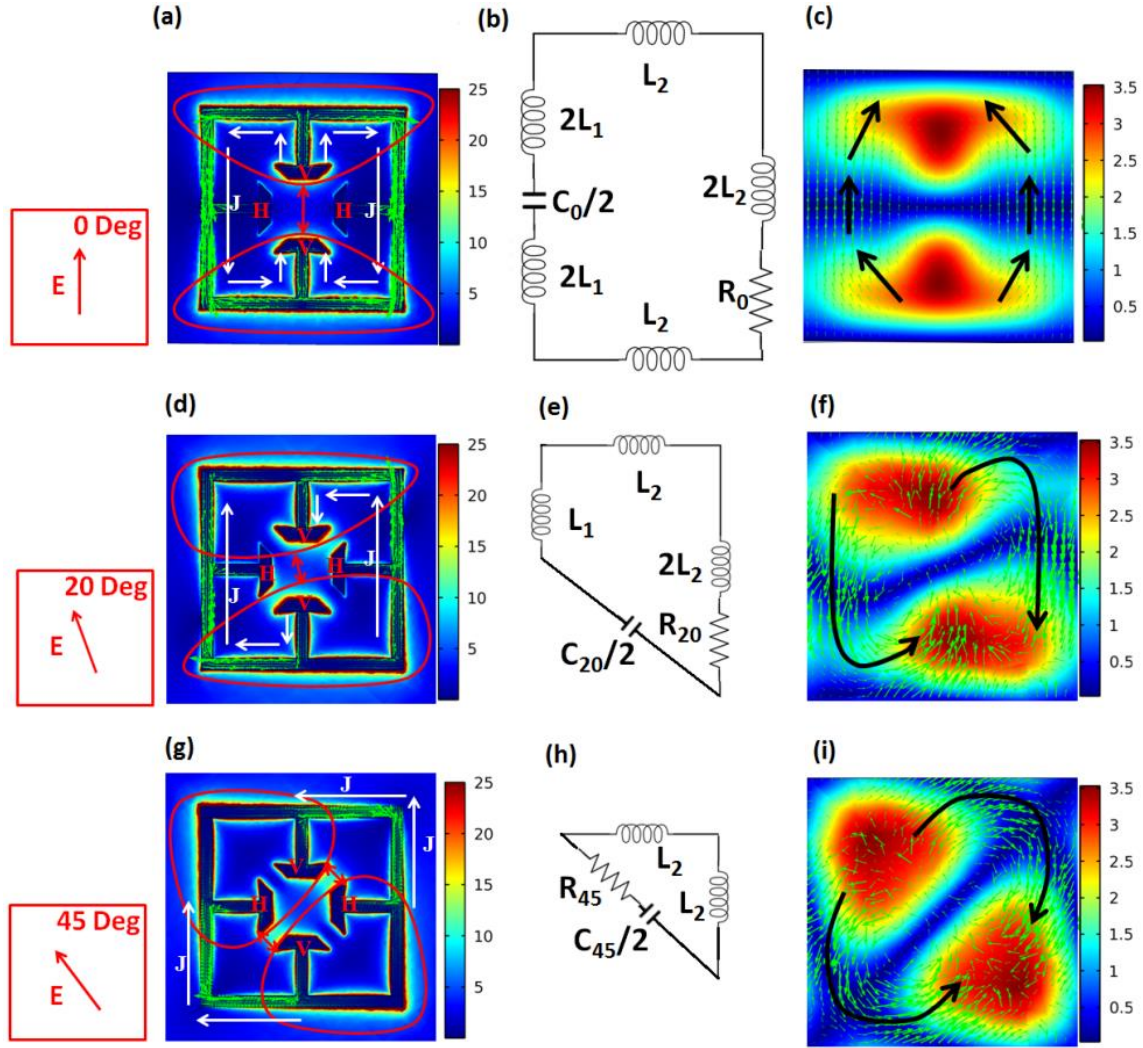


Figure 6.20. (a, d & g) Electric field and current density distribution on FSS where white arrows show the current direction, red closed curves show the locations of effective poles and the labels V and H indicate to horizontal and vertical legs. (b, e & h) FSS circuit model and (c, f & i) electric field and current density on back plane. Black arrows indicate current paths for clarity.

The circuit models can be used to reliably predict the resonant frequency at the varied polarizations and describe why the resonant frequency, given by  $f = 1/\sqrt{LC}$ , is insensitive to the incident polarization. At  $0^\circ$ , the capacitance is set by the distance between opposite “T”s while the inductance is set by the current path along the outer edge of the square ring. As the polarization is rotated, the capacitance distance decreases unit reaching a minimum at  $45^\circ$  where it is determined by the distance across the small  $45^\circ$  gaps leading to a maximum capacitance.

However, the increase in capacitance is accompanied by a decrease in inductance due to the reduction in current path length along the outer edge of the square ring. As a result, the effective LC product is maintained constant allowing for a truly polarization insensitive unit cell.

Figure 6.21 (a) indicates the calculated impedance from the simulated data. This impedance matched the measured absorbance at  $0^\circ$  polarization. The relative impedance at resonance was  $0.73-j0.37 \Omega$ . This was reasonable when the absorbance was 96.5%. Figure 6.21 gives the impedance calculated from simulation for array R4C3 with bulk copper conductivity of  $6 \times 10^7$  S/m, polyimide permittivity of 3.15 and polyimide thickness of  $7.5 \mu\text{m}$  which gave rise to near perfect absorption at 0.9 THz. The calculated impedance at 0.9 THz was  $0.98+j0.03 \Omega$  where the absorbance was 99.95%.

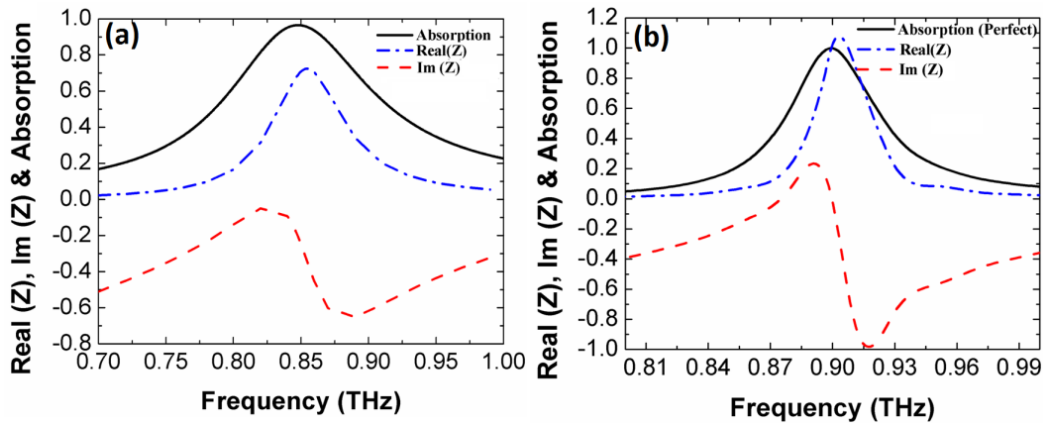


Figure 6.21. (a) Absorption (black solid), real part (blue dashed-dot) and imaginary part (red dashed) of calculated relative impedance for absorber B. (b) Absorption (black solid), real part (blue dashed-dot) and imaginary part (red dashed) of calculated relative impedance for the ideal case of absorber R4C3. For simulation, the copper conductivity was set to  $6 \times 10^7$  (S/m), the polyimide permittivity to 3.15 and the polyimide thickness to  $7.5 \mu\text{m}$ .

As listed in Figure 6.4, we have another structure with two T-shaped arms to study in addition to the 4-T absorbers. The 2-T absorber structure exhibits polarization dependence, as shown in Figure 6.22. This figure shows the absorbance spectra of two arrays with different in-

plane rotation angles. Whereas the 4-T structures exhibit a  $90^\circ$  rotational periodicity, these structures have only  $180^\circ$  rotational periodicity. As these structures are rotated, the origin of the absorption resonance changes from both LC and dipole to solely dipole, leading to a shift in the absorption frequency about the rotation. When observed from a static frequency (either resonance), the rotation appears as a switching effect which could potentially prove useful in future devices.

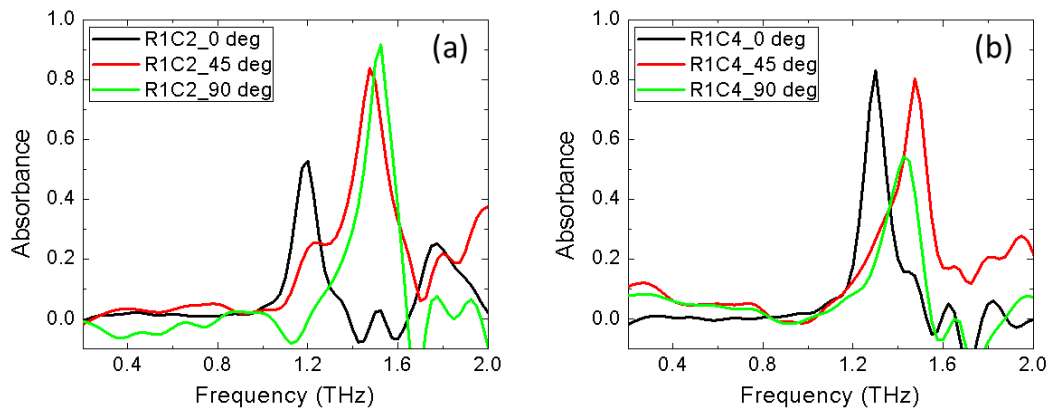


Figure 6.22. Measured absorption spectra of 2-T absorber arrays (a) R1C2 and (b) R1C4 at rotations of  $0^\circ$ ,  $45^\circ$ , and  $90^\circ$ .

Both the 2-T and 4-T structures develop multiple resonances. Their operation can be described in terms of the surface current paths. As the 4-T structures have more available path options, their operation is more difficult to describe. For this work, the focus has been on the first developed resonance of these structures. It must be noted that the optimization of each individual resonant absorption peak requires a unique dielectric spacing thickness, so it is likely impossible to optimize more than a single peak with a single device.

It often can be difficult to accurately place a sample at the focal point of the THz beam not only because the beam is not visible, but also due to the fact that noise in the time domain

signal makes it difficult to discern small increasing or decreasing trends in the pulse amplitude and delay. A simple solution to this problem is imaging. Again, by using the three dimensional motion controlled stage to raster scan a specimen in the THz beam path and taking a spectroscopic scan at set intervals, an image of the specimen can be reconstructed from the spectroscopic data. Another method that simply sets the delay stage at a constant position to detect the THz pulse peak is much faster because it requires no actual scanning time per pixel. This is the fast scanning technique used to find, and subsequently place samples at, the focal point before measurement. This becomes especially important to ensure proper placement of the sample and proper selection of the length and width of the imaging window before full spectroscopic imaging. This is also invaluable for positioning samples such as the previously mentioned SRRs and absorbers, because they cause little variation to the time domain signal.

Spectroscopic imaging can also be useful in evaluating the localized quality of particular sections of either SRRs or absorbers within arrays. Figure 6.23, shows two reconstructed spectroscopic images of an absorber array. The image reconstructed from the time domain signal was only ascertainable at a specific delay and would have been nearly impossible to find without the imaging process. According to the image reconstructed from the frequency dependent power spectrum, the array seems to exhibit stronger absorption near its edges indicating that the quality of the individual elements around the outside of the array may be better than that of the elements more toward the center of the array.

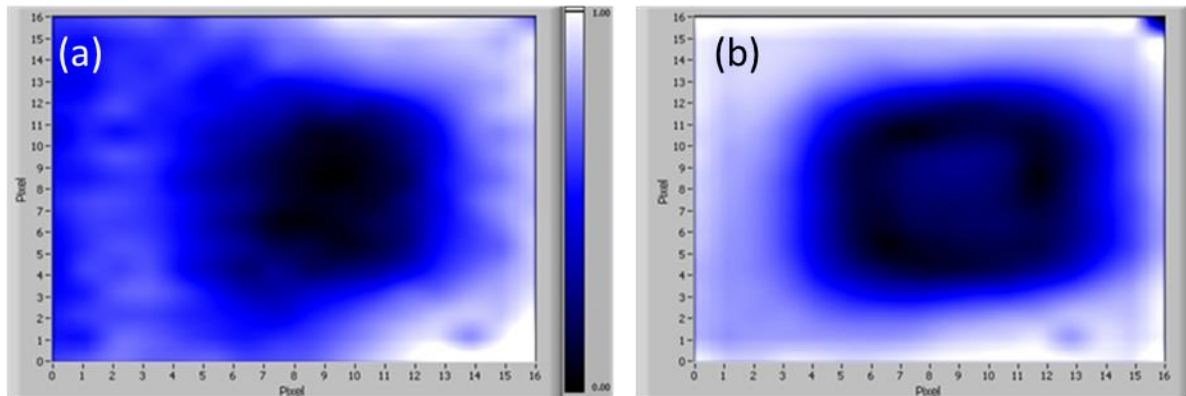


Figure 6.23. Reconstructed images of an absorber array based on (a) time domain amplitude and (b) frequency dependent power.

## 6.6. Conclusion

The absorber devices presented in this chapter were designed by finite element numerical simulation and fabricated by standard photolithography and lift-off process. These absorbers have proven to exhibit near perfect absorption through reflection mode THz-TDS. It was shown that the absorption of these devices is insensitive to the polarization of the incident terahertz frequency radiation when the device has four-fold symmetry as shown in the 4-T structure or can be highly polarization dependent as shown in the 2-T structure. The important parameters necessary to successfully target a resonant frequency and absorption strength were seen to be the outer length of the resonator element, the gap lengths, and the dielectric spacer thickness. These devices could be suitable for frequency selective detection applications.

## CHAPTER 7

### FLEXIBLE ABSORBERS

#### 7.1. Flexible Device Background

Research and development of flexible electronic devices, which began at least as far back as the early 1900s, has seen great technological strides over the past couple decades. Flexible electronic devices can be especially advantageous when the space and weight constraints for the packaging of the device are critical factors such as in cameras, cellular phones, automobiles, and even rockets and satellites. Flexible electronic devices have many envisioned and realized applications. Some of the realized applications, which are shown in Figure 7.1, include flexible displays<sup>180</sup>, solar cells<sup>181</sup>, and circuits for medical devices.<sup>182</sup> Flexible electronic interconnections are used in numerous automotive systems including the dashboard instrument panels and anti-lock braking systems.

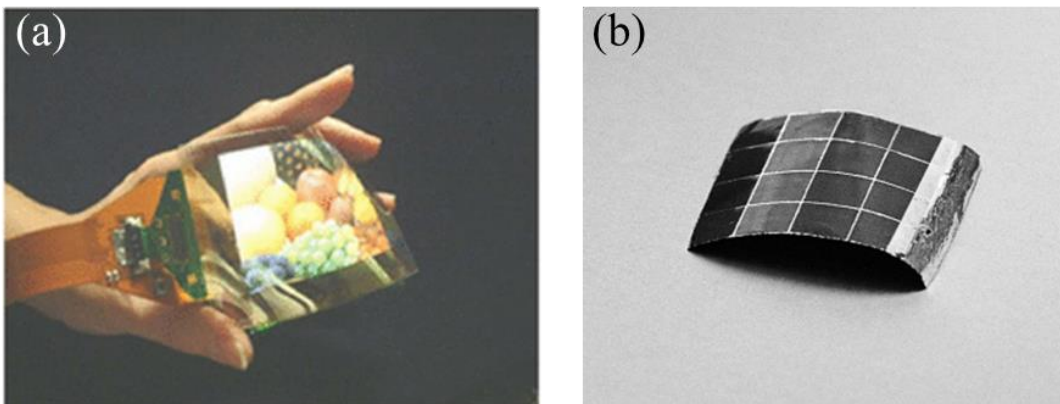


Figure 7.1. (a) Flexible OLED display<sup>180</sup> and (b) flexible ZnO/CdS/Cu(In,Ga)Se<sub>2</sub>/Mo/polyimide stack solar cell.<sup>181</sup>

Flexible metamaterials can offer many advantages that include the ability to be placed in unusual places and conform to surfaces which would be beneficial for facilitating cloaking applications. Flexible materials often have increased durability as well. The ability to produce flexible metamaterials can open an entirely new set of applications. There has recently been a great deal of research on flexible metamaterials.

Commonly used flexible substrate materials include polyimide<sup>183,184,185</sup> and poly(ethylene naphthalate) (PEN)<sup>186,187</sup> which provide excellent flexibility and high resistance to solvents, acids, and bases. These types of substrates can either be purchased or deposited on a sacrificial substrate during device fabrication and subsequently removed. Both materials have been shown to be suitable for terahertz metamaterials because they have high transparency at terahertz frequencies.

Numerous flexible metamaterial devices have been reported.<sup>188,189</sup> Flexible metamaterial devices have been proven useful for several applications. One group in particular recently designed and fabricated a flexible metamaterial with the goal of completing the spectrum of achievable refractive index by pushing it into the high positive regime. The device was composed of “I”-shaped resonators that exhibited an unnaturally high index of refraction of 33.2 at 0.33 THz<sup>185</sup>, the structure of which is presented in Figure 7.2. The device is expected to be beneficial for design flexibility in transformation optics applications.

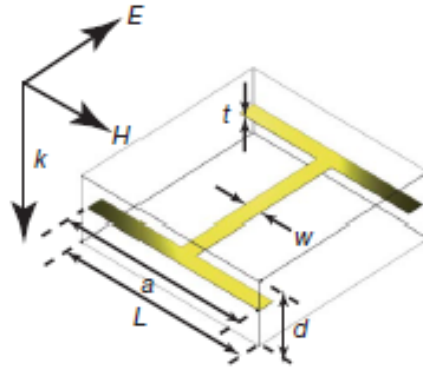


Figure 7.2. Diagram of a flexible metamaterial resonant element unit cell that was reported to achieve a refractive index of 33.2 at 0.33 THz.<sup>185</sup>

Flexible metamaterial absorbers have also been investigated.<sup>183,190,191,192,193</sup> A flexible broadband absorber was reported that used dielectric surface relief structures instead of metallic resonators as shown in Figure 7.3. The flexible absorber was fabricated by using a silicon wafer that had the surface relief pattern etched (through a combination of reactive ion etching and wet etching) into it. The etched wafer was then used as a template with liquid polydimethylsiloxane (PDMS) applied. After baking the PDMS film, it was removed from the silicon and shown to exhibit 99% absorbance over the range from 0.75 THz to 2 THz.<sup>192</sup>

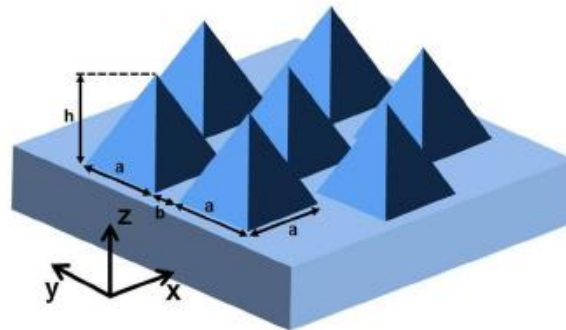


Figure 7.3. Diagram of a flexible broadband absorber that was reported to achieve 99% absorbance from 0.75 THz to 2 THz.<sup>192</sup>

By fabricating SRRs on a polyimide substrate, another group was able to use the device as a wireless strain sensor.<sup>184</sup> The device was designed to operate in the microwave region at 12 GHz and composed of dual concentric square SRRs as the FSS layer with a SiN layer serving as the dielectric spacer separating the FSS from the ground plane. Kapton (polyimide) tape was used for the substrate. The device was seen to have a linearly proportional relationship between the absorption and the strain on the device based on the change in capacitance between the SRRs and the ground plane during the mechanical straining of the device. Other groups have also reported similar devices based on SRRs of various geometries.<sup>194,195</sup>

## 7.2. Flexible Absorber Simulation

The flexible absorbers in this work were designed using the three layer approach containing a bottom copper ground plane and top FSS layer, consisting of copper resonators, separated by a dielectric spacing layer. The FSS unit cell for the flexible absorber consisted of two differently sized, nonconcentric, out-of-plane rings separated by a 1.7  $\mu\text{m}$  thick dielectric (polyimide) layer as given in Figure 7.4. The device was designed with the larger ring in the upper layer because larger sized resonators require a greater dielectric spacing thickness for optimization.

A series of eight arrays with FSS ring center-to-center spacing (distance between the centers of the top ring and bottom rings) ranging from 2  $\mu\text{m}$  to 9  $\mu\text{m}$  were simulated to determine the effect of this spacing on the resonant frequencies and absorption strength at each frequency. Table 7.1 summarizes the design parameters for the eight different devices.

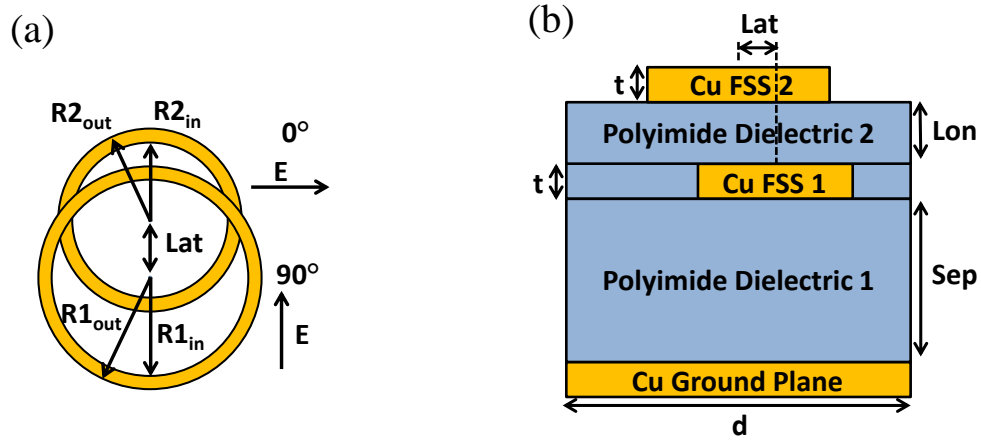


Figure 7.4. Diagrams of (a) the top view of the FSS layer consisting of two nonconcentric rings with center-to-center spacing represented by  $Lat$  and labeled incident field polarizations. (b) Side view of the flexible absorber unit cell where  $sep$  and  $Lon$  represents the dielectric spacing layer thicknesses between the ground plane and the FSS and two rings composing the FSS, respectively.

These center-to-center spacings from the simulations were later used to design the photomask used for the fabrication of the devices. According to the design, the FSS top layer of rings is fixed, with all of the displacement differences between devices occurring due to a translation of the FSS bottom layer of rings.

	Device 1	Device 2	Device 3	Device 4	Device 5	Device 6	Device 7	Device 8
Bottom Ring ( $R2_{in}-R2_{out}$ )	33-36	33-36	33-36	33-36	33-36	33-36	33-36	33-36
Top Ring ( $R1_{in}-R1_{out}$ )	39-42	39-42	39-42	39-42	39-42	39-42	39-42	39-42
Displacement ( $Lat$ )	2	3	4	5	6	7	8	9

Table 7.1. The first and second rows give the FSS bottom and top ring, respectively, inner-outer radii for each device. The third row gives center-to-center displacement, referred to by the term  $Lat$  in Figure 7.4, for the FSS rings for each device.

The COMSOL Multiphysics RF Module was again used for the simulations. Once the model geometry had been built with the boundary conditions set, a mesh was applied as seen in Figure 7.5. At this point the simulation of the device was ready to be performed.

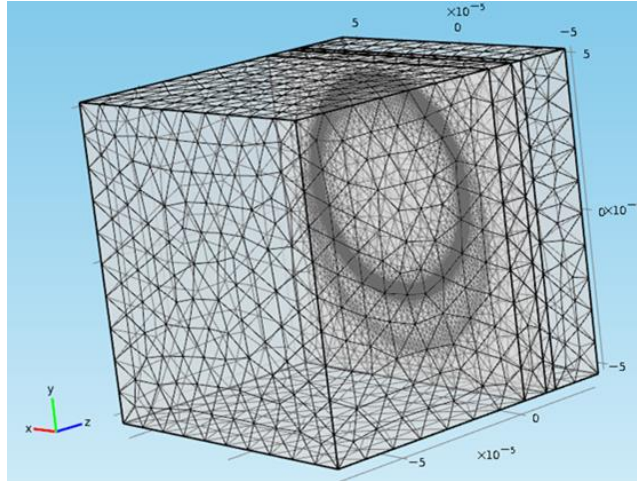


Figure 7.5. Flexible absorber simulation model geometry with applied mesh.

The first characteristic observed, was the induced currents on the ring based on the simulation results. In the simulations, the currents induced on the rings at the resonant frequency seemed to have dipole oscillations. The simulated currents in the two rings oscillate in opposite directions as seen in Figure 7.6.

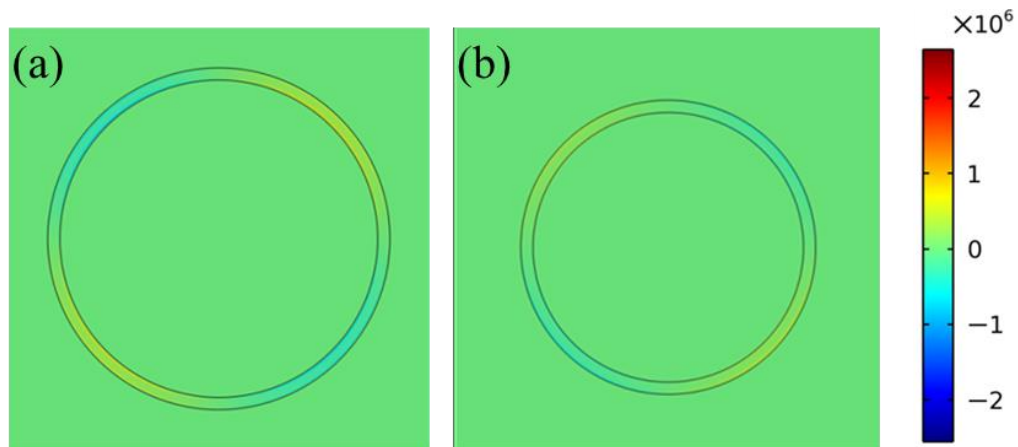


Figure 7.6. Simulated surface currents on (a) the front ring and (b) the back ring of the FSS unit cell.

The electric field densities in the proximity of the rings from simulation are shown in Figure 7.7. As expected from the ring currents, the electric field also appears to be exhibiting dipole oscillation when excited at the resonant frequency.

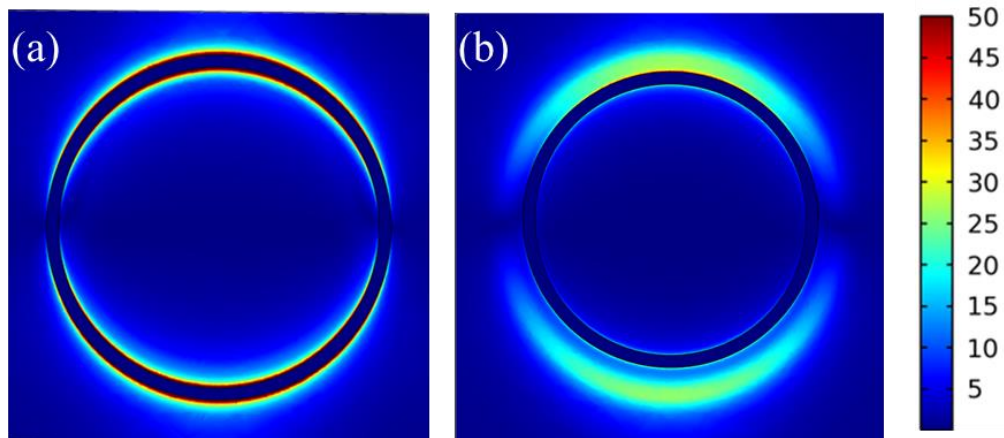


Figure 7.7. Simulated electric field density in near proximity to (a) the front ring and (b) the back ring of the FSS unit cell.

A series of simulations was run with varied center-to-center distances between the rings in the unit cell ranging from  $2\ \mu\text{m}$  to  $9\ \mu\text{m}$  as was indicated in Table 7.1. In the same manner as the SRRs, the flexible absorber devices were simulated at  $0^\circ$  and  $90^\circ$  by rotating the polarization of the radiative source where  $0^\circ$  implies that the electric field is perpendicular to the center-to-center ring translation vector and  $90^\circ$  implies that the electric field is parallel to that vector. The simulated absorbance of the device is given in Figure 7.8 for both rotations.

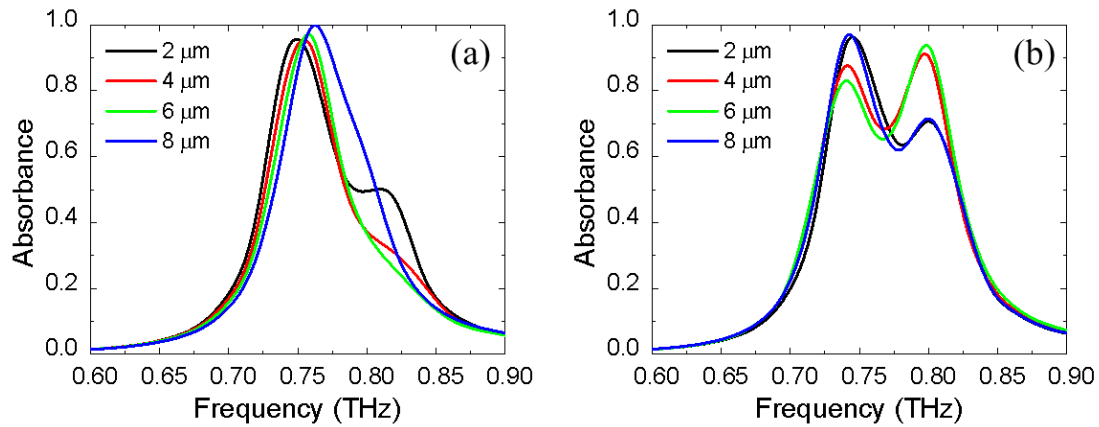


Figure 7.8. Simulated absorbance of the flexible absorber at (a)  $0^\circ$  and (b)  $90^\circ$ .

In the  $0^\circ$  orientation, only a single absorption peak is observed at 0.75 THz (between 0.74 and 0.76 THz for all four spacings) except for a second, less visible peak seen for the device with 2  $\mu\text{m}$  center-to-center spacing at 0.82 THz. The 0.75 THz absorption peak for the  $0^\circ$  orientation did not show significant change in magnitude either. However, the magnitude of the two absorption peaks seen at 0.74 THz and 0.8 THz in the  $90^\circ$  orientation varied inversely as the center-to-center spacing between the rings was swept from 2  $\mu\text{m}$  to 8  $\mu\text{m}$ , with the 0.8 THz peak rising to a maximum in the middle of the sweep. Based on these findings, it was speculated that the flexible device could be utilized to detect the mechanical translation of the rings with respect to each other. The simulations were used to target the appropriate ring sizes to be used for fabrication of the device.

### 7.3. Flexible Absorber Fabrication

The largest portion of my work on this project was designing a fabrication process by which a flexible platform could be built to fabricate not only the flexible absorbers, but other future flexible metamaterial devices as well. In order to make the device flexible, it was fabricated on a polyimide substrate which was deposited onto a silicon wafer without the use of the VM-651 adhesion promoter. At the time of fabrication, this process had not been performed previously, so testing was required. To begin the fabrication process, a layer of polyimide was applied to a small piece of silicon, followed by the optimized curing procedure defined in the Chapter 6. When the sample was removed from the furnace after hard baking at 350°C, the polyimide film had developed a large bubble underneath it as seen in Figure 7.9 (left). Subsequent attempts seemed to randomly yield samples both with and without formed bubbles. It was speculated that particulates on the substrate surface could be causing the bubbles to form.

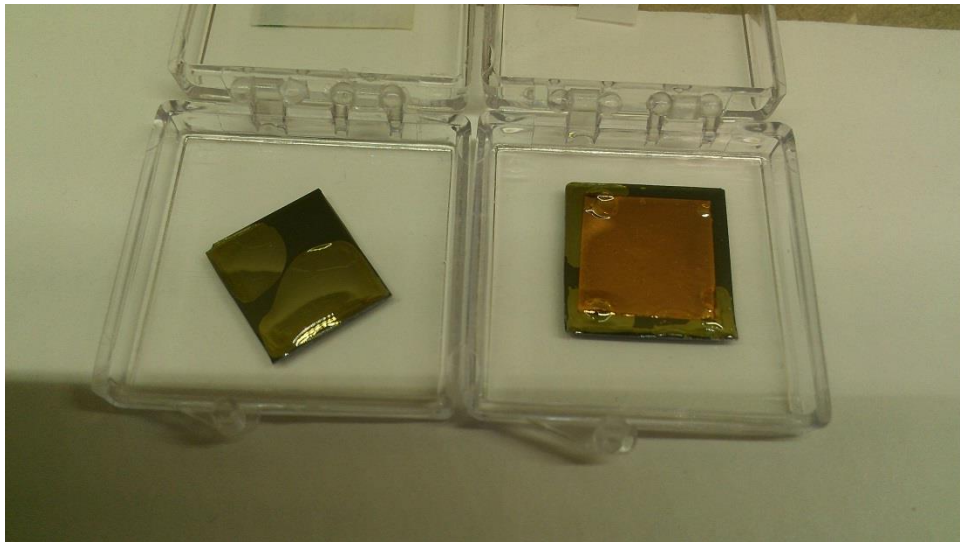


Figure 7.9. Picture of polyimide bubbles on bare silicon (left) and after copper deposition (right).

Several small pieces were processed in parallel to ensure some of the pieces would not have bubbles. A metal (15 nm chromium and 185 nm copper) layer was deposited on top of the pieces that survived which would serve as the ground plane for the device. After the metal deposition, the first polyimide dielectric spacing layer was applied and cured. Many of these pieces developed bubbles in the polyimide near the corners of the metal layer as shown in Figure 7.9 (right). A single piece survived this stage. The FSS pattern was deposited onto this piece through the photolithographic lift-off procedure. The device was then removed from the silicon as shown in Figure 7.10.

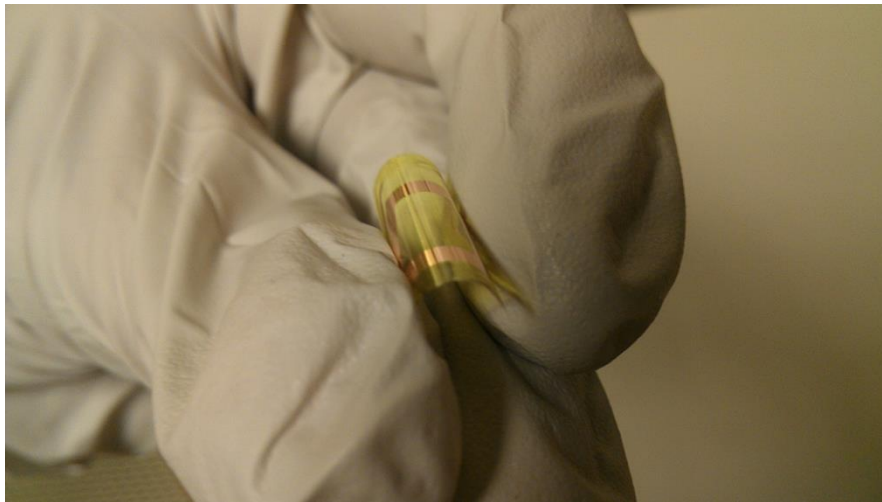


Figure 7.10. Picture of successful fabrication test device.

This proved the feasibility of using the polyimide substrate for the fabrication of a flexible device, but the FSS structures were not correct for the small test piece due to the polyimide edge bead. In order to lessen the effect, the procedure was attempted again with a full 3 inch silicon wafer instead of a small piece. This proved effective as the actual interface between the mask and the sample was much further away from the polyimide edge bead allowing for successful fabrication of the device as shown in Figure 7.11.

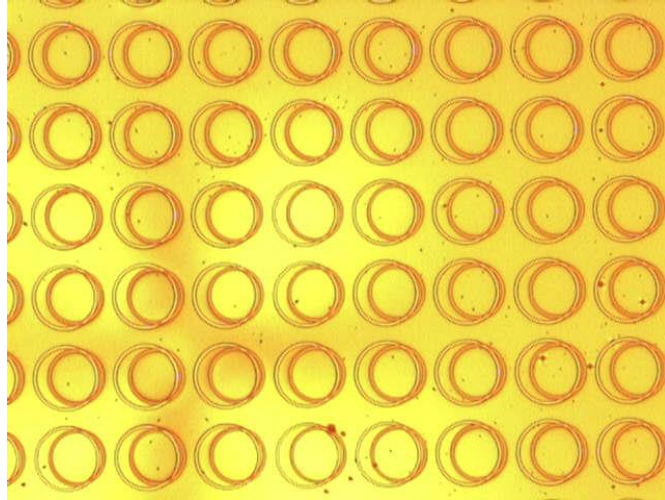


Figure 7.11. Optical microscope image of the flexible absorber.

A secondary goal in the fabrication of the flexible absorber device was to attempt to design the device such that the FSS layers would undergo different deformation during stretching of the device. In order to facilitate this goal, the fabrication of the final devices was changed so that the bottom layer of rings in the FSS would be encapsulated in a distinct  $\text{SiO}_2$  layer as shown in Figure 7.12. This was accomplished by depositing a 250 nm  $\text{SiO}_2$  layer on the first polyimide spacing layer. Photoresist was spin coated onto the  $\text{SiO}_2$  layer and patterned with the first FSS layer rings. The exposed ring patterns in the  $\text{SiO}_2$  layer were then etched 200 nm by ion milling followed by the chromium/copper deposition of the rings. After lift-off, the cap layer of  $\text{SiO}_2$  was deposited ensuring the rings were fully enclosed. At this point, the rest of the fabrication process was completed normally with the application of the second polyimide spacing layer and subsequent second FSS ring layer photolithography, deposition, and lift-off.

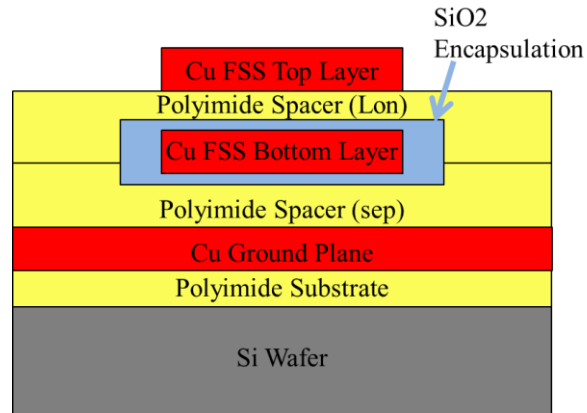


Figure 7.12. Side view diagram of the layers in the fabricated flexible absorber.

#### 7.4. THz-TDS Measurement of the Flexible Absorbers

The flexible absorber arrays were first measured while still attached the silicon wafer. This was performed in the same manner as the 2-T and 4-T absorber arrays with the Z-2 in reflection mode. The sample was also positioned in the beam path with the steel holder plate mounted on the motion controlled stage. After these measurements had been completed, the polyimide film was removed from the silicon substrate. The measurement of the flexible device required the reconfiguration of the sample mounting procedure. For the reflection mode measurement, the sample should be flat and close to normal to the terahertz pulse path. The polyimide film, once removed from the silicon wafer, would roll up into a cylinder. It was necessary to clamp the film on both sides to pull it flat. This was accomplished by using the motion controlled stage as a clamping base on one side and a 90° angle bracket on the other side. Optical post clamps were used to clamp the film on both sides. This modified setup is shown in Figure 7.13.

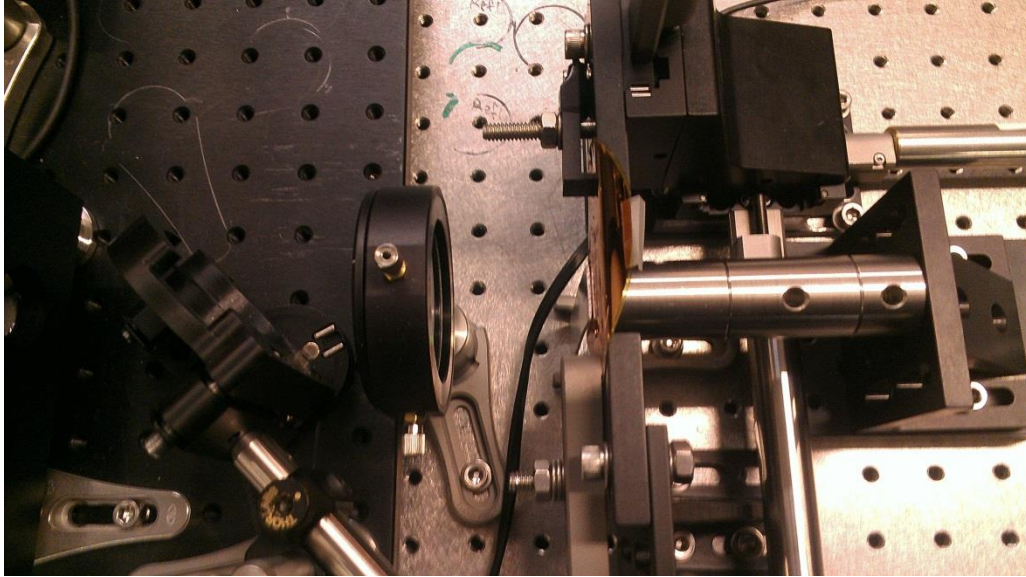


Figure 7.13. Photograph of the measurement setup for the flexible absorber.

This setup also made it possible to test the function of the device as a sensor. When mounted, the motion controlled stage could be used to stretch the devices laterally. First, all of the fabricated devices were measured in a flat, but not stretch position, in both  $0^\circ$  and  $90^\circ$  orientations. Afterwards, stretching of the devices was performed between measurements based on the position of the motor on the motion controlled stage.

Because these types of structures could lead to future applications in cloaking, it was desired to see how the flexible absorbers would respond to deformation. In order to characterize this type of a response, a suitable sample holder was designed with AutoDesk Inventor and printed on an Objet 3-D printer at the University of Alabama College of Engineering 3-D print shop as seen in Figure 7.14.

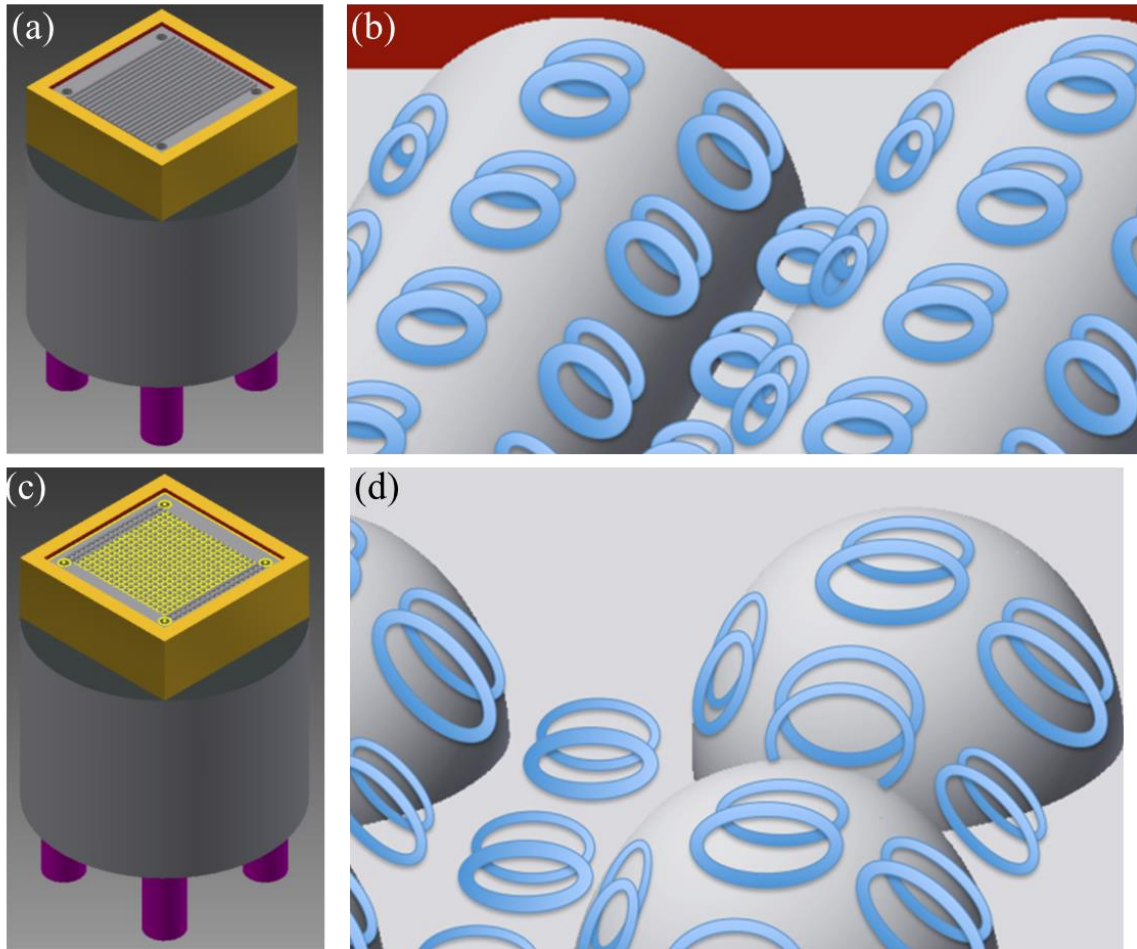


Figure 7.14. Diagram of the (a) cylindrical and (c) spherical deformation vacuum holders and illustrations of device conformation to the (b) cylindrical and (d) spherical surface relief structures.

The design included a recessed region that was covered with an array of surface structures, which when evacuated, would pull the flexible absorber sample into conformal contact. Two different holders were printed with one containing cylindrical deforming structures and the other containing hemispherical deforming structures. Vacuum ports were placed on the side opposed to the recessed sample mounting side. The body of the holder was made to be cylindrical with a 1 inch diameter so the holder could be mounted in a tilting 1 inch mirror mount.

Over several iterations of printing, the minimum resolvable printing size of the surface structures in the recessed region was determined to be  $500\ \mu\text{m}$ . Therefore, the diameter of both the half-cylinders and hemispheres were set at this value. The hemispheres were laid out in a 19 by 23 structure array with a  $600\ \mu\text{m}$  lattice constant so that the spacing between the hemispheres was  $100\ \mu\text{m}$ . The half-cylinders extend nearly the entire distance across the recessed surface and were also laid out with  $100\ \mu\text{m}$  spacing between the cylinders.

Figure 7.15 shows the vacuum holder setup incorporated into the measurement scheme in the Z-2. Similar to the previous reflection mode setup and alignment, the mirror mount was used to align the holder (with a plain flat mirror mounted to the holder) such that the incident terahertz

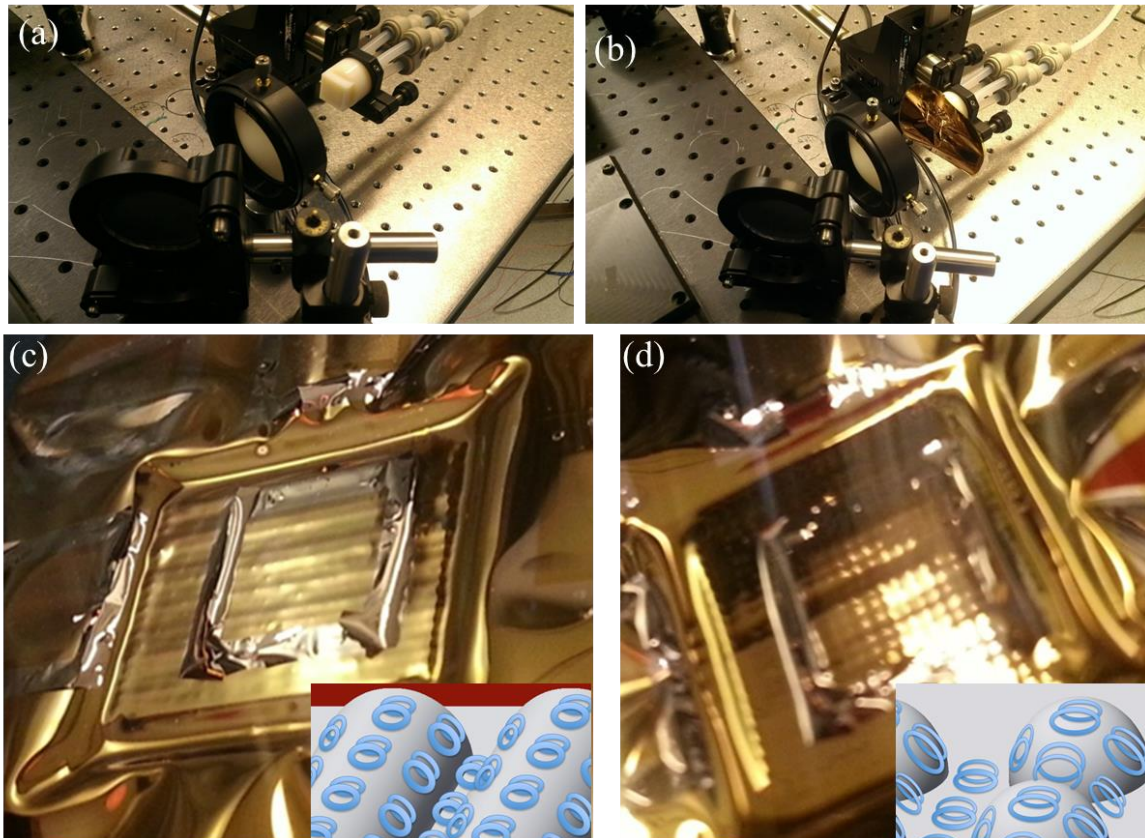


Figure 7.15. Pictures of a vacuum holder (a) without and (b) with flexible absorber sample mounted and pictures of the an array mounted on the (c) cylindrical and (d) hemispherical surface relief vacuum holders with insets showing diagrams of the unit cells overlaid on the surface relief structures for clarity.

pulse path was normal to the plane of the mirror. Measurements were performed with the flexible absorbers mounted in both  $0^\circ$  and  $90^\circ$  orientations.

### 7.5. Flexible Absorber THz-TDS Results

The measured absorbance at resonance of the arrays before being removed from the sacrificial silicon wafer were seen to match with those in the simulations for the  $0^\circ$  polarization measurements as seen in Figure 7.16 except for a 10 GHz shift in resonant frequencies. At first glance, the appearance of the second resonance at the  $90^\circ$  polarization was not obvious, but the slight broadening of the resonance peak gave an indication that the second resonance was indeed present. The broadening was much more pronounced in the  $4\ \mu\text{m}$  and  $6\ \mu\text{m}$  center-to-center displacement structures which were predicted in the simulations to exhibit maximums at the second resonant frequency. It was speculated that the two resonant frequencies may be slightly shifted closer together due to some type of interaction between the two layers of FSS rings in the unit cell.

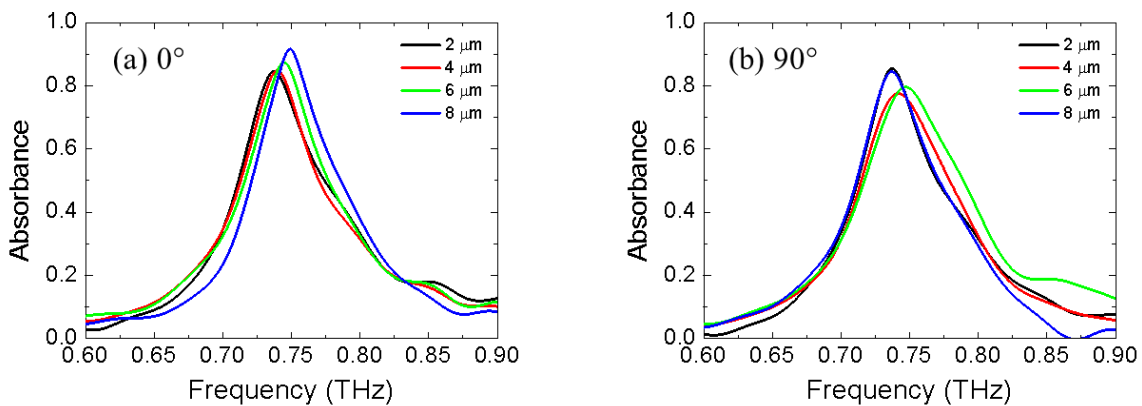


Figure 7.16. Measured absorbance for flexible absorber arrays with center-to-center spacings of  $2\ \mu\text{m}$ ,  $4\ \mu\text{m}$ ,  $6\ \mu\text{m}$ , and  $8\ \mu\text{m}$  at (a)  $0^\circ$  and (b)  $90^\circ$  before removal from the silicon wafer.

Except for a 5 GHz redshift in the measured resonant frequency, the measured absorbance of the structures at both polarizations still matched with the simulated values after being removed from the silicon wafer. With the exception of the 2  $\mu\text{m}$  center-to-center spacing structures, the flexible absorbers exhibited better than 90% absorption at  $0^\circ$  polarization. This can be seen in Figure 7.17. The second absorption resonance expected at 0.8 THz still seems to have redshifted slightly to the point where the two resonance peaks have a significant overlap at the  $90^\circ$  polarization with increased broadening as the center-to-center distance changes between 4  $\mu\text{m}$  and 6  $\mu\text{m}$ .

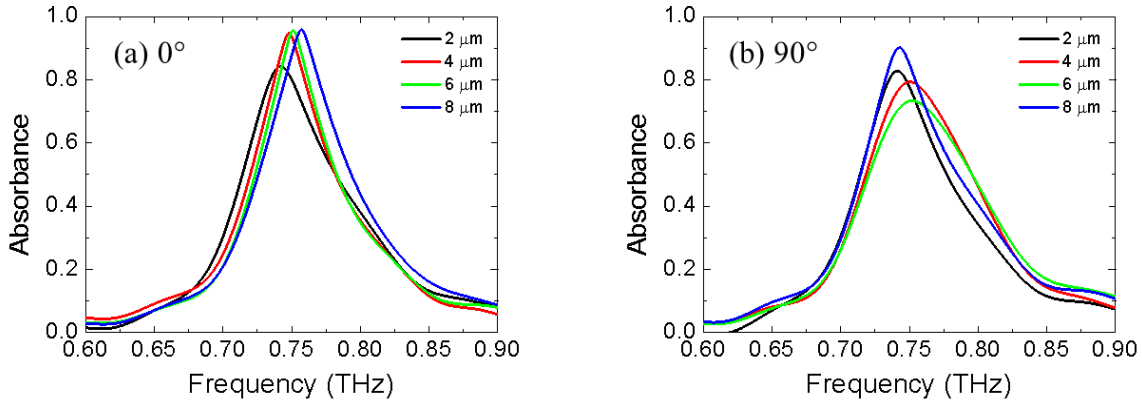


Figure 7.17. Measured absorbance spectra for flexible absorber arrays with center-to-center spacing of 2  $\mu\text{m}$ , 4  $\mu\text{m}$ , 6  $\mu\text{m}$ , and 8  $\mu\text{m}$  at (a)  $0^\circ$  and (b)  $90^\circ$  polarization after removal from the silicon wafer.

The flexible absorbers were also measured while being stretched, after removal from the silicon wafer. The structures were seen to exhibit absorption nearly identical to that seen before stretching in terms of both resonant frequency and absorbance strength to within the tolerance of the measurement during stretching, but the actual stretching of the arrays had negligible effect upon the absorbance spectra as seen in Figure 7.18.

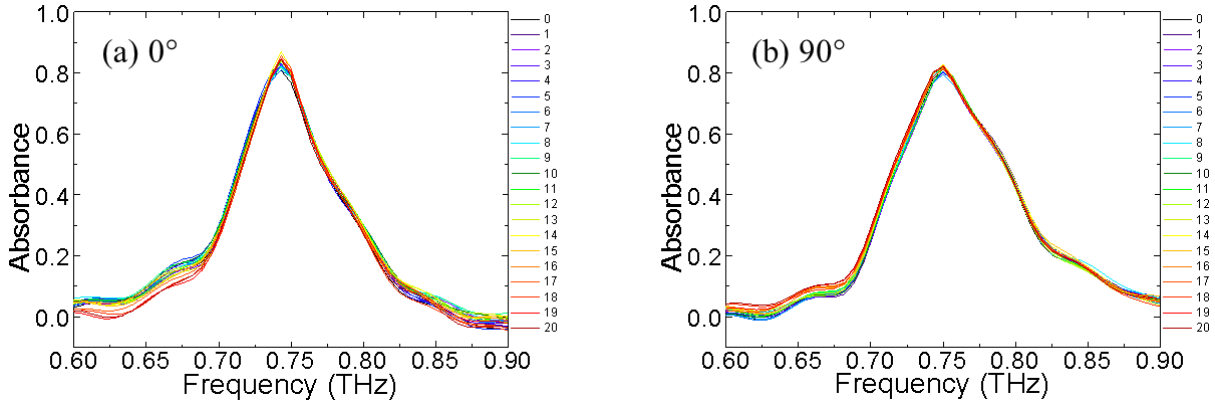


Figure 7.18. Measured absorbance for flexible absorber arrays with center-to-center spacings of  $2\ \mu\text{m}$ ,  $4\ \mu\text{m}$ ,  $6\ \mu\text{m}$ , and  $8\ \mu\text{m}$  at (a)  $0^\circ$  and (b)  $90^\circ$  during stretching. Legend gives the displacement as read from the motor position of the motion controlled stage.

Upon seeing little effect from stretching, the measurement setup was shifted so that a stereomicroscope could be positioned to view the arrays while being stretched as seen in Figure 7.19. The rings in the FSS did not show any signs of displacement with respect to each other or elongation of the rings themselves into a more elliptical shape. An optical microscope image of a stretched array is given in Figure 7.20. It was speculated that while the polyimide has suitable out-of-plane flexibility (meaning it can be rolled), it was too rigid to be adequately stretched by this method.

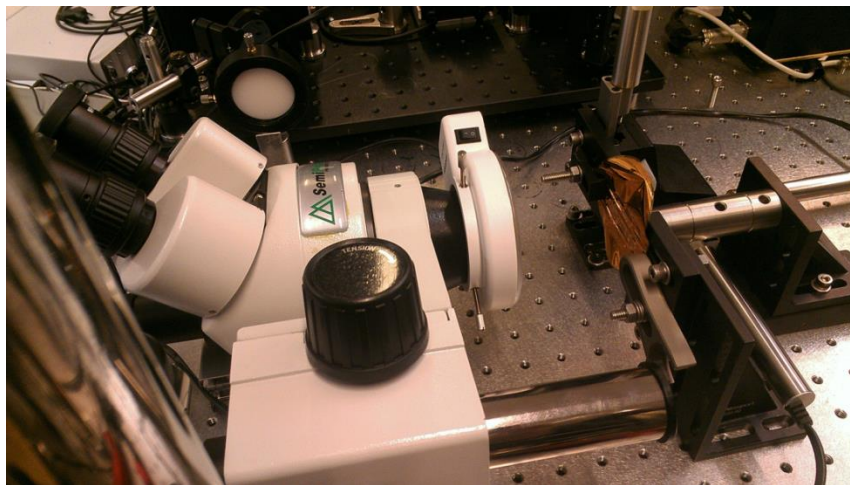


Figure 7.19. Modified measurement setup to allow microscope viewing of the arrays during stretching.

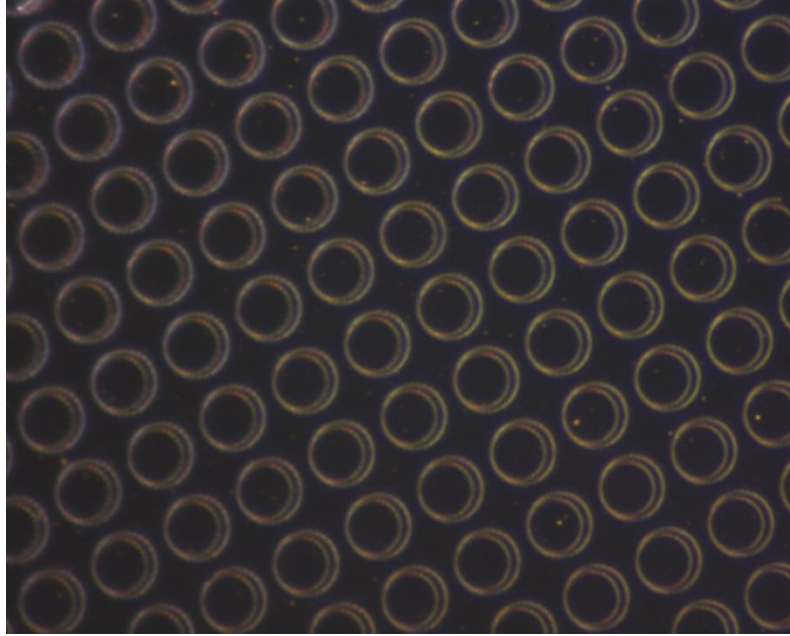


Figure 7.20. Optical microscope picture of flexible absorber array during stretching.

Figure 7.21 shows the measured absorbance spectra of the flexible absorber structures at both polarizations while deformed with the cylindrical holder. The flexible absorbers were again seen to exhibit nearly identical absorbance at both polarizations while under deformation compared to measurements performed before removal from the sacrificial silicon wafer. Additionally, the absorbance broadening still occurs in the measurements at the  $90^\circ$  polarization.

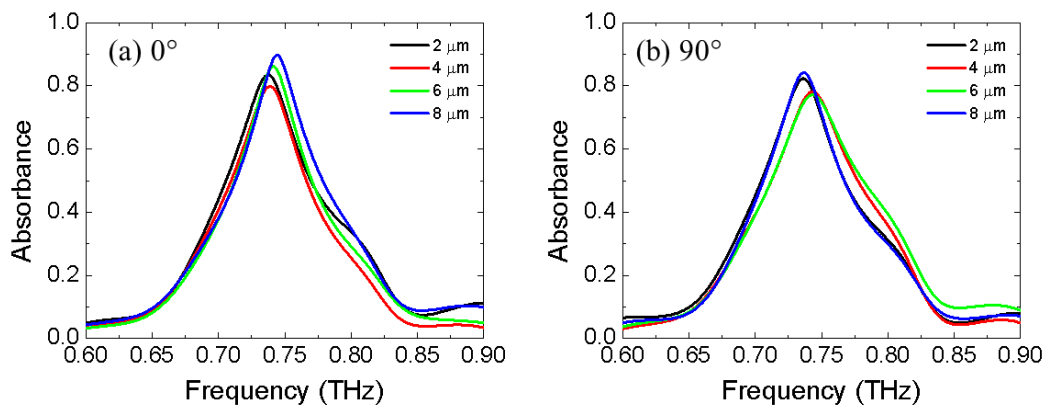


Figure 7.21. Absorbance spectra of flexible absorber devices at (a)  $0^\circ$  and (b)  $90^\circ$  when deformed by cylindrical vacuum holder.

The measured absorbance spectra of the flexible absorber devices while deformed with the hemispherical holder are given in Figure 7.22. The measurements with this holder were seen to match very closely to the previous measurements with the cylindrical vacuum holder.

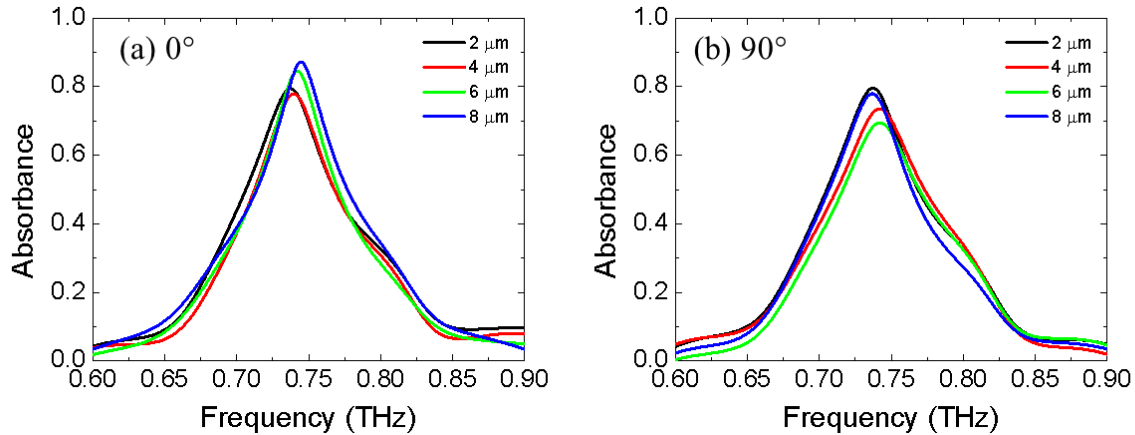


Figure 7.22. Absorbance spectra of flexible absorber devices at (a) 0° and (b) 90° when deformed by hemispherical vacuum holder.

Table 7.2 provides a summary of the measured absorbance peak frequency and strength for each of the devices measured. The values for both vacuum holder types indicated that the type of deformation seemed to have little effect on the operation of the absorber, and for that matter, the deformation itself had negligible effect on the structure functionality.

	2 μm				4 μm				6 μm				8 μm			
	0°		90°		0°		90°		0°		90°		0°		90°	
	THz	Abs														
Planar on Si	0.737	0.845	0.737	0.856	0.740	0.848	0.742	0.776	0.745	0.874	0.747	0.796	0.750	0.916	0.737	0.845
Cylinder	0.737	0.835	0.736	0.823	0.739	0.798	0.743	0.782	0.741	0.862	0.743	0.772	0.744	0.897	0.737	0.842
Hemisphere	0.737	0.794	0.737	0.796	0.740	0.780	0.742	0.735	0.742	0.845	0.742	0.694	0.745	0.872	0.737	0.779

Table 7.2. Absorbance at resonant frequency for each flexible absorber device at both 0° and 90° orientations for measurements with and without the vacuum holders.

## 7.6. Conclusion

The flexible absorber structures presented in this chapter were seen in simulation to exhibit strong absorption at resonance with frequency sensitivity to the center-to-center spacing of the rings composing the FSS. The fabrication procedure for these devices was difficult to optimize, but was found to be capable of producing a polyimide substrate on which future flexible devices can be realized. The measured structures matched well with simulation at the  $0^\circ$  polarization. At the  $90^\circ$  polarization, the two resonant frequencies were seen to have significant overlap which resulted in what looked like a single broadened resonant frequency. This was especially obvious in the  $4\ \mu\text{m}$  and  $6\ \mu\text{m}$  center-to-center displacement structures. Under stretching, the devices had nearly identical absorption with negligible change in absorption frequency or strength. The measurements performed with the 3-D printed vacuum holders showed that the operation of the flexible absorber devices has little dependence of the geometry of the deforming object. The structures were shown to maintain functionality around two dimensional curves which lends credence to the potential of these structures to lead to future applications in cloaking.

## CHAPTER 8

### CONCLUSION

#### 8.1. Summary of Findings

As metamaterials have begun to unlock our ability to manipulate radiation at terahertz frequencies, new applications for metamaterials are constantly being developed. The field of terahertz frequency metamaterials is and should continue seeing rapid growth as new discoveries continue to be made for the foreseeable future. This work has sought to address some terahertz technologies and many of the recent advances in the field of metamaterials operating at terahertz frequencies while providing a detailed summary and discussion of my research outcomes in this area including SRRs, perfect absorbers, and flexible absorbers.

The sample fabrication and measurement techniques employed for the SRR and perfect absorber samples were discussed in detail including the design and use of standard photolithography and lift-off processes, as well as E-beam metal deposition and THz-TDS measurement. Device fabrication was seen to become progressively more complicated in the progression from SRRs to flexible absorbers. The design and simulation of the devices was also discussed with the simulation being used to predict device operating (resonant) frequencies and mechanisms of absorption.

The SRRs studied in this work included single layer, passivated layer, and dual layer arrays of dual square concentric SRRs. The results of this study included the comparison of simulation to actual measurement of the SRR arrays as well as evaluation of the SRR size on resonant frequency. The SRR arrays were seen to develop two distinct and switchable LC

resonances as well as a dipole resonance by measuring the arrays at  $0^\circ$  and  $90^\circ$  in-plane rotations about the terahertz pulse path. Particular emphasis was given to the observed effects of the addition of a passivation layer and second layer of split-ring resonators. The addition of the passivation layer served to effectively lower the resonant frequencies of the SRRs. The dual SRR layer array was seen to have a slight modulating effect on the absorption strength at the resonant frequencies compared to that of the passivated array without the second SRR layer. The SRR results are soon to be published.<sup>196</sup>

All of the absorbers fabricated for this work were designed with the three layer approach using a FSS layer, a conducting metal ground plane and a spacing dielectric layer which separates the previous two layers. For the 2-T and 4-T perfect absorbers, the FSS layer consisted of single layer metallic ELC resonators, where the 2-T absorbers were polarization dependent, and the 4-T absorbers were insensitive to the polarization of the incident radiation. The polarization sensitivity of the absorbers was characterized through reflection mode THz-TDS by rotating the absorber arrays in-plane about the terahertz pulse path in order to simulate the change in incident polarization. The polarization insensitivity of the 4-T absorbers was modeled with an equivalent circuit model which was used to explain the phenomena. Both the effect of absorber size parameter dimensions and the dielectric spacing layer thickness were investigated with the size dimensions seen to control the resonant frequencies, and the dielectric spacing layer thickness seen to modulate the strength of absorption. The absorbance of the devices was seen to be broadened compared to that seen in the simulation with the broadening effect attributed to a reduction in the conductivity of the deposited copper ELCs. Reconstructed images based on time and frequency domain spectroscopic data were also presented. The 4-T absorber results have been recently published.<sup>197</sup>

The flexible absorber FSS consisted of dual layer single, circular rings separated by an additional dielectric (polyimide) spacing layer. Simulation showed that the resonant absorption strength, and to a lesser extent, the resonant frequencies of the device were dependent upon the center-to-center spacing of the FSS rings, leading to the suggestion that the device could have a possible application as a stress/strain sensor. The measurement results for the structures showed that the resonant frequencies and absorbance strengths were well matched with those from simulation, although the subsequent stretching of the device during measurement yielded no visible change in either the resonant frequencies or absorption strengths. Measurements with the custom vacuum holders revealed that the functionality of the flexible absorbers is not affected by deformation, regardless of the shape. Furthermore, these structures were seen to maintain functionality around a two dimensional curve which means they could lead to future applications in cloaking.

## 8.2. Future Work

The SRR measurements designed to isolate the magnetic component of the incident radiation did not yield meaningful results because the SRRs were so small compared to the cross section of the terahertz pulse path. Through the proper design and implementation of a waveguide, which could effectively compress the terahertz pulse path cross section, this difficulty could be overcome and allow for successful measurement of the SRR arrays in this orientation. The most likely candidate for this would be a simple parallel plate waveguide. However, additional work would be needed to determine the appropriate method for coupling the terahertz pulses into the waveguide.

The next logical step for the planar perfect absorbers is incorporation into an active device. This could be in the form of a bolometric scheme for detection or sensing. These absorbers could also be incorporated into a transmission based communications system to serve as an optical attenuator or modulator.

The flexible absorber device has several tasks that would be required before being useful in the envisioned application as a stress/strain sensor. The measurements of the device revealed that the out-of-plane rings in the FSS did not move relative to each other during the stretching measurements, so the first task would be the determination of a new, stronger method of stretching the flexible absorbers that could allow for characterization of the structures for this purpose. Additionally, although the polyimide substrate is quite flexible, a new, even more flexible material could allow for more mobility of the ring structures composing the FSS. The third task would be to better characterize exactly how the surface of the flexible absorber is deformed during deformation by the vacuum holders so that more accurate simulation models may be constructed. Finally, it may also prove possible to use a single layer of rings to realize this applications if the material is sufficiently flexible to allow a single ring to be stretched from spherical to elliptical.

## REFERENCES

1. B. Ferguson, X. -C. Zhang, "Materials for terahertz science and technology," *Nature Mater.* 1, 26-33 (2002).
2. P. Shumyatsky and R. R. Alfano, "Terahertz sources," *Journ of Biomedical Optics* 16 (3) 033001 (2011).
3. W. Faries, K. A. Gehring, P. L. Richards, and Y. R. Shen, "Tunable far-infrared radiation generated from difference frequency between two ruby lasers," *Phys. Rev.* 180 (2), 363–365 (1969).
4. J. R. Morris, and Y. R. Shen, "Far-infrared generation by picosecond pulses in electro-optical materials," *Opt. Commun.* 3 (2), 81–84 (1971).
5. K. H. Yang, P. L. Richards, and Y. R. Shen, "Generation of far-infrared radiation by picosecond light pulses in LiNbO<sub>3</sub>," *Appl. Phys. Lett.* 19 (9), 320–323 (1971).
6. T. Yajima, and N. Takeuchi, "Far-infrared difference-frequency generation by picosecond laser pulses," *Jpn. J. Appl. Phys.* 9 (11), 1361–1371 (1970).
7. D. H. Auston, K. P. Cheung, J. A. Valdmanis, and D. A. Kleinman, "Cherenkov radiation from femtosecond optical pulses in electro-optic media," *Phys. Rev. Lett.* 53 (16), 1555–1558 (1984).
8. B. B. Hu, X. -C. Zhang, D. H. Auston, and P. R. Smith, "Free-space radiation from electrooptic crystals," *Appl. Phys. Lett.* 56 (6), 506–508 (1990).
9. P. Shumyatsky and R. R. Alfano, "Terahertz sources," *Journ. Biomed. Opt.* 16 (3), (2011).
10. P. R. Smith, D. H. Auston, and M. C. Nuss, "Subpicosecond photoconducting dipole antennas," *IEEE J. Quantum Electron.* 24 (2), 255–260 (1988).
11. Ch. Fattering and D. Grischkowsky, "Terahertz beams," *Appl. Phys. Lett.* 54 (6), 490–492 (1989).
12. N. Katzenellenbogen, and D. Grischkowsky, "Efficient generation of 380 fs pulses of THz radiation by ultrafast laser pulse excitation of a biased metal semiconductor interface," *Appl. Phys. Lett.* 58 (3), 222–224 (1991).
13. D. H. Auston and M. C. Nuss, "Electrooptic generation and detection of femtosecond electrical transients," *IEEE J. Quantum Electron.* 24 (2), (1988).

14. J. T. Darrow, B. B. Hu, X. -C. Zhang, and D. H. Auston, "Subpicosecond electromagnetic pulses from large-aperture photoconducting antennas," *Opt. Lett.* 15 (6), 323-325, (1990).
15. A. G. Davies, E. H. Linfield, and M. B. Johnston, "The development of terahertz sources and their applications," *Phys. Med. Biol.* 47, 3679-3689 (2002).
16. M. Born and E. Wold, "Principles of optics," Seventh Edition, Cambridge University Press (1999).
17. J. T. Darrow, X. -C. Zhang, D. H. Auston, J. D. Morse, "Saturation properties of large-aperture photoconducting antennas," *IEEE J. Quantum Electron* 28 (6), 1607-1616 (1992).
18. N. Sarukura, H. Ohtake, S. Izumida, and Z. Liu, "High average-power THz radiation from femtosecond laser-irradiated InAs in a magnetic field and its elliptical polarization characteristics," *J. Appl. Phys.* 84 (1), 654-656 (1998).
19. Q. Wu and X. -C. Zhang, "Free-space electro-optic sampling of terahertz beams," *Appl. Phys. Lett.* 67 (24), 3523-3525, (1995).
20. C. Kübler, R. Huber, and A. Leitenstorfer, "Ultrabroadband terahertz pulses: generation and field-resolved detection," *Semicond. Sci. Technol.* 20, S128-S133 (2005).
21. 21. Q. Wu and X. -C. Zhang, "Ultrafast electro-optic field sensors," *Appl. Phys. Lett.* 68 (12), 1604-1606 (1996).
22. 22. Q. Wu and X. -C. Zhang, "Electro-optic sampling of freely propagating terahertz fields," *Opt. Quantum Electron.* 28, 945 (1996).
23. M. Dyakonov and M. S. Shur, "Shallow water analogy for a ballistic field effect transistor: New mechanism of plasma wave generation by DC current," *Phys. Rev. Lett.* 71 (15), 2465-2468 (1993).
24. M. Dyakonov and M. S. Shur, "Detection, mixing, and frequency multiplication of terahertz radiation by two dimensional electronic fluid," *IEEE Trans. Electron Devices* 43 (3), 380-387 (1996).
25. T. Watanabe, S. B. Tombet, Y. Tanimoto, Y. Wang, H. Minamide, H. Ito, D. Fateev, V. Popov, D. Coquillat, W. Knap, Y. Meziani, and T. Otsuji, "Ultrahigh sensitive plasmonic terahertz detector based on an asymmetric dual-grating gate HEMT structure," *Solid-State Electronics* 78, 109-114 (2012).
26. C. Kistner, A. Andre, T. Fischer, A. Thoma, C. Janke, A. Bartels, T. Gisler, G. Maret, and T. Dekorsy, "Hydration dynamics of oriented DNA films investigated by time-domain terahertz spectroscopy," *Appl. Phys. Lett.* 90, 233902, 1-3 (2007).

27. B. M. Fischer, M. Hoffmann, H. Helm, R. Wilk, R. Rutz, T. Kleine-Ostmann, M. Kock, and P. U. Jepsen, "Terahertz time-domain spectroscopy and imaging of artificial RNA," *Opt. Exp.* 13, 5206-5215 (2005).
28. J.-Y. Chen, J. R. Knab, J. Cerne, and A. G. Markelz, "Large oxidation dependence observed in terahertz dielectric response for cytochrome C," *Phys. Rev. E. Rapid* 72, 04090, 1-4 (2005).
29. J. Knab, J. -Y. Chen, and A. Markelz, "Hydration dependence of conformational dielectric relaxation of lysozyme," *Biophys. J.* 90, 2576-2581 (2006).
30. A. Markelz, S. Whitmire, J. Hillebrecht, and R. Birge, "Terahertz time domain spectroscopy of biomolecular conformational modes," *Phys. Med. Biol.* 47, 3797-3805 (2002).
31. S. E. Whitmire, D. Wolpert, A. G. Markelz, J. R. Hillebrecht, J. Galan, and R. R. Birge, "Protein flexibility and conformational state: A comparison of collective vibrational modes of wild-type and D96N bacteriorhodopsin," *Biophys. J.* 85, 1269–1277 (2003).
32. A. G. Markelz, J. R. Knab, J. Y. Chen, and Y. He, "Protein dynamical transition in terahertz dielectric response," *Chem. Phys. Lett.* 442, 413-417 (2007).
33. J. -Y. Chen, J. R. Knab, S. Ye, Y. He, and A. G. Markelz, "Terahertz dielectric assay of solution phase protein binding," *Appl. Phys. Lett.* 90, 243901, 1-3 (2007).
34. M. Brucherseifer, M. Nagel, P. H. Bolívar, H. Kurz, A. Bosserhoff, and R. Büttner, "Label-free probing of the binding state of DNA by time-domain terahertz sensing," *Appl. Phys. Lett.* 77 (24), 4049-4051 (2000).
35. P. H. Bolívar, M. Nagel, F. Richter, M. Brucherseifer, H. Kurz, A. Bosserhoff, and R. Büttner, "Label-free THz sensing of genetic sequences: Towards 'THz biochips'," *Phil. Trans. R. Soc. Lond. A* 362, 323-335 (2004).
36. A. G. Markelz, A. Roitberg, and E. J. Heilweil, "Pulsed terahertz spectroscopy of DNA, bovine serum albumin and collagen between 0.06 to 2.00 THz," *Chem. Phys. Lett.* 320, 42-48 (2000).
37. K. Yamamoto, K. Tominaga, H. Sasakawa, A. Tamura, H. Murakami, H. Ohtake, and N. Sarukura, "Far-infrared absorption measurements of polypeptides and cytochrome c by THz radiation," *Bull. Chem. Soc. Japan* 75, 1083–1092 (2002).
38. D. Grischkowsky, S. Keiding, M. Van Exter, and Ch. Fattinger, "Far-infrared time-domain spectroscopy with terahertz beams of dielectrics and semiconductors," *J. Opt. Soc. Am. B* 7 (10), 2006-2015 (1990).

39. L. Duvillaret, F. Garet, and J. -L. Coutaz, "A reliable method for extraction of material parameters in terahertz time-domain spectroscopy," *IEEE J. Sel. Top. Quantum Electron.* 2 (3), 739-746 (1996).
40. S. C. Howells and L. A. Schlie, "Transient terahertz reflection spectroscopy of undoped InSb from 0.1 to 1.1 THz," *Appl. Phys. Lett.* 69 (4), 550-552 (1996).
41. S. S. Prabhu, S. E. Ralph, M. R. Melloch, and E. S. Harmon, "Carrier dynamics of low-temperature-grown GaAs observed via THz spectroscopy," *Appl. Phys. Lett.* 70 (18), 2419-2421 (1997).
42. H. Nemeč, A. Pashkin, P. Kuzel, M. Khazan, S. Schnüll, and I. Wilke, "Carrier dynamics in low-temperature grown GaAs studied by terahertz emission spectroscopy," *J. Appl. Phys.* 90 (3), 1303-1306 (2001).
43. P. Parkinson, H. J. Joyce, Q. Gao, H. H. Tan, X. Zhang, J. Zou, C. Jagadish, L. M. Herz, and M. B. Johnston, "Carrier lifetime and mobility enhancement in nearly defect-free core-shell nanowires measured using time-resolved terahertz spectroscopy," *Nano Lett.* 9 (9), 3349-3353 (2009).
44. K. Kawase, Y. Ogawa, Y. Watanabe, and H. Inoue, "Non-destructive terahertz imaging of illicit drugs using spectral fingerprints," *Opt. Express* 11 (20), 2549-2554 (2003).
45. M. B. Campbell, and E. J. Heilweil, "Noninvasive detection of weapons of mass destruction using THz radiation" *Proc. of SPIE* 5070, 38 (2003).
46. W. R. Tribe, D. A. Newnham, P. F. Taday, and M. C. Kemp, "Hidden object detection: security applications of terahertz technology" *Proc. of SPIE* 5354, 168-176 (2004).
47. D. J. Cook, B. K. Decker, G. Maislin, and M. G. Allen, "Through container THz sensing: applications for explosive screening" *Proc. of SPIE* 5354, 55 (2004).
48. R. Osiander, J. A. Miragliotta, Z. Jiang, J. Xu, and X. C. Zhang, "Mine field detection and identification using THz spectroscopic imaging," *Proc. of SPIE* 5070, 1-6 (2003).
49. M. C. Kemp, P. F. Taday, B. E. Cole, J. A. Cluff, A. J. Fitzgerald, W. R. Tribe, "Security applications of terahertz technology," *Proc. of SPIE* 5070, 44-52 (2003).
50. D. Clery, "Terahertz on a chip," *Science* 297, 5582, 763 (2002).
51. <http://www.lakeshore.com/products/THz-System/Pages/technology.aspx>
52. B. B. Hu and M. C. Nuss, "Imaging with terahertz waves," *Opt. Lett.* 20 (16), 1716-1718 (1995).

53. K. F. Ross, R. E. Gordon, "Water in malignant tissue, measured by cell refractometry and nuclear magnetic resonance," *J. Microsc.* 128 (1), 7-21 (1982).
54. J. H. Chen, H. E. Avram, L. E. Crooks, M. Arakawa, L. Kaufman, and A. C. Brito, "In vivo relaxation times and hydrogen density at 0.063-4.85 T in rats with implanted mammary adenocarcinomas," *Radiology* 184 (2) 427-434 (1992).
55. C. S. Joseph, R. Patel, V. A. Neel, R. H. Giles, and A. N. Yaroslavsky, "Imaging of ex vivo nonmelanoma skin cancers in the optical and terahertz spectral regions," *J. Biophotonics* 10.1002, 1-10, (2012).
56. J. A. Zeitler, and L. F. Gladden, "In-vitro tomography and non-destructive imaging at depth of pharmaceutical solid dosage forms," *Eur. J. Pharm. Biopharm.* 71, 2-22 (2009).
57. W. L. Chan, J. Deibel, and D. M. Mittleman, "Imaging with terahertz radiation," *Rep. Prog. Phys.* 70, 1325-1379 (2007).
58. A. Nahata, J. T. Yardley, and T. F. Heinz, "Free-space electro-optic detection of continuous-wave terahertz radiation," *Appl. Phys. Lett.* 75 (17), 2524-2526 (1999).
59. K. J. Siebert, H. Quast, R. Leonhardt, T. Löffler, M. Thomson, T. Bauer, H. G. Roskos, and S. Czasch, "Continuous-wave all-optoelectronic terahertz imaging," *Appl. Phys. Lett.* 80 (16), 3003-3005 (2002).
60. L. Möller, J. Federici, A. Sinyukov, C. Xie, H. C. Lim, and R. C. Giles, "Data encoding on terahertz signals for communication and sensing," *Opt. Lett.* 33 (4), 393-395 (2008).
61. T. -A. Liu, G. -R. Lin, Y. -C. Chang, and C. -L. Pan, "Wireless audio and burst communication link with directly modulated THz photoconductive antenna," *Opt. Express* 13 (25), 10416-10423 (2005).
62. E. R. Mueller and A. J. DeMaria, "Broad bandwidth communication/data links using terahertz sources and Schottky diode modulators/detectors," *Proc. of SPIE* 5727, 151-165 (2005).
63. C. Jastrow, K. Munter, R. Piesiewicz, T. Kurner, M. Koch, and T. Kleine-Ostmann, "300 GHz transmission system," *Electron. Lett.* 44 (3), 213 (2008).
64. Z. Ghattan, T. Hasek, R. Wilk, M. Shahabadi, and M. Koch, "Sub-terahertz on-off switch based on a two-dimensional photonic crystal infiltrated by liquid crystals," *Opt. Commun.* 281, 46234625 (2008).
65. R. Wilk, N. Vieweg, A. Kopschinski, and M. Koch, "Liquid crystal based electrically switchable Bragg structure for THz waves," *Opt. Express* 17 (9), 7377-7382 (2009).

66. R. Kersting, G. Strasser, and K. Unterrainer, "Terahertz phase modulator," *Electron. Lett.* 36 (13), 1156-1158 (2000).
67. I. H. Libon, S. Baumgärtner, M. Hempel, N. E. Hecker, J. Feldmann, M. Koch, and P. Dawson, "An optically controllable terahertz filter," *Appl. Phys. Lett.* 76 (20), 2821-2823 (2000).
68. P. Kužel and F. Kadlec, "Tunable structures and modulators for THz light," *C. R. Physique* 9, 197-214 (2008).
69. J. Federici and L. Moeller, "Review of terahertz and subterahertz wireless communications," *J. Appl. Phys.* 107, 111101 (1-22) (2010).
70. <http://herschel.jpl.nasa.gov/farIRandSubmm.shtml>
71. W. S. Holland, E. I. Robson, W. K. Gear, C. R. Cunningham, J. F. Lightfoot, T. Jenness, R. J. Ivison, J. A. Stevens, P. A. R. Ade, M. J. Griffin, W. D. Duncan, J. A. Murphy, and D. A. Naylor, "SCUBA: a common-user submillimetre camera operating on the James Clerk Maxwell Telescope," *Mon. Not. R. Astron. Soc.* 303, 659-672 (1999).
72. J. E. Ruhl, P. A. R. Ade, J. E. Carlstrom, H. M. Cho, T. Crawford, M. Dobbs, C. H. Greer, N. W. Halverson, W. L. Holzapfel, T. M. Lanting, A. T. Lee, J. Leong, E. M. Leitch, W. Lu, M. Lueker, J. Mehl, S. S. Meyer, J. J. Mohr, S. Padin, T. Plagge, C. Pryke, D. Schwan, M. K. Sharp, M. C. Runyan, H. Spieler, Z. Staniszewski, and A. A. Stark, "The south pole telescope," *Proc. of SPIE* 5498, 11-30 (2004).
73. R. S. Booth "ALMA, the Atacama large millimeter array," European Space Agency, (Special Publication) SP-451, 107-114 (2000).
74. T. G. Phillips and J. Keene, "Submillimeter Astronomy," *Proc. of IEEE* 80, 1662-1678 (1992).
75. D. Griffiths, "Introduction to Electrodynamics," Third Edition, New Jersey, Prentice-Hall, Inc. (1999).
76. V. G. Veselago, "The electrodynamics of substances with simultaneously negative values of  $\epsilon$  and  $\mu$ ," *Sov. Phys. Usp.* 10 (4), 509-514 (1968).
77. J. B. Pendry, A. J. Holden, D. J. Robbins, and W. J. Stewart, "Magnetism from conductors and enhanced nonlinear phenomena," *IEEE Trans. Microwave Theory Tech.* 47 (11), 2075-2084 (1999).
78. D. R. Smith, W. J. Padilla, D. Vier, S. Nemat-Nasser, and S. Schultz, "Composite medium with simultaneously negative permeability and permittivity," *Phys. Rev. Lett.* 84 (18) 4184-4187 (2000).

79. R. M. Walser, "Electromagnetic metamaterials," *Proc. of SPIE* 4467, 1-15, 2001.
80. N. I. Zheludev, "A roadmap for metamaterials," *Opt. Photonics News* 22, 30–35 (2011).
81. C. M. Soukoulis and M. Wegener, "Past achievements and future challenges in 3D photonic metamaterials," *Nature Photon.* 5, 523-530 (2011).
82. S. A. Cummer, B. -I. Popa, D. Schurig, D. R. Smith and J. B. Pendry, "Full-wave simulations of electromagnetic cloaking structures," *Phys. Rev. E* 74, 036621 (1-5) (2006).
83. D. Schurig, J. J. Mock, B. J. Justice, S. A. Cummer, J. B. Pendry, A. F. Starr, and D. R. Smith, "Metamaterial electromagnetic cloak at microwave frequencies," *Science* 314, 977-980 (2006).
84. N. Fang and X. Zhang, "Imaging properties of a metamaterial superlens," *Appl. Phys. Lett.* 82 (2), 161-163 (2003).
85. K. Aydin, I. Bulu, and E. Ozbay, "Subwavelength resolution with a negative-index metamaterial superlens," *Appl. Phys. Lett.* 90, 254102 (1-3) (2007).
86. X. Zhang and Z. Liu, "Superlenses to overcome the diffraction limit," *Nature Materials* 7, 435-441 (2008).
87. F. Martín, F. Falcone, J. Bonache, R. Marqués, and M. Sorolla, "Miniaturized coplanar waveguide stop band filters based on multiple tuned split ring resonators," *IEEE Microw. Wireless Compon. Lett.* 13 (12) 511-513 (2003).
88. J. García-García, F. Martín, F. Falcone, J. Bonache, I. Gil, T. Lopetegi, M. A. G. Laso, M. Sorolla, and R. Marqués, "Spurious passband suppression in microstrip coupled line band pass filters by means of split ring resonators," *IEEE Microw. Wireless Compon. Lett.* 14 (9) 416-418 (2004).
89. H. -T. Chen, S. Palit, T. Tyler, C. M. Bingham, J. M. O. Zide, J. F. O'Hara, D. R. Smith, A. C. Gossard, R. D. Averitt, W. J. Padilla, N. M. Jokerst, and A. J. Taylor, "Hybrid metamaterials enable fast electrical modulation of freely propagation terahertz waves," *Appl. Phys. Lett.* 93, 091117 (1-3) (2008).
90. H. -T. Chen, W. J. Padilla, M. J. Cich, A. K. Azad, R. R. Averitt, and A. J. Taylor, "A metamaterial solid-state terahertz phase modulator," *Nature Photonics* 3, 148-151 (2009).
91. H. Zhou, F. Ding, Y. Jin, and S. L. He, "Terahertz metamaterial modulators based on absorption," *Progr. Electromagn. Res.* 119, 449-460 (2011).

92. H. Chen, B. -I. Wu, L. Ran, T. M. Grzegorzczuk, and J. A. Kong, "Controllable left-handed metamaterial and its application to a steerable antenna," *Appl. Phys. Lett.* 89, 053509 (1-3) (2006).
93. H. -N. Liu, H. -L. Su, K. -H. Lin, C. -Y. Wu, C. -L. Tang, and S. -H. Yeh, "Design of antenna radome composed of metamaterials for high gain," *Antennas and Propagation Society International Symposium*, 19-22 (2006).
94. M. Sterner, D. Chicherin, A. V. Räisänen, G. Stemme, and J. Oberhammer, "RF MEMs high-impedance tuneable metamaterials for millimeter-wave beam steering," *Proc. of the IEEE MEMS*, 896-899 (2009).
95. A. Lai, K. M. K. H. Leong, and T. Itoh, "Leaky-wave steering in a two-dimensional metamaterial structure using wave interaction excitation," *Proc. IEEE MTT-S Int. Microwave Symp.*, 1643-1646 (2006).
96. R. Islam and G. V. Eleftheriades, "A planar metamaterial co-directional coupler that couples power backwards," *Proc. IEEE MTT-S Int. Microwave Symp.*, 321-324 (2003).
97. R. Islam, F. Elek, and G. V. Eleftheriades, "Coupled-line metamaterial coupler having co-directional phase but contra-directional power flow," *Electron Lett.* 40, 315-317 (2004).
98. R. Marqués, J. Martel, F. Mesa, and F. Medina, "Left-handed simulation and transmission of EM waves in subwavelength split-ring-resonator-loaded metallic waveguides," *Phys. Rev. Lett.* 89 (18), 1-4 (2002).
99. B. Edwards, A. Alu, M. E. Young, M. Silveirinha, and N. Engheta, "Experimental verification of epsilon-near-zero metamaterial coupling and energy squeezing using a microwave waveguide," *Phys. Rev. Lett.* 100, 033903 (1-4) (2008).
100. Barry R. Masters, "Confocal microscopy and multiphoton excitation microscopy: The Genesis of Live Cell Imaging," SPIE Optical Engineering Press, (2006)
101. Sir William Thomson Lord Kelvin, "The Molecular Tactics of a Crystal," Clarendon Press, (1894).
102. S. Tretyakov, I. Nefedov, A. Sihvola, S. Maslovski, and C. Simovski, "Waves and energy in chiral nihility," *J. Electromagn. Waves Appl.* 17 (5), 695-706 (2003).
103. J. B. Pendry, "A chiral route to negative refraction," *Science* 306 (5700), 1353-1355 (2004).
104. M. Decker, M. W. Klein, and M. Wegener, "Circular dichroism of chiral magnetic metamaterials," *Opt. Lett.* 32 (7), 856-858 (2007).

105. D. -H. Kwon, P. L. Werner, and D. H. Werner, "Optical planar chiral metamaterial designs for strong circular dichroism and polarization rotation," *Opt. Express* 16 (16), 11802- 11807 (2008).
106. W. Zhang, A. Potts, and D. M. Bagnall, "Giant optical activity in dielectric planar metamaterials with two-dimensional chirality," *J. Opt. A: Pure Appl. Opt.* 8, 878-890 (2006).
107. Y. Ye and S. He, "90 degree polarization rotator using a bilayered chiral metamaterial with giant optical activity," *Appl. Phys. Lett.* 96, 203501 (1-3) (2010).
108. R. Zhao, J. Zhou, Th. Koschny, E. N. Economou, and C. M. Soukoulis, "Repulsive Casimir force in chiral metamaterials," *Phys. Rev. Lett.* 103 (10), 103602 (1-4) (2009).
109. R. Zhao, Th. Koschny, E. N. Economou, and C. M. Soukoulis, "Comparison of chiral metamaterial designs for repulsive Casimir force," *Phys. Rev. B* 81, 235126 (1-5) (2010).
110. Z. Li, H. Caglayan, K. B. Alici, M. Kafesaki, C. M. Soukoulis, and E. Ozbay, "Composite chiral metamaterials with negative refractive index and high values of the figure of merit," *Opt. Express* 20 (6), 6146-6156 (2012).
111. Y. Ye, X. Li, F. Zhuang, and S. -W. Chang, "Homogeneous circular polarizers using a bilayered chiral metamaterial," *Appl. Phys. Lett.* 99, 031111 (1-3) (2011).
112. Y. Jin and S. He, "Focusing by a slab of chiral medium," *Opt. Express* 13 (13), 4974-4979 (2005).
113. C. Monzon and D. W. Forester, "Negative refraction and focusing of circularly polarized waves in optically active media," *Phys. Rev. Lett.* 95, 123904 (1-4) (2005).
114. N. I. Zheludev and Y. S. Kivshar, "From metamaterials to metadevices," *Nature Mat.* 11, 917-924 (2012).
115. H. -T. Chen, W. J. Padilla, J. M. O. Zide, A. C. Gossard, A. J. Taylor, and R. D. Averitt, "Active terahertz metamaterial devices," *Nature* 444, 597-600 (2006).
116. J. Y. Ou, E. Plum, L. Jiang, and N. I. Zheludev, "Reconfigurable photonic metamaterials," *Nano Lett.* 11 (5), 2142-2144 (2011).
117. M. Lapine, D. Powell, M. Gorkunov, I. Shadrivov, R. Marqués, and Y. Kivshar, "Structural tunability in metamaterials," *Appl. Phys. Lett.* 95, 084105 (1-3) (2009).
118. H. Tao, A. C. Strikwerda, K. Fan, W. J. Padilla, X. Zhang, and R. D. Averitt, "Reconfigurable terahertz metamaterials," *Phys. Rev. Lett.* 103, 147401 (1-4) (2009).

119. T. Hand and S. Cummer, "Characterization of tunable metamaterial elements using MEMS switches," *IEEE Antennas Wireless Propag. Lett.* 6, 401–404 (2007).
120. M. F. Karim, A. Q. Liu, A. Alphones, and A. B. Yu, "A tunable bandstop filter via the capacitance change of micromachined switches," *J. Micromech. Microeng.* 16, 851–861 (2006).
121. I. Gil, F. Martin, X. Rottenberg, and W. De Raedt, "Tunable stop-band filter at Q-band based on RF-MEMS metamaterials. *Electron. Lett.* 43 (21), 1153–1154 (2007).
122. A. E. Nikolaenko, N. Papasimakis, E. Atmatzakis, Z. Luo, Z. X. Shen, F. De Angelis, S. A. Boden, E. Di Fabrizio, and N. I. Zheludev "Nonlinear graphene metamaterial," *Appl. Phys. Lett.* 100, 181109 (1-3) (2012).
123. M. Lapine, I. V. Shadrivov, D. A. Powell, and Y. S. Kivshar, "Magnetoelastic Metamaterials," *Nature Mater.* 11, 30–33 (2012).
124. J. Zhang, K. F. MacDonald, and N. I. Zheludev, "Optical gecko toe: Optically controlled attractive near-field forces between plasmonic metamaterials and dielectric or metal surfaces," *Phys. Rev. B* 85, 205123 (2012).
125. X. Wang, D. -H. Kwon, D. H. Werner, I. -C. Khoo, A. V. Kildishev, and V. M. Shalaev, "Tunable optical negative-index metamaterials employing anisotropic liquid crystals," *Appl. Phys. Lett.* 91, 143122 (1-3) (2007).
126. F. Zhang, Q. Zhao, W. Zhang, J. Sun, J. Zhou, and D. Lippens, "Voltage tunable short wire-pair type of metamaterial infiltrated by nematic liquid crystal," *Appl. Phys. Lett.* 97 (13), 134103 (1-3) (2010).
127. F. Zhang, W. Zhang, Q. Zhao, J. Sun, K. Qiu, J. Zhou, and D. Lippens, "Electrically controllable fishnet metamaterial based on nematic liquid crystal," *Opt. Express* 19 (2), 1563–1568 (2011).
128. F. Zhang, Q. Zhao, L. Kang, D. P. Gaillot, X. Zhao, J. Zhou, and D. Lippens, "Magnetic control of negative permeability metamaterials based on liquid crystals," *Appl. Phys. Lett.* 92, 193104 (1-3) (2008).
129. L. Fok, M. Ambati, and X. Zhang, "Acoustic metamaterials," *MRS Bull.* 33, 931-934 (2008).
130. K. M. Ho, C. K. Cheng, Z. Yang, X. X. Zhang, P. Sheng, "Broadband locally resonant sonic shields," *Appl. Phys. Lett.* 83 (26), 5566-5568 (2003).
131. N. Fang, D. Xi, J. Xu, M. Ambati, W. Srituravanich, C. Sun, X. Zhang, "Ultrasonic metamaterials with negative modulus," *Nature Materials* 5, 452-456 (2006).

132. Y. Cheng, F. Yang, J. Y. Xu, and X. J. Liu, "A multilayer structured acoustic cloak with homogeneous isotropic materials," *Appl. Phys. Lett.* 92, 051913 (1-3) (2008).
133. H. Meng, J. Wen, H. Zhao, and X. Wen, "Optimization of locally resonant acoustic metamaterials on underwater sound absorption characteristics," *Journal of Sound and Vibration* 331, 4406-4416 (2012).
134. H. Torres-Silva and D. Torres, "Chiral seismic attenuation with acoustic metamaterials," *Journal of Electromagnetic Analysis and Applications* 5, 426-431 (2012).
135. J. Mei, G. Ma, M. Yang, Z. Yang, W. Wen, and P. Sheng, "Dark acoustic metamaterials as super absorbers for low-frequency sound," *Nat. Commun.* 3 (756), 1-9 (2012).
136. M. Ambati, N. Fang, C. Sun, and X. Zhang, "Surface resonant states and superlensing in acoustic metamaterials," *Phys. Rev. B* 75, 195447 (1-5) (2007).
137. D. H. Auston, "Picosecond photoconduction Hertzian dipoles," *Appl. Phys. Lett.* 45 (3), 284-286 (1984).
138. National Instruments white paper available at: <http://www.ni.com/white-paper/4541/en/> published July 28, 2011.
139. W. J. Padilla, A. J. Taylor, C. Highstrete, M. Lee, and R. D. Averitt, "Dynamical electric and magnetic metamaterial response at terahertz frequencies," *Phys. Rev. Lett.* 96, 107401 (1-4) (2006).
140. H. Tao, A. Strikwerda, K. Fan, C. Bingham, W. J. Padilla, X. Zhang, and R. D. Averitt, "A dual band terahertz metamaterial absorber," *J. Phys. D: Appl. Phys.* 41, 232004 (1-5) (2008).
141. N. Liu, and H. Giessen, "Coupling effects in optical metamaterials," *Angew. Chem. Int. Ed.* 49, 9838-9852 (2010).
142. J. Wang, S. Qu, Z. Xu, J. Zhang, Y. Yang, H. Ma, and C. Gu, "A candidate three-dimensional GHz left-handed metamaterial composed of coplanar magnetic and electric resonators," *Photon Nanostruct. Fundam. Appl.* 6, 183 (2008).
143. V. Crnojevic-Bengin, V. Radonic, and B. Jokanovic, "Fractal geometries of complementary split-ring resonators," *IEEE Trans. Microw. Theory Tech.* 56, 10, 2312-2321 (2008).
144. J. Zhou, TH. Koschny, M. Kafesaki, E. N. Economou, J. B. Pendry, and C. M. Soukoulis, "Saturation of the magnetic response of split-ring resonators at optical frequencies," *Phys. Review Lett.* 95, 223902 (1-4) (2005).

145. A. B. Movchan and S. Guenneau, "Split-ring resonators and localized modes," *Phys. Rev. B* 70, 125116 (1-5) (2004).
146. A. K. Azad, J. Dai, and W. Zhang, "Transmission properties of terahertz pulses through subwavelength double split-ring resonators," *Opt. Lett.* 31 (5), 634-636 (2006).
147. R. Singh, A. K. Azad, J. F. O'Hara, A. J. Taylor, and W. Zhang, "Effect of metal permittivity on resonant properties of terahertz metamaterials," *Opt. Lett.* 33 (13), 1506-1508 (2008).
148. T. J. Yen, W. J. Padilla, N. Fang, D. C. Vier, D. R. Smith, J. B. Pendry, D. N. Basov, and X. Zhang, "Terahertz magnetic response from artificial materials," *Science* 303, 1494-1496 (2004).
149. B. Wu, B. Li, T. Su, and C. -H. Liang, "Equivalent-circuit analysis and lowpass filter design of split-ring resonator DGS," *J. of Electromagn. Waves and Appl.* 20 (14), 1943-1953 (2006).
150. H. Bahrami and M. Hakkak, "Analysis and design of highly compact bandpass waveguide filter utilizing complementary split ring resonators (CSRR)," *PIER* 80, 107-122 (2008).
151. L. -M. Si and X. Lv, "CPW-fed multi-band omni-directional planar microstrip antenna using composite metamaterial resonators for wireless communications," *PIER* 83, 133-146 (2008).
152. I. McGregor and K. M. Hock, "Complementary split-ring resonator-based deflecting structure," *Phys. Rev. Spec. Topics-Accelerators and Beams* 16, 090101 (1-12) (2013).
153. I. V. Shadrivov, S. K. Morrison, and Y. S. Kivshar, "Tunable split-ring resonators for nonlinear negative-index metamaterials," *Optics Express* 14 (20), 9344-9349 (2006).
154. B. A. Munk. "Frequency Selective Surfaces: Theory and Design". John Wiley & Sons (2000).
155. H. Tao, N. I. Landy, C. M. Bingham, X. Zhang, R. D. Averitt, and W. J. Padilla, "A metamaterial absorber for terahertz regime: Design, fabrication and characterization," *Optics Express* 16 (10), 7181-7188 (2008).
156. D. Schurig, J. J. Mock, and D. R. Smith, "Electric-field-coupled resonators for negative permittivity metamaterials," *Appl. Phys. Lett.* 88, 041109 (1-3) (2006).
157. C. Wu, B. Neuner III, and G. Shvets, "Large-area wide-angle spectrally selective plasmonic absorber," *Phys. Rev. B* 84, 075102 (1-7) (2011).

158. Y. Ma, Q. Chen, J. Grant, S. C. Saha, A. Khalid, and D. R. S. Cumming, "A terahertz polarization insensitive dual band metamaterial absorber," *Opt. Lett.* 36 (6), 945-947 (2011).
159. Y. Q. Ye, Y. Jin, and S. He, "Omnidirectional, polarization-insensitive and broadband thin absorber in the terahertz regime," *J. Opt. Soc. Am. B* 27 (3), 498-504 (2010).
160. F. Alves, B. Kearney, D. Grbovic, "Strong terahertz absorption using SiO<sub>2</sub>/Al based metamaterial structures," *App. Phys. Lett.* 100, 111104 (1-3) (2012).
161. J. Wu and W. Qin, "Terahertz dual-band nearly perfect absorbers based on combined of two types of FSS elements," *Microwave Workshop Series on Millimeter Wave Wireless Technology and Applications (IMWS), IEEE MTT-S International, China* (2012).
162. H. -T. Chen, "Interference theory of metamaterial perfect absorbers," *Optics Express* 20 (7), 7165-7172 (2012).
163. X. -Y. Peng, B. Wang, S. Lai, D. H. Zhang, and J. -H. Teng, "Ultrathin multi-band planar metamaterial absorber based on standing wave resonances," *Optics Express* 20 (25), 27756-27765 (2012).
164. Y. Zeng, H. -T. Chen and D. A. R. Dalvit, "A reinterpretation of the metamaterial perfect absorber," arXiv: 1201.5109 (2012).
165. H. Tao, C. M. Bingham, D. Pilon, K. Fan, A. C. Strikwerda, D. Shrekenhamer, W. J. Padilla, X. Zhang, and R. D. Averitt, "A dual band terahertz metamaterial absorber". *J. Phys. D: Appl. Phys.* 43, 225102 (1-5) (2010).
166. Q. -Y. Wen, H. -W. Zhang, Y. -S. Xie, Q. -H. Yang, and Y. -L. Liu, "Dual band terahertz metamaterial absorber: Design, fabrication, and characterization," *Appl. Phys. Lett.* 95, 241111 (1-3) (2009).
167. X. -J. He, Y. Wang, J. Wang, T. Gui, and Q. Wu, "Dual-band terahertz metamaterial absorber with polarization insensitivity and wide incident angle," *PIER* 115, 381-397 (2011).
168. L. Huang, D. R. Chowdhury, S. Ramani, M. T. Reiten, S. -N. Luo, A. J. Taylor, and H. -T. Chen, "Experimental demonstration of terahertz metamaterial absorbers with a broad and flat absorption band," *Optics Letters* 37 (2), 154-156 (2012).
169. J. Sun, L. Liu, G. Dong and J. Zhou, "An extremely broadband metamaterial absorber based on destructive interference," *Optics Express* 19 (22), 21155-21162 (2011).
170. J. Grant, Y. Ma, S. Saha, A. Khalid, and D. R. S. Cumming, "Polarization insensitive, broadband terahertz metamaterial absorber," *Optics Letters*, 36 (17), 3476-3478 (2011).

171. Y. Liu, S. Gu, C. Luo, and X. Zhao, "Ultra-thin broadband metamaterial absorber," *Applied Physics A* 108 (1), 19-24 (2012).
172. L. K. Sun, H. F. Cheng, Y. J. Zhou, "Broadband metamaterial absorber based on coupling resistive frequency selective surface," *Optics Express* 20 (4), 4675-4980 (2012).
173. N. I. Landy, C. M. Bingham, T. Tyler, N. Jokerst, D. R. Smith, and W. J. Padilla, "Design, theory, and measurement of a polarization-insensitive absorber for terahertz imaging," *Phys. Rev. B* 79, 125104 (1-6) (2009).
174. B. Zhu, Z. -B. Wang, Z. -Z. Yu, Q. Zhang, J. -M. Zhao, Y. -J. Feng, and T. Jiang, "Planar metamaterial microwave absorber for all wave polarizations," *Chin. Phys. Lett.* 26, 114102 (2009).
175. C. Gu, S. Qu, Z. Pei, H. Zhou, J. Wang, "A wide-band, polarization-insensitive and wide-angle terahertz metamaterial absorber," *PIER Lett.* 17, 171-179 (2010).
176. Z. H. Jiang, S. Yun, F. Toor, D. H. Werner, and T. S. Mayer, "Conformal dual-band near-perfectly absorbing mid-infrared metamaterial coating," *ACS Nano* 5 (6), 4641-4647 (2011).
177. K. B. Alici, A. B. Turhan, C. M. Soukoulis, and E. Ozbay, "Optically thin composite resonant absorber at the near-infrared band: a polarization independent and spectrally broadband configuration," *Optics Express* 19 (15), 14260-14267 (2011).
178. C. M. Watts, X. Liu, and W. J. Padilla, "Metamaterial electromagnetic wave absorbers," *Adv. Mat.* 24, OP98-OP120 (2012).
179. M. Parvinnezhad Hokmabadi, D. S. Wilbert, P. Kung, and S. M. Kim, "Terahertz metamaterial absorbers," *Terahertz Science and Technology* 6 (1), 40-58 (2013).
180. A. Sugimoto, H. Ochi, S. Fujimura, A. Yoshida, T. Miyadera, and M. Tsuchida, "Flexible OLED displays using plastic substrates," *IEEE J. Sel. Top. Quantum Electron.* 10 (1), 107-114 (2004).
181. A. N. Tiwari, M. Krejci, F. -J. Haug, and H. Zogg, "12.8% efficiency Cu (In, Ga) Se<sub>2</sub> solar cell on a flexible polymer sheet," *Prog. Photovolt: Res. Appl.* 7, 393-397 (1999).
182. F. Axisa, P. M. Schmitt, C. Gehin, F. Delhomme, E. McAdams, and A. Dittmar, "Flexible Technologies and Smarth Clothing for Citizen Medicine, Home Healthcare, and Disease Prevention," *IEEE Trans. Inf. Technol. Biomed.* 9 (3), 325-336 (2005).
183. H. Tao, C. M. Bingham, A. C. Strikwerda, D. Pilon, D. Shrekenhamer, N. I. Landy, K. Fan, X. Zhang, W. J. Padilla, and R. D. Averitt, "Highly flexible wide angle of incidence

- terahertz metamaterial absorber: Design, fabrication, and characterization,” *Phys. Rev. B* 78, 241103(R) (1-4) (2008).
184. R. Melik, E. Unal, N. K. Kosku, C. Puttlitz, and H. V. Demir, “Flexible metamaterials for wireless strain sensing,” *Appl. Phys. Lett.* 95, 181105 (1-3) (2009).
  185. M. Choi, S. H. Lee, Y. Kim, S. B. Kang, J. Shin, M. H. Kwak, K. –Y. Kang, Y. –H. Lee, N. Park, and B. Min, “A terahertz metamaterial with unnaturally high refractive index,” *Nature* 470, 369-374 (2011).
  186. X. Xu, B. Peng, D. Li, J. Zhang, L. M. Wong, Q. Zhang, S. Wang, and Q. Xiong, “Flexible visible—infrared metamaterials and their applications in highly sensitive chemical and biological sensing,” *Nano Lett.* 11, 3232-3238 (2011).
  187. N. R. Han, Z. C. Chen, C. S. Lim, B. Ng, and M. H. Hong, “Broadband multi-layer terahertz metamaterials fabrication and characterization on flexible substrates,” *Optics Express* 19 (8), 6990-6998 (2011).
  188. H. Tao, A. C. Strikwerda, K. Fan, C. M. Bingham, W. J. Padilla, X. Zhang, and R. D. Averitt, “Terahertz metamaterials on free-standing highly-flexible polyimide substrates,” *J. Phys. D, Appl. Phys.* 41 (23), 232004 (1-5) (2008).
  189. Z. C. Chen, N. R. Han, Z. Y. Pan, Y. D. Gong, T. C. Chong, and M. H. Hong, “Tunable resonance enhancement of multi-layer terahertz metamaterials fabricated by parallel laser micro-lens array lithography on flexible substrates,” *Opt. Mater. Express* 1 (2), 151-157 (2011).
  190. P. K. Singh, K. A. Korolev, M. N. Afsar, and S. Sonkusale, “Single and dual band 77/95/110 GHz metamaterial absorbers on flexible polyimide substrate,” *Appl. Phys. Lett.* 99, 264101 (1-4)(2011).
  191. K. Iwaszczuk, A. C. Strikwerda, K. Fan, X. Zhang, R. D. Averitt, and P. U. Jepsen, “Flexible metamaterial absorbers for stealth applications at terahertz frequencies,” *Optics Express* 20 (1), 635-643 (2012).
  192. D. –H. Kim, D. –S. Kim, S. Hwang, and J. –H. Jang, “Surface relief structures for a flexible broadband terahertz absorber,” *Optics Express* 20 (15), 16815-16822 (2012).
  193. G. X. Li, S. M. Chen, W. H. Wong, E. Y. B. Pun, and K. W. Cheah, “Highly flexible near-infrared metamaterials,” *Optics Express* 20 (1), 397-402 (2011).
  194. J. Li, W. Withayachumnankul, S. Chang, and D. Abbott, “Metamaterial-based strain sensors,” *Proc. ISSNIP*, 6146571, 30-32 (2011).

195. T. T. Thai, H. Aubert, P. Pons, M. M. Tentzeris, and R. Plana, "Design of a highly sensitive wireless passive RF strain transducer," Proc. IEEE MTT-S Int. Microwave Symp., 1–4 (2011).
196. D. S. Wilbert, M. P. Hokmabadi, P. Kung, and S. M. Kim, "Spectroscopic characteristics of three dimensional split-ring resonator arrays at terahertz frequencies," Journal of Nanoscience and Nanotechnology, Accepted (2014).
197. D. S. Wilbert, M. P. Hokmabadi, P. Kung, and S. M. Kim, "Equivalent-circuit interpretation of the polarization insensitive performance of THz metamaterial absorbers," IEEE Transactions on Terahertz Science and Technology 3 (6), 846-850 (2013).

APPENDIX A  
PUBLICATIONS

A.1. Peer Reviewed Journal Articles

1. M. P. Hokmabadi, D. S. Wilbert, P. Kung, and S. M. Kim, "Polarization-dependent, frequency-selective THz stereometamaterial perfect absorber," *Physical Review Applications* (2014) Accepted.
2. C. García Núñez, J. L. Pau, E. Ruíz, A. García Marín, B. J. García, J. Piqueras, G. Shen, D. S. Wilbert, S. M. Kim, P. Kung, "Enhanced fabrication process of zinc oxide nanowires for optoelectronics," *Thin Solid Films* vol. 555, 42-47 (2014).
3. D. S. Wilbert, M. P. Hokmabadi, P. Kung, and S. M. Kim, "Spectroscopic characteristics of three dimensional split-ring resonator arrays at terahertz frequencies," *Journal of Nanoscience and Nanotechnology* (2013). Accepted.
4. D. S. Wilbert, M. P. Hokmabadi, P. Kung, and S. M. Kim, "Equivalent-circuit interpretation of the polarization insensitive performance of THz metamaterial absorbers," *IEEE Transactions on Terahertz Science and Technology* 3 (6), 846-850 (2013).
5. C. García Núñez, A. F. Braña, J. L. Pau, D. Ghita, B. J. García, G. Shen, D. S. Wilbert, S. M. Kim, P. Kung, "Surface optical phonons in GaAs nanowires grown by Ga-assisted chemical beam epitaxy," *Journal of Applied Physics* 115, 034307, 1-8 (2014).
6. M. P. Hokmabadi, D. S. Wilbert, P. Kung, and S. M. Kim, "Design and analysis of perfect terahertz metamaterial absorber by a novel dynamic circuit model," *Optics Express*, vol. 21, no. 14, 16455-16465 (2013).
7. D. S. Wilbert, M. P. Hokmabadi, P. Kung, and S. M. Kim, "Equivalent-circuit interpretation of the polarization insensitive performance of THz metamaterial absorbers," *IEEE Transactions on Terahertz Science and Technology*, vol. 3, no. 6 (2013): 846.
8. C. García Núñez, A. F. Braña, J. L. Pau, D. Ghita, B. J. García, G. Shen, D. S. Wilbert, S. M. Kim, P. Kung, "Pure zincblende GaAs nanowires grown by Ga-assisted chemical beam epitaxy," *Journal of Crystal Growth*, vol. 372, 205-212 (2013).
9. M. Hokmabadi, D. S. Wilbert, P. Kung, and S. M. Kim, "Terahertz metamaterial absorbers," *Terahertz Science and Technology*, vol. 6, No. 1, 40-58 (2013).

10. W. Baughman, H. Yokus, S. Balci, D. S. Wilbert, P. Kung, S. M. Kim, "Observation of Hydrofluoric Acid Burns on Osseous Tissues by Means of Terahertz Spectroscopic Imaging," *IEEE Journal of Biomedical and Health Informatics*, vol. 17, no.4, 798-805 (2013).
11. S. Balci, W. Baughman, D. S. Wilbert, G. Shen, P. Kung, and S. M. Kim, "Characteristics of THz carrier dynamics in GaN thin film and ZnO nanowires by temperature dependent terahertz time domain spectroscopy measurement," *Solid-State Electronics*, vol. 78, 68-74 (2012).
12. N. Dawahre, G. Shen, S. Balci, W. Baughman, D. S. Wilbert, N. Harris, L. Butler, R. Martens, S. M. Kim, and P. Kung, "Atom probe tomography of zinc oxide nanowires", *Journal of Electronic Materials*, vol. 41, no. 5, 801-808 (2012).
13. S. M. Kim, W. Baughman, D. S. Wilbert, L. Butler, M. Bolus, S. Balci, and P. Kung, "High sensitivity and high selectivity terahertz biomedical imaging", *Chinese Optics Letters*, vol. 9, no. 11, 110009 (2011).
14. D. S. Wilbert, G. Shen, N. Dawahre, P. Kung, and S.M. Kim, "High resolution, two-dimensional image mapping of ZnO nanowires by confocal microphotoluminescence and microRaman spectroscopy," *Journal of Nanoscience and Nanotechnology* 11, 5898-5903 (2011).

## A.2. Conference Proceedings

1. D. S. Wilbert, M. P. Hokmabadi, J. Martinez, P. Kung, and S. M. Kim, "Terahertz metamaterials perfect absorbers for sensing and imaging," Proceedings of SPIE, vol. 8585 (2013).
2. M. P. Hokmabadi, D. S. Wilbert, P. Kung, and S. M. Kim, "Theoretical and experimental investigation of hybrid broadband terahertz metamaterial absorber," Proceedings of SPIE, vol. 8632 (2013).
3. W. E. Baughman, Z. Smithson, M. Baker, D. S. Wilbert, P. Kung, S. M. Kim, "Aperture-less terahertz near-field imaging," Proceedings of SPIE, vol. 8585 (2013).
4. H. Yokus, W. Baughman, S. Balci, M. Bolus, D. S. Wilbert, P. Kung, S. M. Kim, "Identification of tissue interaction of terahertz radiation toward functional tissue imaging", Proceedings of SPIE, vol. 8585 (2013).
5. S. M. Kim, D. S. Wilbert, M. Hokmabadi, and P. Kung, "Highly Efficient, Polarization Insensitive Terahertz Metamaterial Perfect Absorber and Imaging," in International Photonics and Optoelectronics Meetings, OSA Technical Digest (online) (Optical Society of America, 2012), paper SF2B.2.
6. L. Butler, D. S. Wilbert, W. Baughman, S. Balci, P. Kung, S. M. Kim, "Design, simulation, and characterization of THz metamaterial absorber", Proceedings of SPIE, vol. 8363 (2012).
7. W. E. Baughman, D. S. Wilbert, S. Balci, M. Bolus, M. Baker, P. Kung, S. M. Kim, M. S. Heimbeck, and H. O. Everitt, "Comparative reconstructions of THz spectroscopic imaging for non-destructive testing and biomedical imaging," Proceedings of SPIE, vol. 8363 (2012).
8. D. S. Wilbert, M. P. Hokmabadi, W. Baughman, P. Kung, S. M. Kim, "Highly efficient, polarization insensitive terahertz metamaterial perfect absorber and imaging," Proceedings of IEEE Photonics Conference (IPC), vol. 228, no. 229, 23-27 (2012).
9. P. Kung, N. Harris, G. Shen, D. S. Wilbert, W. Baughman, S. Balci, N. Dawahre, L. Butler, E. Rivera, D. Nikles, and S. M. Kim, "Photovoltaic devices based on quantum dot functionalized nanowire arrays embedded in an organic matrix", Proceedings of SPIE, vol. 8268 (2012).
10. G. Shen, N. Harris, N. Dawahre, D. S. Wilbert, W. Baughman, E. Rivera, D. Nikles, T. Bryant, S. M. Kim, P. Kung, "InP/ZnS core-shell quantum dots sensitized ZnO nanowires for photovoltaic devices," Proceedings of International Semiconductor Device Research Symposium, December 2011.

11. S. Balci, W. Baughman, D. S. Wilbert, G. Shen, P. Kung, S.M. Kim, "Characteristics of THz carrier dynamics in GaN and ZnO nanowires by temperature dependent Terahertz time domain spectroscopy measurement," Proceedings of International Semiconductor Device Research Symposium, December 2011.
12. L. Butler, D. S. Wilbert, W. Baughman, P. Kung, S. M. Kim, "Design, simulation, and characterization of THz metamaterial absorber," Proceedings of International Semiconductor Device Research Symposium, December (2011).
13. D. S. Wilbert, L. Butler, W. Baughman, P. Kung, S. M. Kim, "Terahertz spectroscopic properties of three-dimensional split-ring resonator arrays," Proceedings of 36th International Conference on Infrared, Millimeter and Terahertz Waves, October 2011.
14. W. Baughman, D. S. Wilbert, S. Balci, M. Bolus, P. Kung, S.M. Kim, "Application of terahertz spectral imaging for the identification of osseous tissue," Proceedings of 36th International Conference on Infrared, Millimeter and Terahertz Waves, October 2011.
15. S. Balci, W. Baughman, D. S. Wilbert, L. Butler, P. Kung, S. M. Kim, "Temperature dependent THz time-domain spectroscopy of carrier dynamics in GaN thin film," Proceedings of 36th International Conference on Infrared, Millimeter and Terahertz Waves, October (2011).
16. W. Baughman, D. S. Wilbert, L. Butler, N. Harris, G. Shen, N. Dawahre, J. Brewer, P. Kung and S. M. Kim, "Terahertz spectroscopy of semiconductor materials" American Physical Society 2011 March Meeting, Dallas, TX.
17. L. Butler, W. Baughman, D. S. Wilbert, N. Harris, G. Shen, N. Dawahre, J. Brewer, P. Kung and S. M. Kim, "Charge carrier lifetime in Poly(3-hexylthiophe)/ZnO nanowire array based photovoltaic devices" American Physical Society 2011 March Meeting, Dallas, TX.
18. N. Dawahre, G. Shen, D. S. Wilbert, N. Harris, W. Baughman, L. Butler, J. Brewer, S. M. Kim, and P. Kung "Micro and Nanostructural properties of wide bandgap semiconductor," American Physical Society 2011 March Meeting, Dallas, TX.
19. G. Shen, D. S. Wilbert, N. Harris, N. Dawahre, W. Baughman, L. Butler, J. Brewer, S. M. Kim, and P. Kung, "Growth and characterization of ZnMgO nanowires by thermal chemical vapor deposition," American Physical Society 2011 March Meeting, Dallas, TX.
20. D. S. Wilbert, G. Shen, N. Dawahre, N. Harris, P. Kung, and S. M. Kim, "High resolution, two-dimensional image mapping of ZnO nanowires by confocal microphotoluminescence and microRaman spectroscopy," Poster presentation at IEEE NANO 2010.

21. D. S. Wilbert, G. Shen, N. Dawahre, N. Harris, P. Kung, and S. M. Kim, “High resolution, two-dimensional image mapping of ZnO nanowires by confocal microphotoluminescence and microRaman spectroscopy,” Proceedings of Center for Materials for Information Technology Fall 2010 Research Review.
22. P. Kung, G. Shen, D. S. Wilbert, W. Baughman, M. Murphy, and S. M. Kim, “Synthesis and optical properties of ZnO nanowires for nanophotonics,” Proceedings of UGIM 2010, 18th Biennial University/Government/Industry Micro/Nano Symposium, Piscataway, NJ.
23. B. Ajilore, W. Baughman, D. S. Wilbert, J. S. Kim, P. Kung, and S. M. Kim, “Acquisition and analysis of terahertz time domain imaging and sensing,” Proceedings of IEEE SoutheastCon 2010.
24. G. Shen, D. Wilbert, B. Ajilore, M. York, W. Baughman, M. Murphy, J. S. Kim, S. M. Kim, and P. Kung, “Synthesis of zinc oxide nanowires by chemical vapor deposition,” American Physical Society 2010 March Meeting, Portland, OR.
25. D. Wilbert, G. Shen, B. Ajilore, M. York, W. Baughman, M. Murphy, P. Kung, and S. M. Kim, “Spectroscopic properties of zinc oxide nanostructures by chemical vapor deposition,” American Physical Society 2010 March Meeting, Portland, OR.